

# Application of CFD In Designing a Drug Delivery Mixing Chamber: An Experimental and Computational Study

Vahid Jalili

Centre for Numerical Modelling and Process Analysis  
School of Computing and Mathematical Sciences  
the University of Greenwich  
London



A thesis submitted in partial fulfillment of the requirements of the  
University of Greenwich for the Degree of Doctor of Philosophy

This research programme was carried out in collaboration with  
Astra Zeneca Pharmaceutical Company

March 17, 2004

---

# Declaration

---

I certify that this work has not been accepted in substance for any degree, and is not concurrently submitted for any degree other than that of Doctor of Philosophy (PhD) of the University of Greenwich. I also declare that this novel work is the result of my own investigations except where otherwise stated.

---

# Abstract

---

The purpose of this novel research was to understand the flow behaviour and improve the efficiency of the Volumatic<sup>TM</sup> spacer, using a combination of engineering tools such as CFD, Laser Doppler Anemometry (LDA) and Flow visualization techniques. The lack of information on the Volumatic<sup>TM</sup> spacer meant that, initial understanding had to be gained into the flow behaviour within the spacer. This was initially preformed by injecting air carrying a tracer concentration to represent the drug portion of the medicine. The efficiency (volume of drug collected at the mouth piece) was found to be about 6.5% which was in the same order as the figure quoted in the literature Chuffart <sup>(9)</sup>. A series of parametric studies were carried out to discover the effects of various parameters on the overall efficiency of the spacer. In the initial part a series of jet profiles were studied at the inlet, these were in the shape of staright, cone shape and spray jet profiles. It was concluded that the jet with a cone angle of 5° increased the efficiency of the spacer from 6.5% to 9.4%.

The next stage of parametric study involved reducing the length of the spacer from 0.24 m to 0.12 m and varying the inlet velocity from 40 m/s down to 10 m/s. The findings concluded that the efficiency of the spacer could be increased to 23%, using a velocity of 40 m/s at inlet. The length was reduced from 0.12 m to 0.06 m and a similar study as described above was carried out. This time it was concluded that reducing the velocity to 30 m/s increased the efficiency to 30%. The other interesting feature to come out of this study was that the whole of the spacer volume was used, hence the drug was mixing better than in the original Volumatic<sup>TM</sup> spacer, where

---

about one third of the spacer volume remained completely empty of the drug.

The studies carried out so far had shown that the additional increase in drug delivery efficiency in the case of the Volumatic<sup>TM</sup> spacer, was not substantial enough to justify the considerable manufacturing costs which have to be met, if the Volumatic<sup>TM</sup> spacer was to be remanufactured in its improved design. The way forward seemed to be in the development of a new design. The new design had to be small enough, so that it could be carried around easily by patients, who do not use the current spacer due to its size. The new design had to be economical in terms of manufacture, simple to use and easy to clean. The reasons mentioned above and the current trend towards the tube type spacer designs, implied the logical approach would be to base the design on a similar geometry. A tube type spacer was modelled with two holes drilled directly opposite each other, a distance of 10 mm away from the pMDI's nozzle. The holes introduced a pressure difference, hence directing the drug towards the patient's airway system. The new spacer had a length of 0.1 m. The computational results showed that the efficiency had increased to 71% for this particular design.

The CFD results obtained from the initial study on the Volumatic<sup>TM</sup> spacer were validated using LDA measurements. The velocities along four different locations were measured. At each location the velocities were measured at increments of 5 mm for a distance of 50 mm inside the spacer. The LDA results showed very good agreements with those obtained from CFD. The volume of data sampled experimentally at each point was 25,000 data points. This large volume of data eliminated any random sources of error, and as the CFD simulations were carried out some six months prior to LDA results, it was safe to assume that the drug had been modelled accurately. The same experimental set up was used to measure velocity values for the tube spacer, but in this instance, velocity measurements were made only along two planes, due to limited time and availability of the drug source.

Finally laser light sheeting was used to illuminate the Volumatic<sup>TM</sup> spacer and a high speed KODAK camera capable of capturing 4500 frames per second was used.

---

The visualization study proved that there was a portion of the Volumatic<sup>TM</sup> spacer which at times was free of any drug.

The originality of the work has been described in the following paragraph: Prior to this research there was no comprehensive study available combining engineering tools such as Computational Fluid Dynamics (CFD), Laser Doppler Anemometry (LDA) and High Speed Photography to study the flow pattern within the current Volumatic<sup>TM</sup> spacer design and hence analysing its efficiency. The studies carried out were of the impaction type. The results of this study have confirmed that there are several parameters contributing to the efficiency of the Volumatic<sup>TM</sup> spacer. This knowledge was not available in the open literature previously.

The initial part of this study has provided a scientific approach to analysing the flow patterns, hence obtaining an accurate value for the efficiency of the current device. This part of the study alone is a valuable tool for industry, because it has given industry data which has not been previously available. The results from this study have indicated that, the Aero Chamber Spacer type design has an efficiency of 71% compared to the current 10% efficiency of the Volumatic<sup>TM</sup> spacer. The efficiencies discussed are measured in terms of the percentage of the drug delivered to the mouth piece. The benefit to industry would be saving at a conservative estimate in terms of millions of Pounds annually. This can be calculated from industry's own figures that, 1 out of every 5 new born baby suffers from asthma in various degrees. The drug is the most expensive component of the device, hence a more efficient device would use a lesser quantity of the drug.

Finally the combination of techniques used, and the number of data samples taken for example in the case of LDA measurements some 25000 data samples were taken and averaged at each point, has ensured a high degree of accuracy and confidence in the results presented.

---

# Acknowledgements

---

I would like to express my gratitude to my supervisors Dr Mayur K. Patel and Professor Christopher Bailey for their advice and guidance throughout the study.

I would like to acknowledge the financial support of the University of Greenwich and Astra Zeneca Pharmaceutical Company and in particular Mr Ian Shrubbs who made the funding possible.

I would like to express my gratitude to my colleagues at Loughborough and Brighton University Drs Henk Versteeg, Graham Hargrave and Mr Steve Begg for allowing me to use their laboratory facilities.

---

# Dedication

---

In order for me to have completed my PhD, a number of people have been very influential and each person has contributed to my progress along the way. By way of thanking them I would like to dedicate this work to them.

The people concerned are my wife Ruth, who has encouraged me throughout and our children Soraya, Darioush and Kourosh; my brother Mr Hassan Jalili who financed my education during the early years and up to my degree; finally my parents for all they have done for me.

---

# Contents

---

<b>Abstract</b>	<b>ii</b>
<b>Acknowledgements</b>	<b>v</b>
<b>Dedication</b>	<b>vi</b>
<b>Contents</b>	<b>vii</b>
<b>List of Figures</b>	<b>xii</b>
<b>1 Introduction</b>	<b>1</b>
1.1 Introduction . . . . .	1
1.2 How The Inhalers Work . . . . .	3
1.3 Common Usage Errors . . . . .	3
1.4 General Features of the Volumatic Spacer . . . . .	4
1.5 Research Objectives . . . . .	5
1.6 The Thesis Outline . . . . .	6
<b>2 Literature Survey</b>	<b>8</b>
2.1 Introduction . . . . .	8
2.2 Drug Deposition Studies . . . . .	9
2.3 Direct Methods of Drug Deposition . . . . .	10
2.4 Devices . . . . .	10
2.4.1 Spacers . . . . .	11
2.4.1.1 Valve Spacer . . . . .	13

2.4.2	Metered Dose Inhaler . . . . .	13
2.4.2.1	Chemical Component . . . . .	13
2.4.3	The Metering Valve . . . . .	14
2.4.4	The Actuator . . . . .	14
2.4.5	The Canister . . . . .	16
2.4.6	Dry Powder Inhalers . . . . .	16
2.4.7	Nebulisers . . . . .	18
2.5	Drug Deposition In The Lung . . . . .	18
2.5.1	Factors Affecting Lung Deposition . . . . .	18
2.6	Aerosol Cloud Characterisation . . . . .	19
2.6.1	Experimental Techniques . . . . .	19
2.6.2	The Impaction Technique . . . . .	20
2.6.2.1	The Twin Impinger . . . . .	20
2.6.2.2	The Cascade Impinger . . . . .	20
2.6.3	Light Scattering Techniques . . . . .	21
2.7	Theoretical Model . . . . .	24
2.8	Various Flow Models . . . . .	26
2.8.1	Homogeneous Flow Models . . . . .	26
2.8.2	The Separated Flow Model . . . . .	27
2.9	Recent CFD Developments . . . . .	28
2.9.1	The Continuous Phase . . . . .	29
2.9.2	The Dispersed Phase . . . . .	29
2.10	Relevant Research . . . . .	30
2.11	Spray Analysis From a pMDI . . . . .	33
<b>3</b>	<b>Computational Fluid Dynamics (CFD)</b>	<b>36</b>
3.1	Introduction . . . . .	36
3.1.1	Post Processor . . . . .	39
3.2	Governing Equations . . . . .	39
3.3	Turbulent Flow . . . . .	40
3.3.1	Introduction . . . . .	40
3.4	Turbulence Models . . . . .	40

---

3.4.1	Introduction . . . . .	40
3.4.2	k- $\epsilon$ Model . . . . .	41
3.5	The RNG k- $\epsilon$ Model . . . . .	43
3.5.1	Governing Equations for the RNG k- $\epsilon$ Model . . . . .	44
3.6	The RNG and The k- $\epsilon$ Model . . . . .	44
3.7	The k- $\epsilon$ Realizable Model . . . . .	45
3.8	The Realizable k- $\epsilon$ Model Equations . . . . .	47
3.8.1	The Turbulent Viscosity . . . . .	47
3.8.2	Model Constants . . . . .	48
3.8.3	The Production of Turbulence in k- $\epsilon$ Models . . . . .	48
3.8.4	Buoyancy Effects on k- $\epsilon$ Models . . . . .	49
3.9	Wall Bounded Turbulent Flows . . . . .	50
3.9.1	Introduction . . . . .	50
3.9.2	Wall Function . . . . .	51
3.10	Discrete Phase Models . . . . .	52
3.10.1	Introduction . . . . .	52
3.11	Equation Of Motion For Particles . . . . .	52
3.12	Stochastic Particle Tracking . . . . .	53
3.12.1	Integration Of The Trajectory Equations . . . . .	54
3.13	Droplet Size Distribution . . . . .	54
3.14	Discrete Random Walk Tracking . . . . .	55
3.14.1	Prediction Of Particle Dispersion . . . . .	55
3.14.2	Discrete Random Walk Model . . . . .	56
3.15	Particle Types . . . . .	56
3.15.1	Inert Heating or Cooling . . . . .	57
3.15.2	Droplet Vaporization . . . . .	59
3.15.3	Mass Transfer During Vaporization . . . . .	59
3.15.4	Droplet Heat Transfer Equation . . . . .	61
3.16	Droplet Boiling . . . . .	62
<b>4</b>	<b>The Finite Volume Technique</b>	<b>63</b>
4.1	Introduction . . . . .	63

---

4.1.1	Convective Fluxes . . . . .	64
4.1.2	Diffusion Fluxes . . . . .	65
4.1.3	Source term approximation . . . . .	67
4.2	Segregated Solution Method . . . . .	68
4.3	Approximation of Surface Integrals . . . . .	69
4.4	The Implicit Method . . . . .	69
4.5	Pressure Calculation . . . . .	71
4.5.1	Implicit Time Advance Method . . . . .	72
4.5.2	Introduction . . . . .	72
4.5.3	Implicit Pressure-Correction methods . . . . .	74
4.6	Quadratic Upwind Interpolation Scheme: QUICK . . . . .	76
4.6.0.1	Remarks on the QUICK scheme . . . . .	78
4.7	Unstructured Grids . . . . .	78
4.7.1	Underrelaxation Criterion . . . . .	79
4.7.2	Convergence Criterion . . . . .	80
4.8	Staggered Grid . . . . .	80
4.9	Momentum Equations Variables . . . . .	82
<b>5</b>	<b>Experimental Technique</b>	<b>83</b>
5.1	Introduction . . . . .	83
5.2	Laser Systems . . . . .	84
5.3	Laser Doppler Velocimetry Configuration . . . . .	85
5.4	Real Fringe Systems . . . . .	88
5.5	Backscattering Geometries . . . . .	90
5.6	The Side Wall Effect . . . . .	90
5.7	Frequency Shifting . . . . .	92
5.8	Experimental Procedure . . . . .	93
5.8.1	Laser Doppler Anemometry . . . . .	93
5.9	Experimental Apparatus and Setup . . . . .	94
5.10	Methodology . . . . .	99
5.11	Flow Visualization . . . . .	102
5.11.1	Introduction . . . . .	102

---

5.11.2	Laser Light Sheet Unit . . . . .	102
5.11.3	Experimental Set-Up . . . . .	102
5.12	Conclusion . . . . .	103
<b>6</b>	<b>Results</b>	<b>105</b>
6.1	Introduction . . . . .	105
6.2	CFD Results . . . . .	107
6.2.1	Boundary Conditions . . . . .	107
6.2.2	Grid Dependency test . . . . .	109
6.3	Parametric Studies . . . . .	114
6.3.1	Jet configuration . . . . .	115
6.3.2	Jet With 30° Cone Angle . . . . .	119
6.3.3	19.5° deg spray Angle . . . . .	121
6.4	Geometry Effects . . . . .	124
6.4.1	New Spacer Model Length, 12cm . . . . .	125
6.4.2	New Spacer Model Length, 6cm . . . . .	131
6.4.3	Summary of The Modified Volumatic <sup>TM</sup> Designs . . . . .	135
6.4.4	Conclusions . . . . .	141
6.5	The Straight Tube Design . . . . .	141
6.5.1	Conclusions of the Parametric study . . . . .	145
6.6	Experimental Results . . . . .	146
6.6.1	Validation of CFD Results Against LDA . . . . .	146
6.6.2	Conclusions . . . . .	153
6.7	Flow Visualization Studies . . . . .	154
<b>7</b>	<b>Discussions and Conclusions</b>	<b>157</b>
7.1	Introduction . . . . .	157
7.2	Answers to the Questions Raised in Chapter 1 . . . . .	157
7.3	CFD Results . . . . .	159
7.4	Experimental Results . . . . .	162
7.5	Flow Visualizations . . . . .	162
7.6	Conclusions . . . . .	163

7.7	Further Work . . . . .	163
7.7.1	Geometrical Studies . . . . .	163
7.7.2	Full Flow Path . . . . .	164
7.7.3	Different Drugs . . . . .	164
7.7.4	Clinical Trials . . . . .	164
	<b>References</b>	<b>166</b>

---

# List of Figures

---

1.1.1	Different Drug Delivery Devices . . . . .	2
1.4.1	Volumatic <sup>TM</sup> Spacer . . . . .	4
2.4.1	Metering Valve Configuration Glaxo Smith Kline <sup>(64)</sup> . . . . .	15
2.4.2	Diagram Representing The Actuator (American Asthma Association) <sup>(55)</sup>	17
2.6.1	Optical Operation of Malvern Particle Sizer . . . . .	22
2.6.2	The SPART Particle Analyser . . . . .	23
2.6.3	The APS33 Particle Analyser . . . . .	25
2.9.1	The Mesh Used For CFD Analysis, Versteeg H.K, et. al, <sup>(69)</sup> . . . . .	29
2.10.1	Turbulent Velocity Fluctuations . . . . .	32
4.1.1	2-D Control Volume . . . . .	64
4.1.2	Approximation of gradients at cell faces Source:Ferziger 1999 . . . . .	67
4.8.1	U-control volume and its neighbouring velocities Source: Versteeg and Malalasekera,1995 . . . . .	81
4.9.1	V-control volume and its neighbouring velocities Source: Versteeg and Malalasekera, 1995 . . . . .	82
5.3.1	Schematic representation of LDV System . . . . .	86
5.3.2	Schematic representation of single lens LDV System . . . . .	88

5.4.1	Modified Version of the Optical system Proposed by Rudd . . . . .	89
5.4.2	Schematic representation of the forward scatter real fringe LDV System . . . . .	90
5.5.1	Typical backscatter optical system . . . . .	91
5.7.1	Braggcell Configuration . . . . .	93
5.9.1	Lens Mounting Assembly of The Volumatic Spacer . . . . .	95
5.9.2	Optical Breadboard and Optics . . . . .	96
5.9.3	Inhaler Trigger Switch Arrangement . . . . .	98
5.10.1	Measurement Grid Used In the Study . . . . .	101
5.11.1	Flow Visualization Equipment . . . . .	104
6.2.1	Boundary conditions for the CFD simulations . . . . .	108
6.2.2	Vector Plots Showing The Effect of Different Meshes Used In This Study . . . . .	109
112		
6.2.4	Mesh Dependence Study . . . . .	113
6.3.1	Concentration Distribution For Straight Jet . . . . .	116
6.3.2	Different Jet Configurations . . . . .	117
6.3.3	Concentration Distribution For The 5 <sup>0</sup> Jet Angle . . . . .	119
6.3.4	Diagram Showing 30 <sup>0</sup> Jet Cone angle Results . . . . .	121
6.3.5	Diagram Showing 19.5 <sup>0</sup> Spray Jet angle Results . . . . .	123
124		
6.4.1	Jet Inlet Velocities At 10 m/s For The Spacer Length 12cm . . . . .	126
6.4.2	Inlet Velocities 30m/s Spacer Length 12cm . . . . .	128
6.4.3	Inlet Velocities 40m/s Spacer Length 12cm . . . . .	130
6.4.4	Inlet Velocities 10m/s Spacer Length 6cm . . . . .	132
6.4.5	Inlet Velocities 30m/s Spacer Length 6cm . . . . .	134
6.4.6	Inlet Velocities 40m/s Spacer Length 6cm . . . . .	136
6.4.7	Concentration Distribution For Diffrent Spacer Lengths . . . . .	138
6.4.8	Concentration Distribution For Diffrent Spacer Lengths . . . . .	140
6.5.1	Comparison of the Two Spacers . . . . .	142

6.5.2	Drug Distribution For The New Aero Chamber Design . . . . .	144
6.6.1	CFD Validation Against LDA Results At Distance 12cm from Inlet From Center Line In Positive Y Direction . . . . .	147
6.6.2	Measurement Grid Used In the Study . . . . .	148
6.6.3	LDA VS CFD Measurements For The Volumatic <sup>TM</sup> . . . . .	151
6.6.4	LDA VS CFD Measurements For The Volumatic <sup>TM</sup> . . . . .	151
6.6.5	LDA VS CFD Measurements For The Volumatic <sup>TM</sup> . . . . .	152
6.6.6	LDA VS CFD Measurements For The Volumatic <sup>TM</sup> . . . . .	152
6.6.7	LDA VS CFD Measurements For The Aero Chamber Design . . . . .	153
6.7.1	Flow Visualization High Speed Photos . . . . .	156

---

# CHAPTER ONE

---

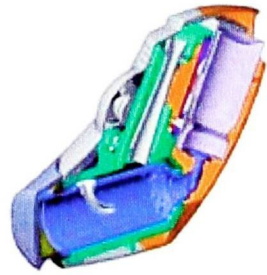
## Introduction

*This chapter begins by giving a background into the need for oral drug administration and the devices currently available. The need for this research and the methodology employed in carrying out this research have been highlighted. Finally the thesis outline has been defined.*

### §1.1 Introduction

The increase in reported cases of asthma has caused scientists to study the causes of asthma and devise efficient methods for delivering drugs such as Ventolin<sub>TM</sub> to the affected region, Figure(1.1.1) . It has been widely accepted that the most efficient means of delivering drugs to combat asthma is through the respiratory tract, however such devices suffer from lack of efficiency in terms of delivering the correct dosage. It has been widely reported in literature that approximately less than 10% of the inhaled dosage reaches the alveoli Newman S.P <sup>(50)</sup>. It is this inefficiency and associated human factors, which have led to the development of large volume spacers. The larger volume spacer attached to the end of a pMDI would allow the drug to be inhaled in a controlled manner, hence increasing the possibility of the drug reaching the affected region. The use of spacer with pMDI not only improves efficiency but may also reduce adverse effects, such as oral dysphonia, Toogood et al. <sup>(66)</sup> which may occur with high doses of inhaled steroids. The large volume spacers are relatively

---



(a) pMDI Pressurised Metered Dose Inhaler



(b) Nebuliser



ADAM

(c) Latest Nebuliser

Figure 1.1.1: Different Drug Delivery Devices

easy to use and largely overcome the problems of poor technique associated with the use of metered dose inhalers.

### §1.2 How The Inhalers Work

A typical pMDI inhaler canister, contains a solution with active ingredients which is mixed with a liquefied gas propellant under pressure. The mixture is packaged in an aluminium canister or a plastic-coated glass container. To dispense a dose of the drug, the canister needs to be pressed down. In doing so, the drug and propellant are ejected through the nozzle and into the device known as the spacer.

### §1.3 Common Usage Errors

Correct self-dosing with an pMDI is fairly difficult. In a study carried out 100 patients were trained to use pMDI's correctly. The most common errors patients make include:

- Failing to shake the canister before use
- Failing to pause and exhale slowly
- Not waiting between actuations
- Poor co-ordination between inhalation and actuations.

The last source of error poor co-ordination is by far the most common and frequent source of error and can cause in nearly the entire drug dose being deposited in the mouth or throat. In order to remedy this problem, a device known as spacer is used

### §1.4 General Features of the Volumatic Spacer

The Volumatic<sup>TM</sup> Spacer is made of transparent Perspex material as shown in Figure(1.4.1). It has a length of 24 cm, and a diameter of 4.5 cm at each end. In the middle the diameter of the spacer is 9 cm. The spacer is designed in such a way that it can be pulled apart and cleaned after use.

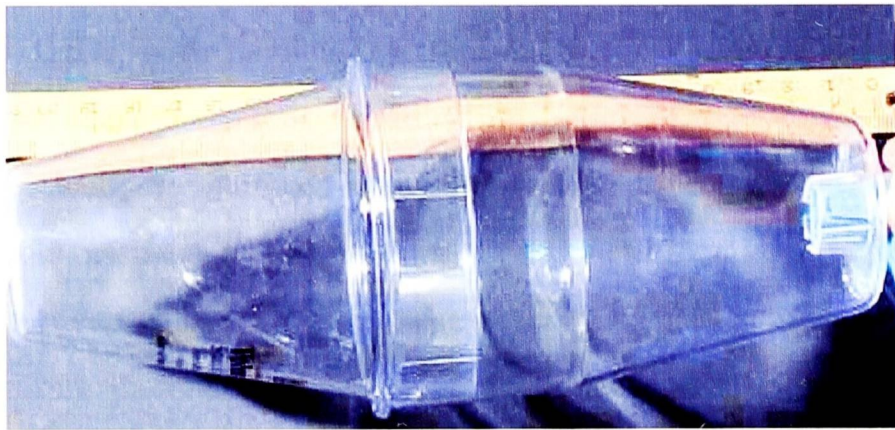


Figure 1.4.1: Volumatic<sup>TM</sup> Spacer

### §1.5 Research Objectives

The questions and answers in this section have been designed to provide a detailed explanation, as to why this research was carried out and how the out come would benefit the patients.

#### Question 1

**[Why do we need to study the flow behaviour within the Volumatic<sup>TM</sup>?]**

It is a well known fact that, the drug delivery devices in general suffer from lack of efficiency. This naturally affects the amount of drug delivered to the affected region. There have been numerous experimental and recently a few computational studies, modelling the pMDI, with particular attention to the nozzle geometry and design. There have been also experimental studies into different drug formulation. The one area pharmaceutical companies have not concentrated on has been the design of the holding chambers or spacers. This is a vital component forming an interface between the pMDI and the patient's air ways where the drug needs to be deposited. This is a novel research, looking at the current design of the Volumatic<sup>TM</sup>. The reason behind this is that, there are no previous computational or experimental studies, nor has there been any imperical data on how this particular design has been chosen. It is therefore important to understand how the current design works and what level of efficiency does it operate at. Finally any such device placed between the pMDI and the patient's air ways, needs to be operating at maximum efficiency in terms of drug dosage delivered, otherwise improvements to the nozzle efficiency would be lost.

#### Question 2

**[What is the importance of this research?]**

This research would provide validated data for the Volumatic<sup>TM</sup> and a research methodology for any such device. In terms of the benefit to the patient, it would ensure that, more of the drug dosage is delivered to the affect region in the airways, hence enhancing the research carried out on the nozzle design and development.

#### Question 3

**[Is the research worthwhile?]**

The project is worthwhile, because a more efficient spacer would reduce the number

of drug dosage a patient needs. This in return would reduce the number of refill drug capsules needed. In economic terms there would be a major reduction in budget allocated for treatment of asthma.

### Question 4

[Would the current engineering tools such as Computational Fluid Dynamics (CFD) and experimental techniques such as Laser Doppler Anemometry (LDA) and high speed photography be adequate to carry out this research? ]

The answer to this question is provided in the Discussion and Conclusion Chapter.

## §1.6 The Thesis Outline

The fundamental aim of this research is to understand the drug distribution patterns within the Volumatic<sup>TM</sup> spacer and establish a numerical value for the efficiency of this device. Initially an extensive literature survey was carried out, but there was no published material or any research in the open literature investigating the role of a spacer device.

- In the abstract a summary of the overall findings has been described.
- A general background and the reasons for carrying out this research are given, together. It is also clear from this chapter that the research has been a combination of CFD, LDA and high speed photography technique.
- A comprehensive literature survey has been presented in chapter 2.
- In chapters 3 and 4 numerical techniques and the code used are discussed.
- The experimental design and setup together with techniques such as LDA and High Speed photography used for this study are discussed in chapter 5. In this chapter the suitability of LDA system and similarity of air compared to the actual drug in terms of flow patterns within the spacer are also pointed out.

The flow visualisation set up and the capability of the high speed camera are also discussed.

- The CFD and experimental results are discussed in detail in Chapter 6. The results presented initially are those of air within the spacer. These have been validated using LDA, hence establishing the suitability of the technique for this research. The actual drug is then modelled and validated extensively using LDA technique. A series of parametric studies have also been carried out and the findings are documented. Finally the new Aero chamber design is studied and validated using LDA technique.
- Finally the findings from this study, together with a plan for the future work and answers to the questions raised in the Introduction chapter are discussed in chapter 7.

---

# CHAPTER TWO

---

## Literature Survey

*The objective of this chapter is to present and discuss the information that is related to, the work contained in this thesis. The chapter begins by looking at methods of drug deposition, then moves on to describe various devices used for drug delivery purpose. The literature then looks at the experimental techniques employed in determining the efficiency of the devices. Finally various flow models have been discussed together with the recent computational approach.*

### §2.1 Introduction

The morbidity and mortality from asthma seems to be rising, as reported by Burr<sup>(7)</sup>. A survey into the cause of death associated with asthma, Burney<sup>(6)</sup>, has pointed out, despite better understanding of the pathogenesis of the disease, Holgate<sup>(28)</sup>, more awareness of under diagnosis and under treatment, and a wide choice of effective treatments and delivery systems to deliver the drug to the affected region, Crompton<sup>(11)</sup>.

The purpose of this chapter is to bring together all the published work on the pressurised metered dose inhaler(pMDI), so that a basis is formed for carrying out this research. The literature survey in this chapter is divided into two sections, the first

section deals with the spacer device and the drug deposition studies, whereas the second section reports on the atomisation and spray formation process.

### §2.2 Drug Deposition Studies

The work of Moren <sup>(46)</sup>, has shown that the amount of drug deposited in the mouth could be significantly reduced by using a spacer device. He reported that the efficiency of the device was dependent on the length and width of the spacer, but there has been no mention in his work about the optimum length and size for the spacer. In his study a range of tube spacers and a large volume pear-shaped spacer was used. The results produced showed that longer spacers were more effective than shorter spacers in reducing drug deposition in the mouth. The wider tube resulted in less drug being lost in the pressurised metered dose inhaler (pMDI), the spacer and the mouth, suggesting that more drugs reached the airways when the large volume pear-shaped spacer was used. The novel computational study carried out in this research has given an indication of typical lengths for the spacers.

In a follow up study carried out by Newman <sup>(50)</sup>, comparing the drug deposition from an pMDI alone with that from an pMDI plus large-volume pear-shaped spacer, revealed that use of the spacer decreased oropharyngeal deposition from 80.9% to 16.5%. With the pMDI alone 8.7% of the dose reached the lungs compared with 20.9% with the addition of the spacer. In an in vitro study the deposition of Salbutamol from both an pMDI with large volume spacer attachment and without showed markedly different patterns of deposition for the two devices. With the pMDI alone, only 73.2% of the emerging dose was captured at the oropharynx and only 10.6% reached the lower airways, while the corresponding values with the spacer attached were 1.5% and 21.2%. This indicated that more deeply respirable particles which reach the lower airways were obtained with the spacer device.

### §2.3 Direct Methods of Drug Deposition

In the studies carried out by Newman <sup>(51)</sup> and Dolovich <sup>(16)</sup>, comparisons were made for drug deposition from a pMDI alone with a pMDI with a spacer attachment in patients with obstructive airways disease. The results indicated that 11% of the dose reached the lungs with the pMDI compared with significantly higher amounts for slow 16% and fast 13.3% inhalations. The distribution pattern of drug deposition within the lungs was significantly more peripheral after slow inhalation. Oropharyngeal deposition was halved by the use of spacers. In a more recent study Melchor <sup>(43)</sup> examined the lung deposition of directly radio labelled salbutamol from a pMDI inhaler alone, a pMDI with a large volume cone spacer device a dry powder inhaler (DPI) . The drug deposition was assessed by a dual headed gamma camera after inhalation of the drug. The mean percentage deposition of the drug in the lungs in the subjects was 21.6% with the pMDI alone, 20.9% with the MDI with the spacer, and 12.4% with the DPI. For the patients, total lung deposition was 18.2% with the pMDI alone, 19.0% with the pMDI spacer, and 11.4% with the DPI.

### §2.4 Devices

The pressurised metered dose inhaler (pMDI) has traditionally been the device of choice in the delivery of drugs to the lungs. There are however a range of delivery devices available for treatment of asthma. The devices are chosen according to the patient criteria. A summary of the devices and their application is shown in Table(2.4.1).

## 2.4. Devices

Type	Device	Advantages	Disadvantages
Aerosols	MDI with or without spacer Breath actuated  Small Volume Spacers	Inexpensive  Simple to use	Difficult to co-ordinate actuation and inspiration
Dry Powder	Turbohaler Clickhaler  Diskhaler Spinhaler Rotahaler Aerochamber	Simple to use Robust, Portable Indicator for doses remaining	cost  Difficult to use Drug Protection against temperature humidity
Nebuliser compressor		Simple to use can deliver high doses	expensive needs mask

Table(2.4.1) Summary of inhaler Devices

Pressurised metered dose inhaler(pMDIs) are the main devices used for treatment of asthma and are likely to remain so for the foreseeable future. However the pMDI on its own is not a very efficient device, hence in most cases a spacer device is prescribed to be used in conjunction with the pMDI.

### §2.4.1 Spacers

In an effort to overcome some problems associated with the metered dose inhalers: such as poor coordination, improved drug delivery to the lungs and reduction of

side effects produced by deposition of the drug in the oropharyngeal, spacers were designed. There are currently two types of spacers available

- Open-ended tubes
- Large volume spacers with closed ends

The function of tube spacers is to increase the distance between the mouth and the actuator of the pMDI aerosol. This allows evaporation of the propellant and slowing down of particles to enhance lung deposition.

Using a range of tube spacers and a pear-shaped large volume spacer Moren <sup>(44)</sup>, showed that the amount of drug deposited in the actuator, tube and mouth was increased when the inhalation was voluntarily delayed for 5 seconds compared with co-ordinated inhalation. It has been suggested in this research that the lack of inspiratory flow when the dose is fired increases the probability of contact between droplets in the aerosol cloud and the walls of the tube resulting in higher impaction. The conclusion reached was that the length of the tube spacer was the most critical design feature in allowing evaporation of the propellant to take place and hence deliver more of the drug to the affected region.

### §2.4.1.1 Valve Spacer

The valve spacer is yet another type of device used, in this type of spacers the dose is ejected into the device and there is generally a delay before the patient inhales the drug. The study carried out by Newman <sup>(51)</sup>, has shown that the delay time between discharge of the drug dose into the spacer and inhalation was a major factor in increasing the dosage inhaled, hence the author recommends inhalation should take place immediately after the drug has been discharged. The main advantage of large volume spacer is that, compared with the use of MDI alone, they increase the proportion of the dose delivered to the airways while reducing the proportion absorbed into the body. The research in this area has shown that a large volume spacer deposited about 21% of the dose in the lungs and 16% in the oropharynx, with 56% remaining in the spacer. A similar study was carried out using only the MDI, the results revealed that only 10-15% of the dose were deposited in the lungs and 70-80% in the oropharynx Newman <sup>(51)</sup>.

### §2.4.2 Metered Dose Inhaler

The main objective of the pMDI is to dispense a measured dose of drug and propellant at each discharge. The device is capable of discharging 200 doses accurately and therefore the velocity of discharge drops considerably as our experimental work has shown. The main use of pMDI at present is for the treatment of asthma. The pMDI consists of the following components:

- Chemical component
- Metering valve
- Actuator
- Canister

### §2.4.2.1 Chemical Component

The chemical component is made up of the drug, propellant and surfactants. The drug is atomised and dispensed in a mixture format. The drug particle sizes are in the range 0.5- 5 $\mu$ m. There have been changes enforced in EU after the Montreal Protocol <sup>(54)</sup> where the use of CFCs in the propellants has been banned since 1995.

### §2.4.3 The Metering Valve

This is the most important component in the pMDI, because this is the device responsible for measuring and delivering a measured volume in the region of 25-100 $\mu$ L depending on the setting of the valve for up to 200 discharges. The metering valve has to provide an air tight seal as shown in Figure(2.4.1).

The actuation mechanism of the metering valve is to assume the valve as a sampling chamber connecting the canister to an exit nozzle (actuator) by an inlet and outlet one way valve. The mechanism operation can be described by assuming the inlet valve to be open, the sampling chamber full and the outlet valve closed, therefore isolating the sampling chamber. Once enough pressure has been exerted on the valve stem, the outlet valve opens and the drug is discharged. The valve stem then returns to its normal position, due to the valve stem mechanism, which operates on a two stage set up. In the first stage the outlet valve is closed and then the inlet valve is opened in the second stage, allowing the sampling chamber to be filled. The metering valve then returns to its original position and is ready to discharge again.

### §2.4.4 The Actuator

The actuator is a single piece Figure(2.4.2), consisting of the mouth piece, body and the nozzle, the only way to manufacture this component of pMDI is to use injection

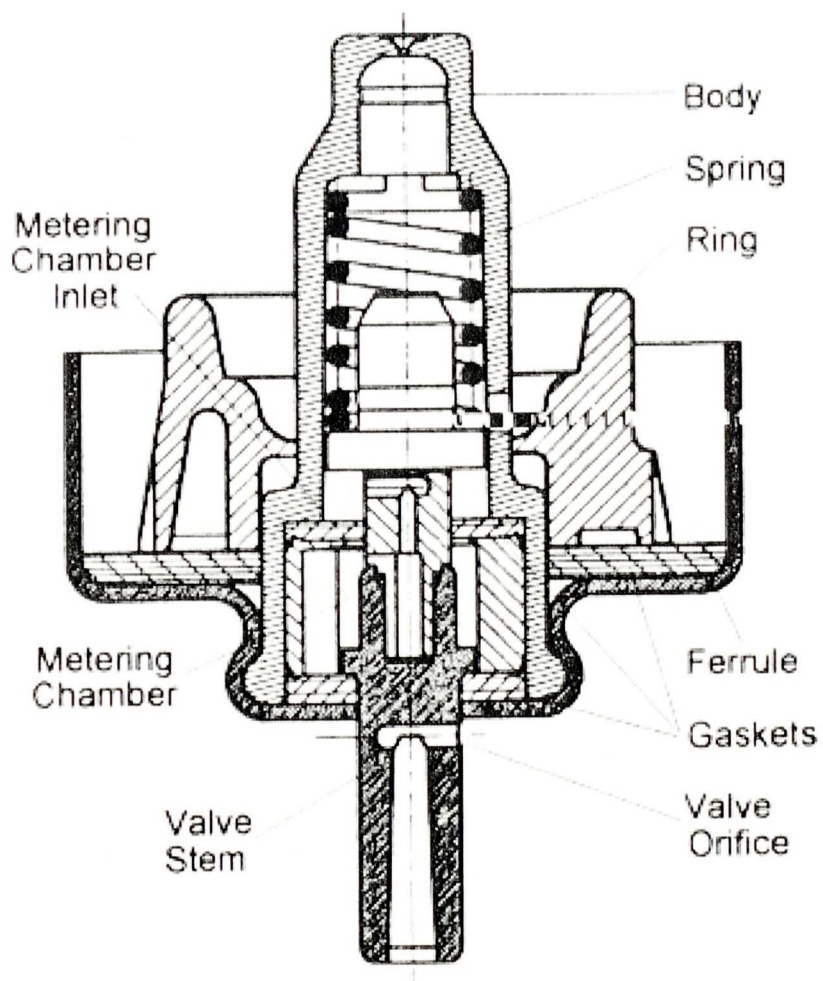


Figure 2.4.1: Metering Valve Configuration Glaxo Smith Kline <sup>(64)</sup>

moulding process.

The mouthpiece would sit either inside a device known as the spacer or directly inside the patients mouth, hence forming an interface between the actuator and the patient. The actuator body provides a means for depressing the valve stem and ensuring adequate air ducting for inhalation to the mouthpiece at an acceptable low flow rate. The actuator nozzle is an essential component in atomisation process and resultant formation. This is one of the few components of the pMDI which has not been modified since its first design by Riker Laboratories in 1995. This lack of attention to this component of the device has resulted in very little literature available regarding the spray development.

### §2.4.5 The Canister

The canister has to be very light, yet at the same time be able to withstand internal pressures of at least 10 atmospheres. The typical capacity for such canisters is in the range of 15-30ml.

### §2.4.6 Dry Powder Inhalers

In a dry powder inhaler, the drug is present as a finely milled powder which is sometimes mixed with an inert carrier such as lactose. These devices use the patient's own inspiration to create turbulent air flow necessary to disperse the drug powder and form aerosol of drug particles. In general, dry powder inhalers are easier to use than pMDIs; there are no co-ordination problems as the medication leaves the device only when the patient inhales.

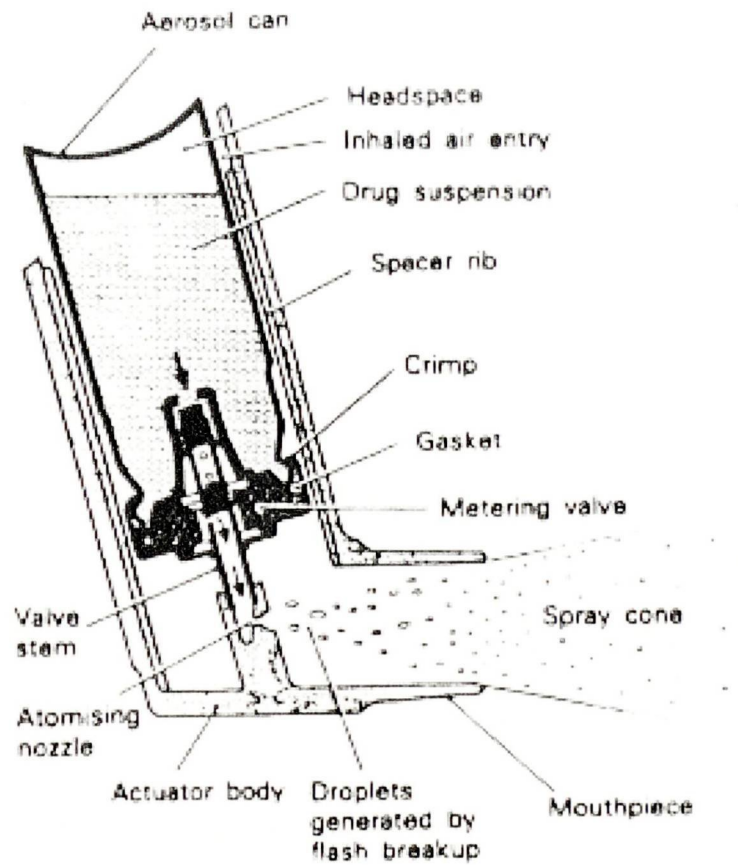


Figure 2.4.2: Diagram Representing The Actuator (American Asthma Association)<sup>(55)</sup>

### §2.4.7 Nebulisers

Nebulisers deliver drug solution as a continuous mist of tiny droplets, created using an air or oxygen compressor or high frequency vibration. In general they are easy to use, requiring simple tidal breathing and little co-ordination. In general nebulisers are fairly inefficient devices, hence larger doses need to be used.

### §2.5 Drug Deposition In The Lung

The site of deposition of an inhaled drug in the respiratory tract can influence its therapeutic effect and potential for systemic absorption Gorman<sup>(25)</sup>, Hiller<sup>(27)</sup> Moren<sup>(45)</sup>. Drug that is deposited in the oropharynx has no immediate clinical effect; it is trapped by inertial impaction and subsequently swallowed and may then be systemically absorbed. In contrast, drug deposited in the bronchi and bronchioles can have the required effect but is less well absorbed. Drug deposited in the alveoli may have no clinical effect but will be absorbed efficiently into the systemic circulation, any active drug that reaches the systemic circulation may lead to side effects.

#### §2.5.1 Factors Affecting Lung Deposition

There are a wide range of factors affecting deposition of the inhaled drug in the respiratory tract, these are as follows:

- Diameter of the air ways

In healthy, open airways, an inhaled drug will penetrate further down the bronchial tree, resulting in increased systemic absorption than in patients with asthma where the airways are narrowed.

- The size of the inhaled particles

It has been shown that the size of particles plays an important role in the penetration of the drug into the airways. It is therefore important that particles generated by the inhaler fall within the following range  $1\text{-}5\mu\text{m}$ , however it has been found that particles greater than  $5\mu\text{m}$  tend to impact the oropharynx or the bifurcations between the large upper airways. If particles are large or the air is moving rapidly, the aerosol may not be able to follow the air stream when it changes direction and may impact on the airway walls.

Particles in the range  $0.5\text{-}5\mu\text{m}$  are small enough to penetrate the lower airways, where they may settle onto the airway surfaces during steady breathing or breath holding, but particles between  $25\mu\text{m}$  will settle in the bronchi and bronchioles where they have the required clinical Effects but are less well absorbed. Particles less than  $0.5\mu\text{m}$  behave more like a gas, they are too small to be deposited by sedimentation so are simply breathed out in the next exhalation, Newman <sup>(50)</sup>.

- Method of inhalation

The type of delivery system can affect deposition of drug and its performance.

There are three types of delivery system used to administer inhaled drugs:

### §2.6 Aerosol Cloud Characterisation

There are several techniques available for characterising of the pMDI sprays. These are presented below:

#### §2.6.1 Experimental Techniques

There are several experimental techniques available for characterising sprays ejected from the pMDI. The methods are as follows:

- The Impaction Technique
- Light Scattering Technique

### §2.6.2 The Impaction Technique

This technique works on the principle that droplets of different inertia are separated by having different impaction stages, so that the droplets with lowest inertia would follow the air flow streamlines and reach the latter impaction stages. The advantage of impaction technique when applied to pMDIs is that it can account for the effects of shape, size and velocity of droplets in relation to lung deposition. This technique is therefore thought to be the only reliable means of measuring the drug deposited in the lungs.

There are two main types of impactors,

- The Twin Impinger
- The Cascade Impinger

#### §2.6.2.1 The Twin Impinger

The way twin impinger operates is to draw air in. This activates the PMDI and the spray is drawn through the system, with impaction taking place at two stages. The amount of respirable air is measured by means of mass chromatography. The down side of this technique is that drug deagglomeration which can also occur as a result of impaction.

#### §2.6.2.2 The Cascade Impinger

The cascade impaction method works on the principal that a series of decreasing jet orifices direct the spray towards the impaction plate. The disadvantages are similar to those of the twin impinger.

### §2.6.3 Light Scattering Techniques

The light scattering methods can be divided into the following categories:

- Single particle sizes
- Laser diffraction size analysis

There are commercial companies engaged in manufacturing light scattering instruments, these devices are the preferred technique for the pMDI spray analysis, since they are non-invasive in nature and information can be obtained with ease, care and at speed.

The most widely used laser diffraction size analyser is the Malvern Particle sizer. In this technique the spray is classified by measuring the drop size distribution. This is achieved by the moving drop diffracting a parallel beam of monochromatic light. The drop sizes are classified by the size of circular diffraction rings they produce, the larger the diffraction ring the smaller the drop size and visa versa. The optical arrangements of the Malvern Particle sizer is shown in Figure(2.6.1).

The main disadvantage of this equipment is that near the nozzle or distances less than 10cm due to the presence of high vapour mass, phenomena are recorded, which are not actually droplets, but in industry are referred to as phantom droplets and should be omitted from the readings. The way to overcome this problem was explained by Clark<sup>(10)</sup>, where he found the region to accurately measure the pMDI spray was in the range 8-24cm. The principal on which particle sizers operate is based on measuring

an individual particle passing through the control volume. There are two types of commercial particle sizers available, the first type is known as Aerodynamic Particle Sizer (APS) and laser-Doppler methods. In the case of APS the drop size is measured by actuating the spray in a relatively large reservoir where the propellant evaporates leaving only the drug particles to be analysed. There are two commercially available Aerodynamic Particle Sizers, these being the single particle Aerodynamic Relaxation Time Analyser and the Aerodynamic Particle Sizer (APS33). The two instruments use different techniques which are described in the following sections:

The Figure(2.6.2) is a schematic diagram of a (SPART). The device works on the phase lag produced when a particle is subjected to a given acoustic vibration within the sensing zone of a dual laser beam intersection. The drop numbers have to be reduced, so that accurate sampling can take place. The acoustic vibration caused by the droplet crossing the laser beam gives an indication of the droplet velocity. The (APS33) as shown in Figure(2.6.3) works on the principal that the time of flight of a single droplet is measured as it crosses two parallel beams. The time taken to cross the beam is dictated by the droplet inertia and hence its aerodynamic diameter. The main disadvantage of this technique is that only information on the residual

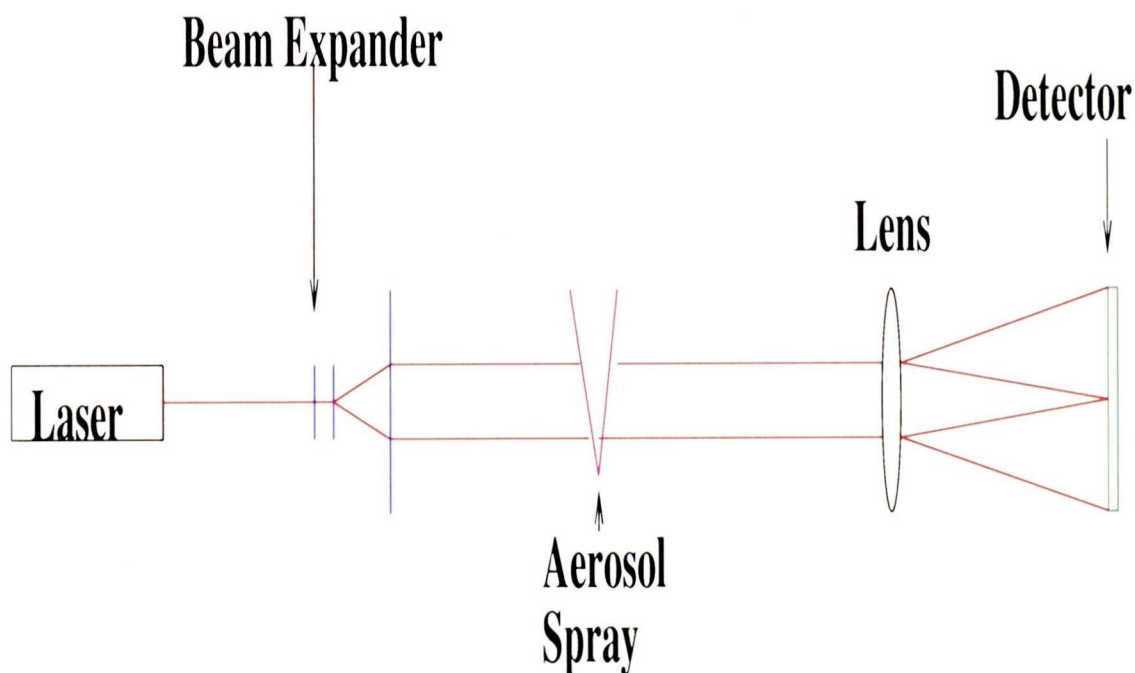


Figure 2.6.1: Optical Operation of Malvern Particle Sizer

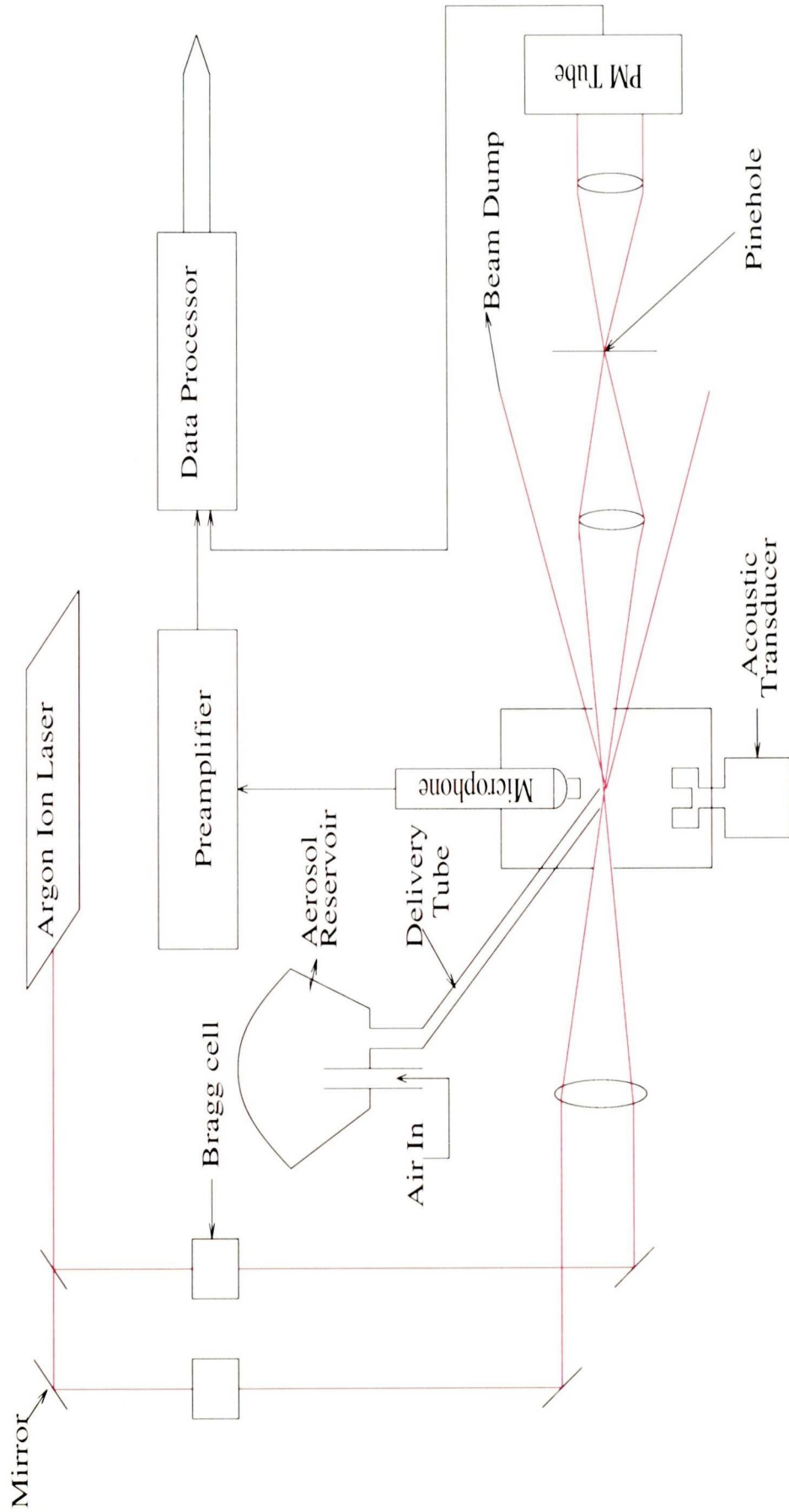


Figure 2.6.2: The SPART Particle Analyser

aerodynamic diameter can be obtained, neglecting spatial and temporal dynamic and evaporation effects which are important in the characterisation of the spray.

In both laser and phase-Doppler anemometry the measurement technique is based on the light scattered from a droplet particle as it moves through the control volume and cuts across the beams, hence providing local and spatial resolution of the droplet in real time. In the laser Doppler anemometry (LDA) approach the frequency of the Doppler burst signal is measured. This frequency is dependent on the distance between the parallel interference fringe lines in the measurement volume and the speed with which the drop traverses the measurement volume, therefore giving the drop velocity.

The application of phase Doppler anemometry (PDA) has provided a method for comprehensive spray characterisation and also providing the velocity and droplet Size. The droplet diameter is obtained by measuring the frequency shift which is produced when the Doppler burst is received by two or more detectors, separated by a given distance, and is related to drop size by a linear relationship derived from geometrical optics theory. The method of obtaining the drop velocity is similar to LDA. The disadvantage of both techniques are that only spherical particles can be measured.

### §2.7 Theoretical Model

The motivation behind the development of spray modelling, has been the need to improve the spray performance, and at the same time gain an insight into the spray formation mechanism. The advantages of spray modelling have already been recognised in areas such as internal combustion engines, fire modelling and gas turbines. The number of spray models available can be categorised into two groups. The groups are locally homogeneous models and separated flow models. The models are described in the next section.

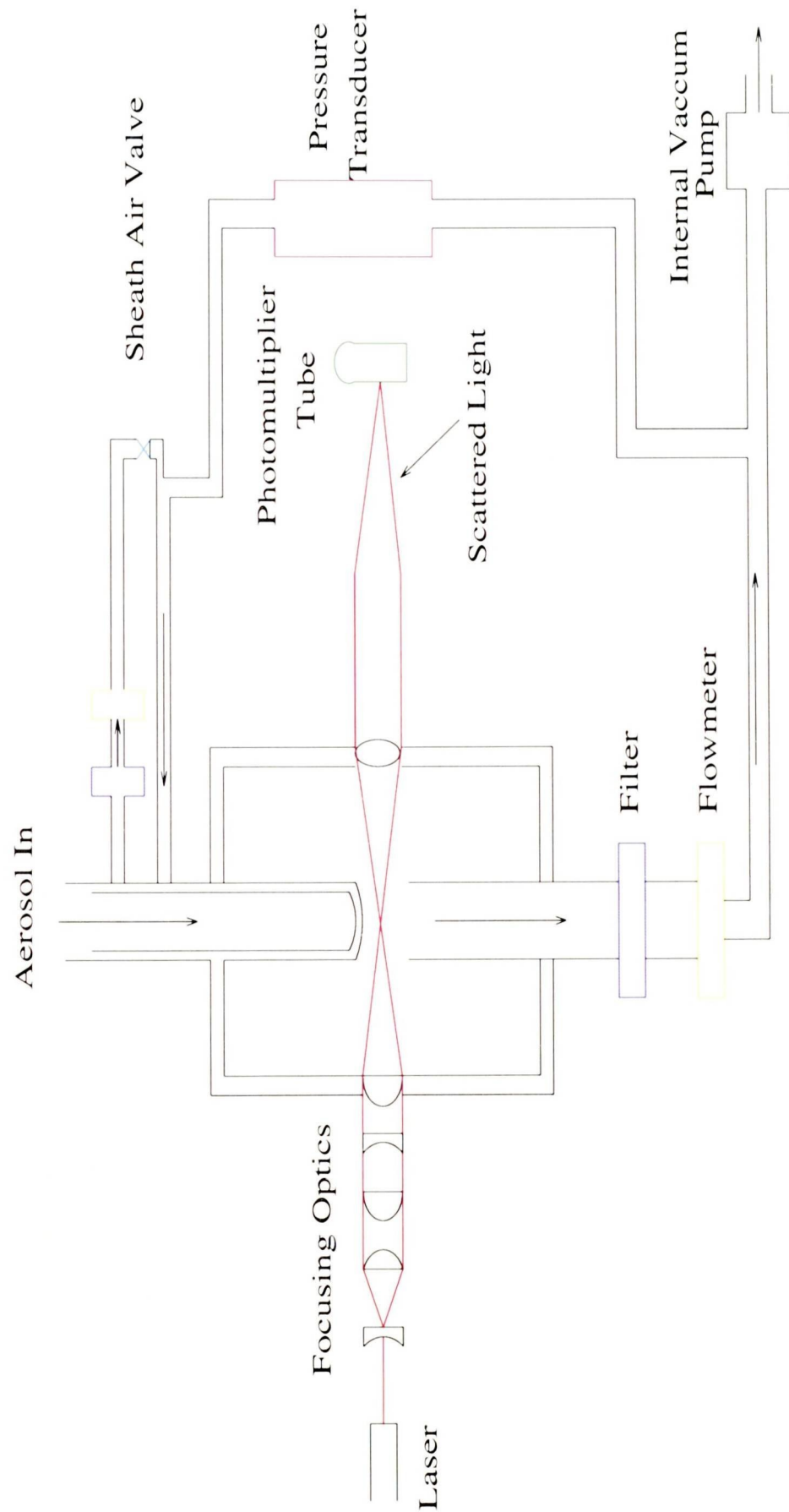


Figure 2.6.3: The APS33 Particle Analyser

### §2.8 Various Flow Models

The flow models generally fall into two categories:

- Homogeneous Flow Models
- Separated Flow Models

#### §2.8.1 Homogeneous Flow Models

In locally homogeneous flow models the assumption is made that the dispersed liquid and continuous gas flow field can be treated as a single phase fluid flow. This assumption can only be acceptable when the dispersed phase is made up of infinitely small droplets. In this situation the locally homogeneous flow models provide a first approximation of the spray characteristics, Faeth <sup>(21)</sup>. The basis of this approach involves the solution of Eulerian transport equations for a continuous single phase and the local state of the mixture being determined stochastically by specifying a probability density function of the mixture fraction.

The main advantage of locally homogeneous flow is that parameters which are hard to measure such as initial drop size, drop velocity do not need to be defined as part of inlet boundary conditions. The disadvantage of this model is that it is not suitable for modelling flow fields where the fluid changes phase rapidly. There is also documented evidence [Faeth <sup>(21)</sup>, Faeth <sup>(20)</sup>], that this model over predicts the spray development.

### §2.8.2 The Separated Flow Model

The separated flow models work on the basis of modelling the liquid and the gas phase separately and the interaction between the two is linked via the extra source term introduced into the gas phase transport equations. There are three categories of separated flow models, the continuous droplet model (CDM), continuous fluid model (CFM) and the discrete droplet model (DDM) Faeth <sup>(21)</sup>.

In the CDM model properties such as velocity, drop deposition, size and temperature are defined by means of a statistical distribution function. This method is generally suitable for non-evaporating sprays, since the computing power and cost would be too expensive for multi-dimensional liquid transport equation.

In CFM fluid model it is assumed that both the liquid and gas phase are Interpenetrating continua, resulting in continuous conservation transport equations for both phases. The advantage of this model is to eliminate the need for development of turbulence distribution of the dispersed phase. The disadvantage of this model is the requirement to define multiple liquid phases to account for a range of droplet sizes in real sprays.

The DDM model simulates the liquid phase stochastically by means of a series of droplets each having identical size, velocity, position, time and temperature Jain <sup>(29)</sup>, Morsi <sup>(47)</sup>. The number of drops contained within each parcel being calculated from the conservation of liquid mass. This compares well with what is known as the Monte Carlo procedure in which large number of drops in sprays are represented by a finite series of droplets. The Lagrangian formulation and its submodels are used [Dokowicz <sup>(15)</sup>, Gosman <sup>(26)</sup>, O'Rourke <sup>(52)</sup>, Dokowicz <sup>(14)</sup>, Naber <sup>(48)</sup>, Liu <sup>(42)</sup>], to describe the transient equations for the discrete liquid phase and Eulerian formulation [Wan <sup>(70)</sup>, Ranz <sup>(17)</sup>, Ranz <sup>(18)</sup>] to define gas phase transport equations. It is necessary for the Eulerian procedure to contain additional source terms to account for the introduction of the two phases in terms of momentum, mass and heat transfer. In this

model the turbulent dispersion of the droplet is simulated by using a Random-Walk approach which considers the interaction droplet particles with gas phase turbulent eddies.

The advantages of DDM model are that complex models spray phenomena, such as Collisions and break up of sprays can be modelled on modern computers.

### §2.9 Recent CFD Developments

In a recent study by Versteeg <sup>(69)</sup>, the geometry used for CFD simulations is an pMDI inhaler combined with a 3-D reconstruction of MRI scans of the oral cavity and the throat during inhalation.

The biological geometry has been imaged using a Siemens 1.5 Tesla MRI scanner Eh tezazi et al. <sup>(19)</sup>. The scan has been taken over four separate inhalations through the pMDI device, each of eight seconds duration. The point data obtained was then formatted as a CAD file. This file has used to generate the CFD mesh as shown in Figure(2.12.1)

The CFD model produced included the transient development of the aerosol plume and its interaction with the inhaled air. This interaction is brought about as a result of the plume being confined due to the pMDI mouthpiece and the throat geometry. The continuous phase, representing the inhaled airflow, the gaseous propellant, and the dispersed phase, representing the liquid propellant and drug particles, have been modelled separately and are summarised below:

### §2.9.1 The Continuous Phase

The fluid flow was computed by dividing the pMDI and the throat geometry into sub grids. The equations for the transport of mass, momentum, energy and concentration have been discretised on the sub grids and solved. The turbulence model used is a semi-empirical model. In this analysis the source terms have also been incorporated to take account of:

- Increase of gas phase mass due to evaporation of propellant droplets
- Change of gas phase momentum due to aerodynamic forces on the droplet
- Decrease of internal energy of the gas phase to supply latent heat of evaporation

### §2.9.2 The Dispersed Phase

In this section of the study the heat/mass transfer and the trajectories of the droplets are calculated. The stochastic random walk algorithm has been used to simulate the



Figure 2.9.1: The Mesh Used For CFD Analysis, Versteeg H.K, et. al, <sup>(69)</sup>

effect of turbulence on particle trajectories. The liquid propellant eventually boils away to leave the drug particles. If a dispersed phase droplet impacts a wall boundary the drug particle is deposited. Estimates of the plume properties at the spray orifice location, such as initial velocity magnitude, gas density and vapour mass fraction were found from the Fletcher <sup>(24)</sup>, Clark <sup>(10)</sup>, thermo-fluids model. In this research the Lagrangian technique to examine pMDI spray inside throat geometries, similar to the work carried out by , Stapleton et al <sup>(65)</sup> has been used. In other studies fully Eulerian approach has been adopted, where spray droplet properties are treated as continuous functions which are discretised over the same grid as gaseous phase Finlay <sup>(23)</sup>. The overall conclusion from this work was that the CFD results had shown good agreement with the experimental work of Shrubbs <sup>(63)</sup>.

### §2.10 Relevant Research

In a study carried out by Polli <sup>(53)</sup>, the following factors were thought to have the most effect on the pMDI aerosol particle size.

- Reduced spray orifice diameter
- Increased propellant vapour pressure
- Reduced drug particle size

Further studies have been carried out by Hiller <sup>(27)</sup>, on pMDIs, in order to obtain information on aerodynamic diameter of the particles. The results concluded that the diameter of the particles varied between 2.8-4.3  $\mu\text{m}$ , with a geometrical standard deviation ranging from 1.5- 2.01.

There have also been in-vivo and in-vitro studies by Moren <sup>(46)</sup>, to investigate factors influencing the deposition of pressurised aerosols With experiments which highlighted the following points:

- The increased vapour pressure, resulted in a reduced droplet size, hence increased evaporation rate. This translates into much reduced deposition of the drug into the lungs
- Increasing the volume of the drug released, increased the deposition in the airways and the lungs
- The droplet size would be reduced if the time taken for the propellant to evaporate is increased, this in turn results in the amount of drug deposited.

In a separate study by Moren <sup>(44)</sup>, particle sizes were measured at three different locations from a commercial pressurised aerosol. The method employed was laser holographic technique. The out come of their study showed that at a distance of 3cm from orifice particle sizes were as large as 36 $\mu$ m, this diameter decreased to 10.5 $\mu$ m at a distance of 28 cm from the orifice. This reduction in diameter was contributed to the evaporation of the propellant and separation of the drug particle.

In a study carried out by Dhand <sup>(13)</sup> high speed photography technique was used, to study the effects of jet cone angle, spray distribution and mean jet velocity. the study reports that the characteristics remained constant for the different formulations studied. The results are tabulated in Table(2.2).

Total Spray Duration	65-95 ms
Cone Angle	66 <sup>0</sup> -75 <sup>0</sup>
Ejected Mean Velocity	13-15m/s

Table 2.2 The Effects of Jet Cone Angle

The availability of laser Doppler (LDA) has allowed parameters, such as, axial velocity to be measured with respect to time. One of the groups working in this area

Lee <sup>(40)</sup>, have measured axial drop velocities for a range of different pressurised canisters. The group has also used laser sheet photography to study the spray structures. In the part of the study dealing with velocity variations the velocity was resolved over a 30ms duration and then calculating ensemble-means over numerous actuations, as an example Figure(2.10.1) shows the temporal variations of the axial droplet velocity for propellant 11/12 formulation (30%/70% wt/wt) with surfactant to drug weight ratio of 1/10. The spray velocity, at 5mm from the mouthpiece was found to remain constant for the first half of the spray, but it decays rapidly with fluctuations indicating high levels of turbulence.

It was also concluded from the laser sheet photography study that, in the region immediately downstream of the mouthpiece, the shape and vortices of the spray were well defined.

The peak exit velocity measured by Clark <sup>(10)</sup>, using a pressure transducer, were measured at a distance of 3cm from the orifice using a propellant-134a with different orifice diameter ratios. The range of velocity values measured were between 35-70m/s, the scatter of the data being due to the variability of the exit velocity measurement.

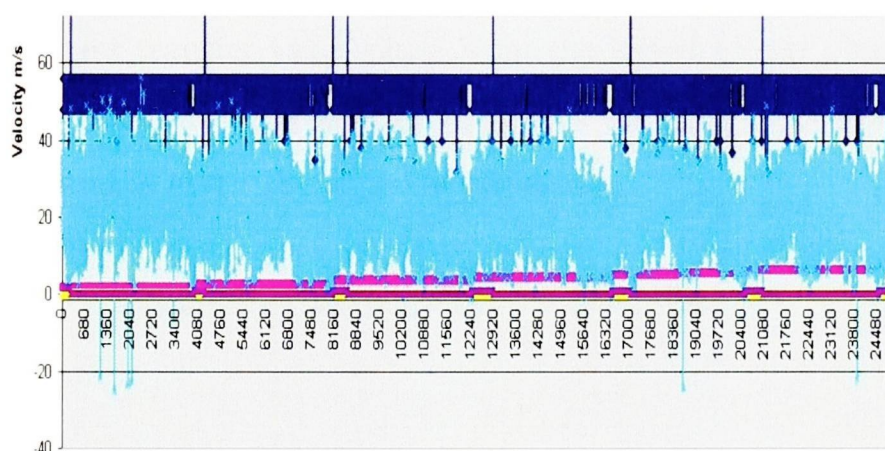


Figure 2.10.1: Turbulent Velocity Fluctuations

## §2.11 Spray Analysis From a pMDI

The work produced by York <sup>(73)</sup>, which studied the spray formation by flash evaporation with reference to cosmetic aerosols, the following four stages in spray formation were highlighted.

- The primary atomisation process starts by flash evaporation and continues by shearing due to high velocity gradients to produce ligaments
- The secondary atomisation due to aerodynamic forces produces drops
- Evaporation
- Entrainment

The observations did not show spray being projected in all Direction which is a characteristic of the flash dominant spray process.

The term flash evaporation has been described by Wiener <sup>(71)</sup>, as the instantaneous transformation of liquid phase into vapour due to sudden decrease in pressure. This sudden change does not allow heat transfer to take place between the gas and liquid phase, however mass transfer takes place from the liquid to gas phase. There have been heat balance calculations preformed to predict the percentage mass of propellant that could flash, and is given the following equation:

$$(mass_{flash})\% = \frac{C_{pi}(T_l - T_{wb})}{h_{fg}} X 100 \quad (2.11.1)$$

There have been other explanations for the process of flash evaporation for example Brown <sup>(5)</sup>, defined this process in relation to nucleation. The materials they used were water and Freon 11, however the correlations they obtained only showed good agreement for water. Their theory was based on the assumption that, due to surface irregularities in the orifice, low pressure eddies are formed which are regularly shed.

The eddies are moved downstream by the jet and act as low pressure stagnation regions. These stagnation regions then form bubbles which burst and disintegrate the jet.

In the theoretical field, Sher<sup>(61)</sup>, developed a mathematical model to describe the size of drops produced by flash evaporation. The theoretical model was validated experimentally using a mixture of Toluene and Freon 22. The experimental results did not agree well with those produced by the theory, simply because the theory had over simplified the process, for example, in the theory, thermal equilibrium was assumed. However there were some useful findings obtained from the experimental results, for example the experimental results showed that the nozzle geometry did not have a noticeable effect on the size of the drop. The other finding was that, the increase in liquid pressure reduced the average drop size until a critical value was reached for pressure where the size of the drop was no longer affected.

There has been a review on two phase flashing jets published by Appleton<sup>(2)</sup>, which can be divided into the following categories:

- Slip flow model slip considered
- Disequilibrium models - both relative and non-linear thermodynamics considered
- Homogeneous equilibrium model- which assumes complete equilibrium

The conclusion from this extensive review was that all models were far too simplified, hence no single model would be describing the process fully. The atomisation process was then thought to be a combination of flashing and aerodynamic forces, which depends on the degree of superheat, back pressure and nozzle geometry. There is a factor known as the flashing criteria  $\epsilon$  which is described by the following equation

$$\epsilon = \frac{T_{sh} - T_{sat}}{T_{sh}} \quad (2.11.2)$$

---

$$0.07 < \epsilon < s0.1$$

- $T_{sh}$  is the shattering temperature
- $T_{sat}$  the saturation temperature

The results obtained are within order of magnitude accuracy of the experimental data presented by Brown <sup>(5)</sup>. The most detailed study of flash evaporation in relation to pMDIs has been carried out by Clark <sup>(10)</sup>. This study has looked at various factors affecting the atomisation process. The conclusions from this study indicated that formulation and nozzle design were the most significant parameters affecting the atomisation process.

The findings from this research have highlighted three different flow regimes which were present during metered discharge through pMDI, these are as follow:

- Valve Orifice Flow: the flow is initially a single phase discharge from the nozzle, which then undergoes from a single phase to a two phase flow as bubbles are formed which fill the metering chamber.
- Expansion Chamber: The fluid flow in the expansion chamber is a two phase flow. The resident air in the chamber is expelled by the ever increasing pressure.
- Spray Flow: The assumption with flows in this region was that, they are two phase in nature. The equilibrium models developed to describe the mass discharge through the orifice were found to compare well with the experimental results confirming the assumption that flows through the orifice were in equilibrium.

## Computational Fluid Dynamics (CFD)

*This chapter sets out by defining the term CFD, and components which make the present day commercial CFD code. The governing equations and various turbulence models used in this study are described. The discrete phase model which forms an important part of this research is described in detail.*

### §3.1 Introduction

The use of numerical methods to solve the partial differential equations governing the flow of fluid has become a popular research tool. This technique is commonly referred to as Computational Fluid Dynamics (CFD), [Versteeg<sup>(68)</sup>].

The current study was undertaken using the commercial code Fluent version 5.3.18 . The code is made up of three separate components which are as follows:

- Pre-processor
- Solver
- Post processor

The Pre-processor is the component which allows the user to define the input of a flow problem to a CFD program by means of an interface and subsequently this information is transformed into a form suitable for use by the solver. The types of information required at this stage are:

- The computational domain
- Grid generation
- Physical or chemical process to be modelled
- Specification of boundary conditions

The solvers use different techniques to solve the partial differential equations, this is generally dependent on the commercial code used. There are four main techniques used in commercial codes. These are finite difference, finite element, finite volume and spectral methods. In general, the numerical methods which form the basis of the solver Perform the following steps:

- Approximation of the unknown flow variables by means of solving the full partial differential equations
- Discretisation of the governing equations
- Solution of the algebraic equations

At this stage it is worthwhile mentioning the difference between various numerical techniques mentioned above. In general the difference is in the way the flow variables are approximated and the way in which discretisation process is carried out.

In the finite difference technique the unknown variable  $\phi$  is defined at the node points of a grid lines. The truncated form of Taylor series is often used to formulate finite difference approximation of derivatives of  $\phi$  in terms of point samples of  $\phi$  at

---

each grid point and its immediate neighbours. Those derivatives appearing in the governing equations are replaced by finite differences yielding an algebraic equation for the value of  $\phi$  at each grid point, [Ferziger <sup>(22)</sup>]

In the finite element method the local variations of flow variables is described by applying a simple piecewise function. This approach determines the solution for the variable  $\phi$ , hence satisfying the governing equations. At this stage if the piecewise approximating functions for  $\phi$  are substituted into the equation it will not hold exactly and a residual is defined as a measure of error. the errors. The next step is to minimize the residuals by multiplying them by a set of weighting functions and integrating. This procedure results in a set of algebraic equations for the unknown coefficients of the approximating functions. The finite element technique was developed initially for the structural analysis, however Zienkiewicz and Taylor, <sup>(74)</sup> have applied this technique to fluid applications.

In the Spectral Analysis method the unknown variables are approximated by means of a truncated Fourier series. These approximations are valid throughout the computational domain. The variables are placed back in the governing equations using a truncated series. The constraint that leads to the algebraic equations for the coefficients of the Fourier series is provided by a weighted residuals concept similar to the finite element method or by making the approximate function coincide with the near exact solution at a number of grid points.

The finite volume method was developed as a special form of finite difference Formulation. This technique is well established and is commonly used in CFD codes. The numerical scheme consists of the following procedure:

- The governing equations of fluid flow are integrated over all the control volumes.
- Discretisation involves the substitution of a variety of finite-volume approximations for the terms in the equations representing processes such as convection, diffusion and sources. This converts the integral equations into a system of

algebraic equations.

- Solution of the algebraic equations by an iterative method.

The distinguishing feature of finite volume method is the way in which the governing equations are integrated over the control volume.

### §3.1.1 Post Processor

The leading CFD codes are all capable of displaying the data in a variety of formats:

- Domain geometry and grid display
- Vector plots, line and shaded contour plots
- 2D and 3D surface plots
- Particle tracking
- Colour postscript output

### §3.2 Governing Equations

The governing equations for continuum physical phenomena such as fluid flow, heat transfer, and solid mechanics can be expressed in the following generalized form:

$$\frac{\partial}{\partial t}(\rho A \phi) + \nabla \cdot Q = \nabla \cdot (\Gamma \nabla Q) + S \quad (3.2.1)$$

	$\phi$	A	$\Gamma$	S	Q
Mass	1	1	0	0	$\rho\nu$
Momentum	v	1	$\Gamma$	$-\nabla P$	$\rho\nu v$
Temperature	h	1	k/c	S	$\rho\nu h$
Concentration	z	1	D	0	$\rho\nu z$

Table 3.2.1 The Governing Equations

### §3.3 Turbulent Flow

#### §3.3.1 Introduction

Turbulent flows are characterized by fluctuating velocity fields. This in turn causes fluctuations of transport quantities such as momentum, energy and species concentration. The fluctuations are small in scale and high in frequency, hence computationally too expensive to simulate directly in practical situations.

The instantaneous governing equations can be time-averaged, ensemble- average or otherwise manipulated to remove the small scales, resulting in a modified set of equations that are less computationally expensive to solve. The new equations contain additional unknown variables which can be determined in terms of known quantities.

### §3.4 Turbulence Models

#### §3.4.1 Introduction

A turbulence model is a means of defining a wide range of flow problems computationally. For most engineering purposes it is necessary to resolve the details of the

turbulent fluctuations. It therefore becomes important for a turbulence model to be applicable in a wide range of flow conditions. It needs to be accurate, and economical to run. The most common turbulence models are classified in Table(3.3.1).

Classical Models	Based on Time averaged Reynolds Equations
	1-Mixing Length Model [Rodi <sup>(58)</sup> ]
	2- Two Equation K- <i>epsilon</i> Model [Launder <sup>(38)</sup> ]
	3- Reynolds Stress Model [Launder <sup>(39)</sup> ]
	4- Algebraic Stress Model [Demuren <sup>(12)</sup> ]
Large Eddy Simulations	Based on Space-filtered Equations

Table 3.3.1 Summary of Turbulence Models Available

In the course of the current research, comparisons were made between three different turbulence models. These are described below:

#### §3.4.2 k- $\epsilon$ Model

The simplest and the at the same time most complete models of turbulence are two-equation models in which the solution of two separate transport equations are determined. The standard k- $\epsilon$  model, Launder <sup>(38)</sup>, is based on model transport equations for the turbulent kinetic energy (k) and its dissipation rate ( $\epsilon$ ). The model transport equation for k is derived from the exact equation, while model transport equation for  $\epsilon$  was obtained using physical reasoning and bears little resemblance to its mathematically exact counterpart.

The assumption made in deriving the k- $\epsilon$  model was that the flow is fully turbulent,

---

and the effects of molecular viscosity are negligible, hence making the standard  $k-\epsilon$  model suitable for fully turbulent flows. In this turbulence model the effect of turbulence can be represented as an increased viscosity. This leads to the eddy viscosity model:

$$-\rho \overline{u_i u_j} = \mu_t \left( \frac{\partial \overline{u_i}}{\partial x_j} + \frac{\partial \overline{u_j}}{\partial x_i} - \frac{2}{3} \rho \delta_{ij} k \right) \quad (3.4.1)$$

$$-\rho \overline{u_j \phi} = \Gamma_t \frac{\partial \overline{\phi}}{\partial x_j} \quad (3.4.2)$$

In equation (3.3.1),  $k$  is the turbulent kinetic energy, which is equal to

$$k = \frac{1}{2} \overline{u_i u_i} = \frac{1}{2} (\overline{u_x u_x} + \overline{u_y u_y} + \overline{u_z u_z}) \quad (3.4.3)$$

The phenomenon of turbulence is a difficult quantity to describe, hence the best approach for computing turbulence would be with the aid of partial differential equations. It is accepted that turbulence can be described with a minimum of two parameters namely velocity scale and a length scale, therefore any model which derives the needed quantities is the logical choice. In the two equation  $k-\epsilon$  model the following equations for  $k$  and  $\epsilon$  are used.

$$\begin{aligned} \frac{\partial(\rho k)}{\partial t} + \frac{\partial(\rho \overline{u_j k})}{\partial x_j} &= \frac{\partial}{\partial x_j} \left( \mu \frac{\partial k}{\partial x_j} \right) - \frac{\partial}{\partial x_j} \left( \frac{\rho}{2} \overline{u_j u_i u_i} + \overline{P u_j} \right) \\ &\quad - \rho \overline{u_i u_j} \frac{\partial \overline{u_i}}{\partial x_j} - \mu \frac{\partial \overline{u_i}}{\partial x_k} \frac{\partial \overline{u_i}}{\partial x_k} \end{aligned} \quad (3.4.4)$$

The terms on the left side of equation(3.4.4) and the first term on the right need no modelling. The last term represents the product of the density  $\rho$  and the dissipation where,  $\epsilon$  can be represented by equation(3.3.5).

$$-\left( \frac{\rho}{2} \overline{u_j u_i u_i} - \overline{P u_j} \right) \approx \frac{\mu_t}{\sigma_k} \frac{\partial k}{\partial x_j} \quad (3.4.5)$$

The second term on the right represents turbulent diffusion of kinetic energy, which in simple terms is the transport of velocity fluctuations by the fluctuations themselves. This is always modelled by use of a gradient diffusion assumption, where  $\mu_t$  is eddy viscosity defined above and  $\sigma_k$  is a turbulent Prandtl number, whose value is approximately unity. The third term of the right side of equation(3.3.4) represents the rate of production of turbulent kinetic energy by the mean flow, a transfer of kinetic energy from the mean flow to the turbulence. The application of eddy viscosity hypothesis to estimate the Reynolds stress, results in equation(3.3.3):

$$P_k = -\overline{\rho u_i u_j} \frac{\partial \overline{u_i}}{\partial x_j} \approx \mu_t \left( \frac{\partial \overline{u_i}}{\partial x_j} + \frac{\partial \overline{u_j}}{\partial x_i} \right) \frac{\partial \overline{u_i}}{\partial x_j} \quad (3.4.6)$$

In this situation all the terms can be calculated from quantities that will be computed, hence the development of the turbulent kinetic energy equation is complete. The governing equation for the dissipation rate is as follow:

$$\frac{\partial(\rho\epsilon)}{\partial t} + \frac{\partial(\rho u_j \epsilon)}{\partial x_j} = C_{\epsilon 1} P_k \frac{\epsilon}{k} - \rho C_{\epsilon 2} \frac{\epsilon^2}{k} + \frac{\partial}{\partial x_j} \left( \frac{\mu_t}{\sigma_\epsilon} \frac{\partial \epsilon}{\partial x_j} \right) \quad (3.4.7)$$

The eddy viscosity can be expressed as :

$$\mu_t = \rho C_\mu \sqrt{k} L = \rho C_\mu \frac{k^2}{\epsilon} \quad (3.4.8)$$

The two equations for  $k$  and  $\epsilon$  define the turbulence model widely known as the k- $\epsilon$  model. The model contains five constants, and the most commonly used values are listed:  $C_\mu = 0.09$ ,  $C_{\epsilon 1} = 1.44$ ,  $C_{\epsilon 2} = 1.92$ ,  $\sigma_k = 1.0$ ,  $\sigma_\epsilon = 1.3$

### §3.5 The RNG k- $\epsilon$ Model

The origins of the RNG based k- $\epsilon$  model is from the instantaneous Navier-Stokes equations, using a mathematical technique called renormalization group (RNG) methods. This analytical approach results in a model with constants different from those in the standard k- $\epsilon$  model, and additional terms and functions in the transport

---

equations for k and  $\epsilon$ .

### §3.5.1 Governing Equations for the RNG k- $\epsilon$ Model

It can be seen at first glance (Choudhury <sup>(8)</sup>) that the RNG k- $\epsilon$  model is similar in form to the k- $\epsilon$  model.

$$\rho \frac{\partial k}{\partial t} = \frac{\partial}{\partial x_i} (\alpha_k \mu_{eff} \frac{\partial k}{\partial x_i}) + G_k + G_b - \rho \epsilon Y_M \quad (3.5.1)$$

A similar equation for the dissipation rate  $\epsilon$  can be written as follow:

$$\rho \frac{\partial \epsilon}{\partial t} = \frac{\partial}{\partial x_i} (\alpha_\epsilon \mu_{eff} \frac{\partial \epsilon}{\partial x_i}) + C_{1\epsilon} \frac{\epsilon}{k} (G_k + C_{3\epsilon} G_b) - C_{2\epsilon} \rho \frac{\epsilon^2}{k} R \quad (3.5.2)$$

The symbols are defined below:

- $G_k$  represents the generation of turbulent kinetic energy due to the mean velocity gradients
- $G_b$  is the generation of turbulent kinetic energy due to buoyancy
- $Y_M$  contribution of the fluctuating dilation in compressible turbulence to the overall dissipation rate
- $\alpha_k$ , and  $\alpha_\epsilon$  are the inverse effective Prandthl numbers for k and  $\epsilon$  respectively

### §3.6 The RNG and The k- $\epsilon$ Model

The main difference between the RNG and standard k- $\epsilon$  models is the presence of additional term R (Choudhury <sup>(8)</sup>) in the  $\epsilon$  equation given by equation (3.5.2):

$$R = \frac{C_\mu \rho \eta^3 (1 - \eta/\eta_o) \epsilon^2}{1 + \beta \eta^3} \frac{1}{k} \quad (3.6.1)$$

$$\eta \equiv Sk/\epsilon, \eta_0 = 4.38, \beta = 0.012$$

The effect of this term becomes more apparent if the equation is rewritten in the following format:

$$\rho \frac{\partial \epsilon}{\partial t} = \frac{\partial}{\partial x_i} (\alpha_\epsilon \mu_{eff} \frac{\partial \epsilon}{\partial x_i}) + C_{1\epsilon} \frac{\epsilon}{k} (G_k + C_{3\epsilon} G_b) - C_{2\epsilon}^* \rho \frac{\epsilon^2}{k} \quad (3.6.2)$$

Where  $C_{2\epsilon}^*$

$$C_{2\epsilon}^* \equiv C_{2\epsilon} + \frac{C_\mu \rho \eta^3 (1 - \eta/\eta_0)}{1 + \beta \eta^3} \quad (3.6.3)$$

The significance of the above equation becomes apparent in certain situations. In the first instance when the value of  $\eta < \eta_0$ , the term R makes a positive contribution, and  $C_{2\epsilon}^*$  becomes larger than  $C_{2\epsilon}$ . In other flow conditions such as in the logarithmic layer, the values obtained with the RNG model gives results which are close in value to those obtained from the standard k- $\epsilon$  model. In flow conditions where there are regions of large strain rates  $\eta > \eta_0$ , the term R makes a negative contribution, hence the value of  $C_{2\epsilon}^*$  is less than  $C_{2\epsilon}$ . In this situation if the model is compared with the standard k- $\epsilon$  model, the smaller destruction of  $\epsilon$ , augments  $\epsilon$  reduces k and eventually the effective viscosity. The conclusion from the various flow conditions described is that, the RNG model is best suited for rapidly changing flows compared to the k- $\epsilon$  model. The values of the constants used in the RNG model are derived from the RNG theory.

### §3.7 The k- $\epsilon$ Realizable Model

The term realizable indicates that the model is capable of satisfying constraints on the normal stresses, which are consistent with the physics of turbulent flow, (T.H. Shih <sup>(62)</sup>) The main reasons for introducing the k- $\epsilon$  Realizable model was to address the short falls of the standard k- $\epsilon$  model. In order to understand the need for the k- $\epsilon$  RNG model we need to start by combining the Boussinesq relationship and the definition of the eddy viscosity, so that a new relationship for the normal Reynolds

stress in an incompressible strained mean flow can be obtained.

$$\overline{u^2} = \frac{2}{3}k - 2\nu_t \frac{\partial U}{\partial x} \quad (3.7.1)$$

In the condition where  $\nu_t \equiv \mu_t/\rho$  the value of the normal stress  $\overline{u^2}$  becomes non-Realizable or negative when the strain rate satisfies the following equation:

$$\frac{k}{\epsilon} \frac{\partial U}{\partial x} > \frac{1}{3C_\mu} \approx 3.7 \quad (3.7.2)$$

There is also another situation in which the inequality referred to as Schwarz inequality for shear stresses  $\overline{u_\alpha u_\beta^2} \leq \overline{u_\alpha^2 u_\beta^2}$  can be violated. The procedure to ensure the positivity of normal stresses and the Schwarz inequality for shear stresses is to allow the variable  $C_\mu$  sensitive to mean flow and the turbulence k-  $\epsilon$ . This procedure is suggested by many researchers Reynolds <sup>(56)</sup>. The values obtained for  $C_\mu$  are validated experimentally and as an example its value is reported to be around 0.09 for equilibrium boundary layer and 0.05 for strong homogeneous shear flows. In the standard k $\epsilon$  model the ability to predict round jets is quite good, however the problem starts when there is a need to predict the expansion rate in an axisymmetric jet. This inability to predict the expansion rate is thought to be related to the equation used for the prediction of  $\epsilon$ . In order to develop a more accurate model RNG model was formulated by Shih <sup>(62)</sup>.

- Introduction of a new eddy-viscosity equation involving a variable  $C_\mu$  suggested by Reynolds <sup>(56)</sup>
- Formulation of a new equation for dissipation rate  $\epsilon$  based on the dynamic equation of the mean square vorticity fluctuations.

### §3.8 The Realizable k- $\epsilon$ Model Equations

The governing equations for the k- $\epsilon$  RNG model are

For k

$$\rho \frac{\partial k}{\partial t} = \frac{\partial}{\partial x_j} \left( \mu + \frac{\mu_t}{\sigma_k} \right) \frac{\partial k}{\partial x_j} + G_k + G_b - \rho \epsilon Y - M \quad (3.8.1)$$

and for  $\epsilon$

$$\rho \frac{\partial \epsilon}{\partial t} = \frac{\partial}{\partial x_j} \left[ \left( \mu + \frac{\mu_t}{\sigma_\epsilon} \right) \frac{\partial \epsilon}{\partial x_j} \right] + \rho C_1 S_\epsilon - \rho C_2 \frac{\epsilon^2}{k + \sqrt{\nu \epsilon}} + C_{1\epsilon} \frac{\epsilon}{k} C_{3\epsilon} G_b \quad (3.8.2)$$

where

$$C_1 = \max\left[0.43, \frac{\eta}{\eta+5}\right] \text{ and}$$

$$\eta = Sk/\epsilon$$

In the above equations the symbols have the same meaning as already explained for the k- $\epsilon$  model in section(3.4.2). The points to notice are that the equation for k is the same as that in the standard k- $\epsilon$  and the RNG model. However the equation for the variable  $\epsilon$  is quite different from the standard and the RNG k- $\epsilon$  models. The two major differences are that the production term in the  $\epsilon$  equation does not involve the production of k as in the other k- $\epsilon$  models. The other striking feature of the RNG model compare with other k- $\epsilon$  models is that the last term of the equation for  $\epsilon$  does not vanish, even if the value of k becomes zero, as there is no k term in the denominator. This model has been validated by researchers Shih <sup>(62)</sup>, Kim <sup>(36)</sup> for a variety of test cases and has shown to predict the flows accurately. It should be noted however, that turbulence models are very sensitive to boundary conditions and these parameters play a major role in determining the accuracy of the model.

#### §3.8.1 The Turbulent Viscosity

The eddy viscosity is modelled in the same way as for the k-  $\epsilon$  model, so it will not be repeated here again. It has already been mentioned that the term  $C_\mu$  is not a

constant term in the Realizable model, therefore an equation in the following form has been defined to obtain a relationship for  $C_\mu$

$$C_\mu = \frac{1}{A_0} + A_s \frac{U^* k}{\epsilon} \quad (3.8.3)$$

where

$$U^* \equiv \sqrt{S_{ij}S_{ij} + \tilde{\Omega}_{ij}\tilde{\Omega}_{ij}} \text{ and}$$

$$\tilde{\Omega}_{ij} = \Omega_{ij} \epsilon_{ijk} \omega_k$$

$$\overline{\Omega}_{ij} = \overline{\Omega}_{ij} - \epsilon_{ijk} \omega_k$$

$\overline{\Omega}_{ij}$  is the mean rate of rotation tensor viewed in a rotating reference frame with angular velocity  $\omega_k$ . The model constants  $A_0$  and  $A_s$  is given by  $A_0 = 4.04$ ,  $A_s = \sqrt{6 \cos \phi}$ .

The relation for  $\phi$  is in the form  $\phi = \frac{1}{3} \arccos(\sqrt{6W})$  and  $W$  can be defined by the relationship  $W = \frac{S_{ij}S_{jk}S_{ki}}{\tilde{S}}$

$$\tilde{S} = \sqrt{S_{ij}S_{ij}}$$

The term  $S_{ij} = \frac{1}{2}(\frac{\partial u_j}{\partial x_i} + \frac{\partial u_i}{\partial x_j})$ . The above equations indicate that  $C_\mu$  is related to the mean strain and rotation rates, and the turbulence fields  $k$  and  $\epsilon$ .

#### §3.8.2 Model Constants

The model constants have been established, to ensure optimum performance for the Realizable model. These constants are:

$$C_{1\epsilon} = 1.44, C_2 = 1.9, \sigma_k = 1.0, \sigma_\epsilon = 1.2$$

#### §3.8.3 The Production of Turbulence in k- $\epsilon$ Models

The production of turbulent kinetic energy defined by the symbol  $G_k$  is modelled in exactly the same way for the standard k- $\epsilon$ , RNG and the Realizable k- $\epsilon$  models. A

definition for the term  $G_k$  is shown as follow:

$$G_k = -\rho \overline{u'_i u'_j} \frac{\partial u_j}{\partial x_i} \quad (3.8.4)$$

The value of  $G_k$  can be obtained by the following equation:

$$G_k = \mu_t S^2 \quad (3.8.5)$$

The value of S the modulus of the mean rate of strain is given by

$$S \equiv \sqrt{2S_{ij}S_{ij}} \quad (3.8.6)$$

The value of  $S_{ij}$  can be obtained from:

$$S_{ij} = \frac{1}{2} \left( \frac{\partial u_i}{\partial x_j} + \frac{\partial u_j}{\partial x_i} \right) \quad (3.8.7)$$

#### §3.8.4 Buoyancy Effects on k- $\epsilon$ Models

In situations where the gravity is computed and there is a temperature gradient present, the turbulence models need to take into account the production of k due to buoyancy hence contributing to the production of  $\epsilon$ .

$$G_b = \beta_{gi} \frac{\mu_t}{Pr_t} \frac{\partial T}{\partial x_i} \quad (3.8.8)$$

In the case of the Realizable model the Prandtl number for energy needs to be defined, in terms of  $\alpha_0 = k/\mu c_p$ . The coefficient of thermal expansion,  $\beta$ , is given by the following equation:

$$\beta = -\frac{1}{\rho} \left( \frac{\partial \rho}{\partial T} \right)_p \quad (3.8.9)$$

The effects of buoyancy need to be considered when there is a non zero temperature gradient or a nonzero gravity field. In stable stratification conditions the effect of turbulence is suppressed. In general the buoyancy effects in the equation for  $k$  are well defined, however for the  $\epsilon$  equation, this needs to be calculated from the following equation:

$$C_{3\epsilon} = \tanh \left| \frac{v}{u} \right| \quad (3.8.10)$$

In the above equation  $v$  is taken to be the component of the flow velocity parallel to the gravitational vector and  $u$  is the component of the flow velocity perpendicular to the gravitational vector. This would mean that the value for  $C_{3\epsilon}$  will be set to 1 in buoyant shear layers where the main flow direction is aligned with the direction of gravity. The value of  $C_{3\epsilon}$  will be zero for buoyant shear layers which are perpendicular to the gravitational vector.

## §3.9 Wall Bounded Turbulent Flows

### §3.9.1 Introduction

The presence of a wall in a turbulent flow significantly affects the flow feature, as an example one can think of the mean velocity field which is affected through the no-slip condition which has to be satisfied. In situations close to the wall accurate representation of the flow is required for accurate predictions, since in such regions flow variables change rapidly. The wall region is divided into three zones:

- The viscous sub layer, where the flow is laminar
- The outer region where the flow is fully turbulent
- The transition region where the effects of molecular viscosity and turbulence are equally important. It is therefore important to make adjustments to the

turbulence models already described, so that they can be readily applied to wall bounded flows.

#### §3.9.2 Wall Function

The purpose of applying the wall function is to bridge the viscosity affected region between the wall and the fully-turbulent region. In high Reynolds number flows, the application of wall function reduces the computational time, hence it is widely used in industrial simulations. The commonly used wall function was proposed by Launder <sup>(38)</sup> It has been found that the wall function is not adequate where low Reynolds Viscous effects are dominant. In mathematical form of the standard wall function is described as follow:

$$U^* = \frac{1}{k} \ln(Ey^*) \quad (3.9.1)$$

where:

$$U^* \equiv \frac{U_p C_\mu^{1/4} k_p^{1/2}}{\tau_w / \rho} \quad (3.9.2)$$

$$y^* \equiv \frac{\rho C_\mu^{1/4} k_p^{1/2} y_p}{\mu} \quad (3.9.3)$$

k Von Karmans cn (constant)

E empirical constant (9.81)

$U_p$  - mean velocity of fluid at point P

$K_p$  - turbulent kinetic energy at point P

$Y_p$  distance from point P to the wall

$\mu$  - dynamic viscosity of the fluid

In the commercial code Fluent, used for this research, the laws of the wall for mean

velocity and temperature are based on the wall unit  $y^*$ , rather than  $y^+ \equiv \rho u_\tau y / \mu$ .

## §3.10 Discrete Phase Models

### §3.10.1 Introduction

The discrete phase is in a Lagrangian frame of reference, and is made up of spherical particles, which are either represented as droplets or bubbles injected in the continuous phase. In this model the heat and mass transfer to and from the particles as well as their trajectories are calculated. The applications for this type of modelling cover a wide range of industrial problems such as combustion, spray drying and aerosol dispersion. In the commercial code Fluent, used for this study, the following discrete phase model options are available.

- The use of Lagrangian formulation to calculate the discrete trajectory
- Heating/cooling of discrete phase
- Vaporization and boiling of liquid droplets
- Turbulent effects of particles

### §3.11 Equation Of Motion For Particles

The trajectory of a discrete phase particles can be predicted by integrating the force balance on the particle, which is written in a lagrangian reference frame. The force balance equation balances the particle inertia with the forces acting on the particle and can be written for the x- direction as:

$$\frac{du_p}{dt} = F_D(uu_p) + g_x(\rho_p - \rho)/\rho_p + F_x \quad (3.11.1)$$

where  $F_D(uu_p)$  is the drag force per unit particle mass. A relationship for  $F_D$  can be written as follows:

$$F_D = \frac{18\mu}{\rho_p D_p^2} \frac{C_D Re}{24} \quad (3.11.2)$$

where

$u$  is the fluid velocity

$u_p$  is the particle velocity

$\mu$  is the molecular viscosity

$\rho$  fluid density

$\rho_p$  is the density of the particle

$D_p$  diameter of the particle

$Re$  is the relative Reynolds number

$$Re = \frac{\rho D_p |U_P - u|}{\mu} \quad (3.11.3)$$

The value for  $C_D$  can be obtained from the following equation:

$$C_D = a_1 + \frac{a_2}{Re} + \frac{a_3}{Re^2} \quad (3.11.4)$$

The values for constants are given by Morsi<sup>(47)</sup> for a range of Reynolds numbers for smooth spheres.

### §3.12 Stochastic Particle Tracking

In turbulent flow conditions the particle trajectories are calculated using the mean fluid velocity  $\bar{u}$  the equation(3.11.1). In order to predict the particle dispersion caused by turbulence, an equation containing the instantaneous value of the fluctuating flow

velocity needs to be included.

$$u = \bar{u} + u' \quad (3.12.1)$$

#### §3.12.1 Integration Of The Trajectory Equations

The trajectory and auxiliary equations are solved by stepwise integration over discrete time steps. The integration of the force balance equation gives:

$$\frac{dx}{dt} = u_p \quad (3.12.2)$$

In the integration process the fluid velocity,  $u$ , is taken as the velocity at the particle position which is obtained from the stored cell centre velocity. The assumption that the term containing the body force remains constant over each small time interval, the trajectory equation can be written as:

$$\frac{du_p}{dt} = (u - u_p)\alpha \quad (3.12.3)$$

where  $1/\alpha$  is the particle relaxation time. The Equations(3.12.2) and (3.12.3) are solved simultaneously to determine the position and the velocity of the particle at any given time.

#### §3.13 Droplet Size Distribution

As far as the sprays are concerned the size distribution of the droplets is given By the Rosin-Rammler expression. where  $\bar{D}$  is the size constant,  $D$  is the particle diameter and  $n$  is the size distribution parameter.

$$M_D = \exp(-[(D/\bar{D})^n]) \quad (3.13.1)$$

### §3.14 Discrete Random Walk Tracking

In the stochastic tracking approach the turbulent dispersion of particles is obtained by integrating the trajectory equations for individual particles, using the instantaneous fluid velocity,  $\bar{u} + u'(t)$ , along the particles path. This procedure is repeated for a number of particles, in order to obtain an overall picture of the particle dispersion. This model is not suitable for diffusion dominated flows.

#### §3.14.1 Prediction Of Particle Dispersion

The particle dispersion is predicted using the idea of integral time scale,  $T$ , which represents the time spent by the particle in turbulent motion.

$$T = \int_0^{\infty} \frac{u'_p(t)u'_p(t+s)}{\overline{u_p'^2}} ds \quad (3.14.1)$$

The integral is a proportional to the rate of particle dispersion, hence the greater the value of the integral, the more turbulent the flow. A relationship needs to be established for smaller particles which move with the fluid. In this situation the integral time becomes the fluid Lagrangian integral time  $T_L$ . This relationship is approximated by the following relationship:

$$T_L = C_L \frac{k}{\epsilon} \quad (3.14.2)$$

In the above equation the value of  $C_L$  needs to be determined, therefore the above equation can be simplified by matching the diffusivity of tracer particles,  $\overline{u_i u_j} T_L$  to the scalar diffusion rate estimated by the turbulence model  $\nu_t / \sigma$ . For the standard k- $\epsilon$  model the value of  $T_L$  is obtained from the following equation;

$$T_L \approx 0.15 \frac{k}{\epsilon} \quad (3.14.3)$$

### §3.14.2 Discrete Random Walk Model

In the Discrete Random Walk model the interaction of a particle with the succession of discrete phase turbulent eddies is simulated. The eddies are characterized by:

- a time scale  $\tau_e$
- a Gaussian distributed random velocity fluctuations,  $u'$ ,  $v'$  and  $w'$  whose values are sampled assuming they obey the Gaussian probability distribution

where

$$u' = \zeta \sqrt{u'^2} \quad (3.14.4)$$

A similar relationship for other directions can be obtained. The right hand side of the equation is the rms value of the velocity fluctuations and the term  $\zeta$  is a random number. The characteristic eddy lifetime is defined either as a constant:

$$\tau_e = 2T_L \quad (3.14.5)$$

A relationship for the value of  $T_L$  is determined by the Equation(3.14.3).

### §3.15 Particle Types

There are a variety of particles which can be modelled in discrete phase simulations. The type of particle used would determine what laws are applicable. A list of particle types available is given in Table(3.14).

Particle Type	Description	Laws Required
Inert	Inert heating or cooling	1,6
Droplet	heating/evaporating/boiling	1,2,3,6

Table(3.14) Particle Types Used In this Research

### §3.15.1 Inert Heating or Cooling

The inert heating and cooling laws are applicable in situations where the volatile fraction  $f_{vo}$  has been consumed and the temperature of the particle is less than the defined vaporization temperature  $T_{vap}$ . Mathematically the relationships described can be written as Law 1:

$$T_p < T_{vap} \quad (3.15.1)$$

Law 6:

$$m_p \leq (1 - f_{vo})m_{p0} \quad (3.15.2)$$

$T_p$  is the particle temperature

$m_{p0}$  is the initial mass of the particle

$m_p$  is the current mass of the particle

$f_{vo}$  volatile Fraction

The droplet continues to obey the Law 1 until its temperature reaches that of vaporization, at which point the droplet obeys one of the mass transfer laws 2, 3, 4 and 5 until the volatile fraction of the droplet is no longer active. The droplet then returns to a state where law 6 is applicable. When either law 1 or law 6 is applied to a droplet a relationship taking into account the particle temperature  $T_p(t)$  and convective heat transfer at the particle surface is derived as follow:

$$m_p c_p \frac{dT}{dt} = h A_p (T_\infty - T_p) + \epsilon_p A_p \sigma (\theta_R^4 - T_p^4) \quad (3.15.3)$$

where  $m_p$  mass of particle (kg)

$c_p$  heat capacity of the particle (J/kg-K)

$A_p$  surface area of the particle (m<sup>2</sup>)

$T_\infty$  local temperature of the continuous phase (K)

$h$  convective heat transfer coefficient (W/m<sup>2</sup>-K)

$\epsilon_p$ - particle emissivity

$\sigma$ - Boltzman constant

$\theta_R$  - radiation temperature

The equation(3.15.3) assumes that there is negligible internal resistance to heat transfer. By integrating the above equation using approximate, linearized form that assumes Particle temperature changes slowly from one time step to the next.

$$m_p c_p \frac{dT_p}{dt} = A_p \{ -[h + \epsilon_p \sigma T_p^3] T_p + [h T_\infty + \epsilon_p \sigma \theta_R^4] \} \quad (3.15.4)$$

The equation is integrated once more to obtain the temperature at the next time step to give:

$$T_p(t + \Delta t) = \alpha_p + (T_p(t) - \alpha_p) \exp(-\beta \Delta t) \quad (3.15.5)$$

$\Delta$  is the integration time step

$$\alpha_p = \frac{h T_\infty + \epsilon_p \sigma \theta_R^4}{h + \epsilon_p \sigma T_p^3(t)} \quad (3.15.6)$$

and an expression for  $\beta$  can be written as:

$$\beta_p = \frac{A_p (h + \epsilon_p \sigma T_p^3(t))}{m_p c_p} \quad (3.15.7)$$

A relationship for the heat transfer coefficient  $h$ , is derived from Ranz <sup>(17)</sup>.

$$Nu = \frac{h D_p}{k_\infty} = 2.0 + 0.6 Re^{1/2} Pr^{1/2} \quad (3.15.8)$$

$D_p$  particle diameter

$k_\infty$  thermal conductivity of the phase

Re Reynolds number based on particle diameter and relative velocity

Pr Prandtl number of the continuous phase ( $c_p \mu / k_\infty$ ) The heat transfer by the parti-

cle appears as a source or sink term in the calculations of the continuous phase. When Laws 1 and 6 are applied the particles do not exchange mass with the continuous phase or cause any chemical reactions.

#### §3.15.2 Droplet Vaporization

This is referred to as Law 2 and is developed to predict the droplet vaporization from a discrete phase. This Law is applicable in situations where the temperature of the droplet reaches the vaporization temperature,  $T_{vap}$  and continues and eventually reaches the boiling point  $T_{bp}$ .

Law 2:

$$T_P < t_{bp} \quad (3.15.9)$$

$$m_p > (1 - f_{vo})m_{po} \quad (3.15.10)$$

#### §3.15.3 Mass Transfer During Vaporization

The rate at which the particle is vaporized is governed by the gradient diffusion, with the flux of droplet vapour into the gas phase

$$N_i t = k_c (C_{i,s} - C_{i,\infty}) \quad (3.15.11)$$

where:  $N_i t$  molar flux of vapour ( $\text{mol}/\text{m}^2 \text{-s}$ )

$k_c$  mass transfer coefficient ( $\text{m}/\text{s}$ )

$C_{i,s}$  vapour concentration at the droplet surface ( $\text{mol}/\text{m}^3$ )

$C_{i,\infty}$  vapour concentration in the bulk gas ( $\text{mol}/\text{m}^3$ )

The value of the  $N_{it}$  is positive, but should this value becomes Negative the droplet is treated as an inert particle. The vapour concentration at the droplet surface can be evaluated by assuming that the partial pressure of vapour at the interface is equal to the saturated vapour pressure,  $P_{sat}$ , at the particle droplet temperature,  $T_p$ :

$$C_{i,s} = \frac{P_{sat}(T_p)}{RT_p} \quad (3.15.12)$$

$R$  is the universal gas constant

The vapour concentration for the bulk gas can be determined from the following Relationship:

$$C_{i,\infty} = X_{it} \frac{P_{op}}{RT_{\infty}} \quad (3.15.13)$$

$X_{it}$  mole fraction of  $it$

$P_{op}$  is the operating pressure

$T_{\infty}$  is the local bulk temperature

The relationship proposed by Ranz<sup>(17)</sup>, Ranz1<sup>(18)</sup> calculates the mass transfer coefficient for the droplet, using the Nusselt number correlation as shown below:

$$Nu_{AB} = \frac{k_c D_p}{D_{i,m}} = 2.0 + 0.6 Re_D^{1/2} Sc^{1/3} \quad (3.15.14)$$

$D_{i,m}$  - diffusion coefficient of vapour in the bulk

$Sc$  - the Schmidt number,  $\frac{\mu}{\rho} D_{i,m}$

$D_p$  - particle (droplet) diameter (m)

The mass of the droplet is reduced according to:

$$m_p(t + \Delta t) = m_p(t) - N_{it} A_p M_{it} \Delta t \quad (3.15.15)$$

$M_{it}$  - molecular weight of species  $it$  (kg/mol)

$m_p$  - mass of droplet (kg)

$A_p$  - surface area of droplet ( $m^2$ )

### §3.15.4 Droplet Heat Transfer Equation

The temperature of the droplet is continuously updated according to the heat exchanges between the droplet and the continuous phase this process takes place in the form of convective and latent heat transfer.

$$m_p c_p \frac{dT_p}{dt} = h A_p (T_\infty - T_p) + \frac{dm_p}{dt} h_{fg} + A_p \epsilon_p \sigma (\theta_R^4 - T_p^4) \quad (3.15.16)$$

$c_p$  - droplet heat capacity (J/kg K)

$T - p$  - droplet temperature (K)

$h$  - convective heat transfer coefficient (W/m<sup>2</sup> K)

$T_\infty$  - temperature of continuous phase (K)

$\frac{dm_p}{dt}$  - rate of evaporation (kg/s)

$h_{fg}$  - latent heat (J/kg)

$\epsilon_p$  - particle emmissivity

$\sigma$  - Boltzmann temperature

$\theta_R$  - radiation temperature

In our study the radiation term was set to zero, so the heat transfer to or from The gas phase becomes a source or sink of energy during subsequent calculations of the continuous phase energy equation.

### §3.16 Droplet Boiling

This is referred to as Law 3 and is defined to predict the boiling behaviour of the droplet when it has reached the boiling temperature.

$$T_p \geq T_{bp} \quad (3.16.1)$$

$$m_p > (1 - f_{vo})m_{po} \quad (3.16.2)$$

Once the droplet has reached the boiling temperature the boiling rate equation Used generally for combustion is applied by Kuo <sup>(37)</sup>.

$$\frac{dD_p}{dt} = \frac{4k_{\infty}}{\rho_p c_{p,\infty} D_p} (1 + 0.23\sqrt{Re_D}) \ln\left[1 + \frac{c_{p,\infty}(T_{\infty} - T_p)}{h_{fg}}\right] \quad (3.16.3)$$

$c_{p,\infty}$  - heat capacity of the gas (J/kg-K)

$\rho_p$  - droplet density (kg/m<sup>3</sup>)

$k_{\infty}$  - thermal conductivity of the gas (W/m-K)

The equation(3.16.3) assumes steady flow at constant pressure and requires  $T_{\infty} > T_{bp}$  for the boiling to occur and the droplet to remain at the same Temperature.

## The Finite Volume Technique

*In this chapter the finite volume technique and the approach to linearization of the diffusive, convective and source terms has been described. The solution methods for the governing equations have also been discussed in detail. Furthermore, features specific to the unstructured grids and the locations where variables are stored are also discussed.*

### §4.1 Introduction

In the finite volume approach, the solution domain is subdivided into a finite number of small control volumes (CVs). The usual procedure is to define CVs by a suitable grid and assign the computational node to the CV centre. In the case of structured grids the nodal locations are defined and the CVs are constructed around them, so that CV faces lie midway between nodes. The advantage of this approach is that the nodal value represents the mean over the CV volume to higher accuracy. The conservation equations are (Ferziger <sup>(22)</sup>)

$$\frac{\partial}{\partial t} \int_{\Omega} \rho \phi d\Omega + \int_S \rho \phi v \cdot n dS = \int_S \Gamma \text{grad} \phi \cdot n dS + \int_{\Omega} q_{\phi} d\omega \quad (4.1.1)$$

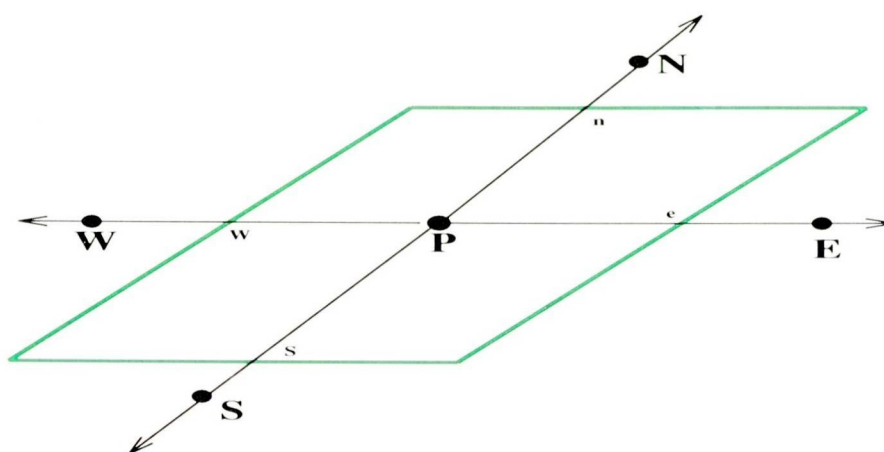


Figure 4.1.1: 2-D Control Volume

### §4.1.1 Convective Fluxes

In the analysis only the east side of the control volume shown in Figure(4.1.1) is used, for other directions the indices need to be changed. The application of midpoint approximation to the mass flux results in the following relationship:

$$\dot{m}_c = \int_{S_e} \rho v \cdot n dS \approx (\rho v \cdot n)_e S_e \quad (4.1.2)$$

The unit normal vector at the face "e" is defined by:

$$n_e S_e = S_e^i i = (y_{ne} - y_{se})i - (x_{ne} - x_{se})j \quad (4.1.3)$$

and the surface area  $S_e$  is given by:

$$S_e = \sqrt{(S_e^x)^2 + (S_e^y)^2} \quad (4.1.4)$$

A new mass flux definition can be derived from above:

$$\dot{m}_c = \rho_e (S^x u_x + S^y u_y)_e \quad (4.1.5)$$

In a Cartesian grid the, surface vector has components in more than one direction and all the velocity components contribute to the mass flux. Each Cartesian velocity

component is multiplied by the corresponding surface vector component as shown by equation(4.1.5). The convective flux of any transported quantity is usually calculated by assuming that the mass flux is known which, with the midpoint rule approximation gives equation(4.1.6):

$$F_e^c = \int_{S_e} \rho \phi v \cdot n ds \approx \dot{m}_e \phi_e \quad (4.1.6)$$

where  $\phi_e$  is the value of  $\phi$  at the centre of the cell face. The second order approximation is obtained by linear interpolation between the two nodes on either side of the face. The interpolation is usually performed by treating the piecewise linear lines as if they were straight; if the line changed direction at the cell face, an additional error is introduced. On structured non-orthogonal grids one can use higher order integration and interpolation techniques to approximate convective fluxes.

### §4.1.2 Diffusion Fluxes

Application of the midpoint rule to the integrated fluxes gives:

$$F_e^d = \int_{S_e} \Gamma \text{grad} \phi \cdot n dS \approx (\Gamma \text{grad} \phi \cdot n)_e S_e \quad (4.1.7)$$

at this point an expression for the gradient of the variable  $\phi$  at the cell face centre can be written in terms of the derivatives with respect to global Cartesian coordinates or local coordinates (n,t). For a 2-D example we obtain:

$$\text{grad} \phi = \frac{\partial \phi}{\partial x} i + \frac{\partial \phi}{\partial y} j = \frac{\partial \phi}{\partial n} n + \frac{\partial \phi}{\partial t} t \quad (4.1.8)$$

where n and t represent the coordinate directions normal and tangential to the surface respectively. The expression for the implicit part of the method can be written if the local (n,t,s) orthogonal coordinate system is attached to the cell face centre. This

means that only the derivative in the n-direction contributes to the diffusive flux:

$$F_e^d = \Gamma_e \left( \frac{\partial \phi}{\partial n} \right)_e S_e \quad (4.1.9)$$

In a Cartesian grid,  $n=x$  at the face "e" and applying the central difference approximation:

$$\left( \frac{\partial \phi}{\partial n} \right)_e \approx \frac{\phi_E - \phi_P}{L_{P,E}} \quad (4.1.10)$$

$L_{P,E}$  is the distance between E and P on a uniform Cartesian grid. The interpolated cell centre gradient gives:

$$\overline{\left( \frac{\partial \phi}{\partial n} \right)_e} = \frac{1}{2} \frac{\phi_E - \phi_W}{2\Delta x} + \frac{1}{2} \frac{\phi_{EE} - \phi_P}{2\Delta x} \quad (4.1.11)$$

There is an oscillation of the variable  $\phi$  present in the x- direction, as shown in Figure(4.1.2). The oscillation will not contribute to this gradient, since both  $\phi_E - \phi_W$  and  $\phi_{EE} - \phi_P$  are zero and so are the gradients at each cell centre. The oscillation can be eliminated by using an implicit flux approximation given by equation(4.1.12)

$$F_e^d = \Gamma_e S_e \left( \frac{\partial \phi}{\partial \xi} \right)_e = \Gamma_e S_e \frac{\phi_E - \phi_P}{L_{P,E}} \quad (4.1.12)$$

The line connecting nodes P and E to the cell face determine the accuracy of the approximation. For example if the line is orthogonal to the cell face the accuracy is second order and the deferred correction term is zero. However if the grid is non-orthogonal, the deferred correction term must contain the difference between the gradients in  $\xi$  and n directions.

$$F_e^d = \Gamma_e S_e \left( \frac{\partial \phi}{\partial \xi} \right)_e + \Gamma_e S_e \left[ \overline{\left( \frac{\partial \phi}{\partial n} \right)_e} - \overline{\left( \frac{\partial \phi}{\partial \xi} \right)_e} \right]^{old} \quad (4.1.13)$$

The first term on the right hand side is treated implicitly while the second term is the deferred correction. The deferred correction term can be calculated using interpolated cell centre gradients in n and  $\xi$  directions.  $\overline{\left( \frac{\partial \phi}{\partial n} \right)_e} = \overline{(grad\phi)_e} \cdot n$

$$\overline{\left( \frac{\partial \phi}{\partial \xi} \right)_e} = \overline{(grad\phi)_e} \cdot i \xi$$

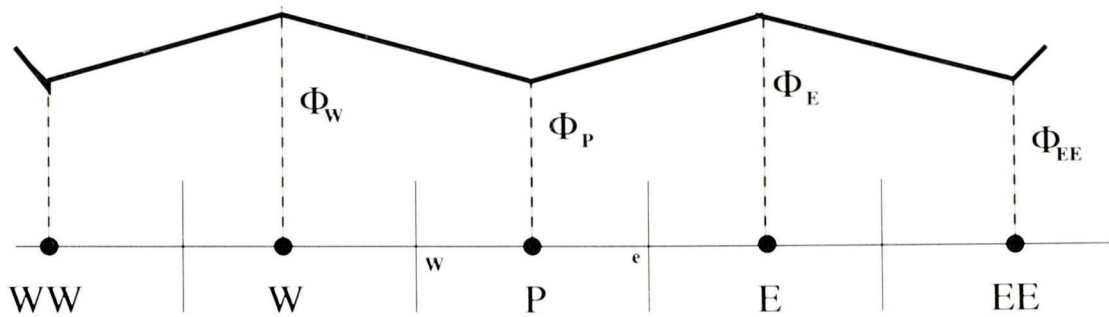


Figure 4.1.2: Approximation of gradients at cell faces Source:Ferziger 1999

$i$   $\xi$  is the unit vector in the  $\xi$ -direction. This allows the final approximation to the diffusive flux through the cell face "e" can be written

$$F_e^d = \Gamma_e S_e \frac{\phi_E - \phi_P}{L_{P,E}} + \Gamma_e S_e \overline{(\text{grad}\phi)_e}^{old} \cdot (n - \xi) \quad (4.1.14)$$

### §4.1.3 Source term approximation

The midpoint rule approximates a volume integral by the product of the CV centre value of the integrand and the CV volume.

$$Q_p^\phi = \int_{\Omega} q_\phi d\Omega \approx q_{\phi,P} \Delta\Omega \quad (4.1.15)$$

The approximation is independent of the CV shape and is approximately second order accurate.

$$Q_p^P = - \int_{\Omega} \frac{\partial P}{\partial x} d\Omega \approx - \left( \frac{\partial P}{\partial x} \right)_P \Delta\Omega \quad (4.1.16)$$

The derivative  $\frac{\partial P}{\partial x}$  is calculated using the Gauss theorem. If the pressure gradient with respect to  $x$  is transferred into gradients with respect to  $\xi$  and  $\eta$  for local

coordinate system at the CV center then

$$Q_P^p \approx -(P_e - P_w)(y_n - y_s) + (P_n - P_s)(y_e - y_w) \quad (4.1.17)$$

### §4.2 Segregated Solution Method

As the name suggests using the segregated solution technique, the equations are solved segregated from each other. The nature of the governing equations dictates that, several iterations of the solution loop must be performed before a converged solution is reached. The iteration procedure consists of the following procedure:

- 1) Initialise all variables
- 2) Fluid properties are updated using the current solution. The updated value at the beginning of the process is based on the initialised solution.
- 3) The u, v and w momentum equations are each solved in turn using current values for pressure and face mass fluxes, in order to update the velocity field.
- 4) The velocities obtained at the first stage, generally do not satisfy the continuity equation locally, hence a Poisson Type equation for pressure correction is derived from the continuity equation and the linearized momentum equations. This pressure correction equation, allows the adjustments to pressure and the velocity fields be made so that local continuity is satisfied.
- The variable equations for quantities such as turbulence and species are solved using the previously updated values.
- 5) In situations where inter phase coupling is to be included, the source terms in the appropriate continuous phase equations may be updated with a discrete phase trajectory calculation.
- 6) A check for convergence is preformed.

- 7) The process is repeated until a defined convergence criteria is reached.

#### §4.3 Approximation of Surface Integrals

The Cartesian control volume (CV) is shown in Figure(4.1.1). The CV surface is subdivided into four plane faces the 2D, each face is given a lower case letter to denote its direction (e, w, n, s) with respect to the central node (P). The net flux through the CV boundary is the sum of integrals over the four faces:

$$\int_S f dS = \sum_k \int_{S_k} f dS \quad (4.3.1)$$

Where  $f$  is the component of the convective ( $\rho\phi \cdot \mathbf{v} \cdot \mathbf{n}$ ) or diffusive ( $\Gamma \text{grad}\phi \cdot \mathbf{n}$ ) vector in the direction normal to CV face. it is important that CVs do not overlap, so that conservation can be maintained, each CV face is unique to the two CVs which lie on either side of it. Once again to exemplify the process, the e face is considered in what follows. The surface integral in Equation(4.3.1) can only be evaluated if the value of the integral  $f$  everywhere on the surface  $s_e$  is known. However this value is only known at the nodal point at the centre of the CV, so an approximation is used as follows:

$$F_e = \int_{S_e} f dS = \bar{f}_e S_e \approx f_e S_e \quad (4.3.2)$$

The values of  $f$  are not available at the cell faces, therefore an interpolation scheme is used to obtain this value. The interpolation scheme needs to be second order accurate.

#### §4.4 The Implicit Method

The term implicit is a reference to the way in which the governing equations are linearized. The way this system works is that for any given variable, the unknown

value is calculated in each cell, involving a technique which uses the existing value and the unknown value from neighbouring cells. The result of such a technique is that each of the unknowns would appear in more than one equation, hence allowing the equations to be solved simultaneously, to give the value of the unknowns. The fully implicit method is recommended for general purpose CFD simulations, due to its stability. If we consider the generic transport equation in 1-D form and applying the implicit Euler method, we get:

$$\frac{\partial \phi}{\partial t} = -u \frac{\partial \phi}{\partial x} + \frac{\Gamma}{\rho} \frac{\partial^2 \phi}{\partial x^2} \quad (4.4.1)$$

$$\phi_i^{n+1} = \phi_i^n + \left[ -u \frac{\phi_{i+1}^{n+1} - \phi_{i-1}^{n+1}}{2\Delta x} + \frac{\Gamma}{\rho} \frac{\phi_{i+1}^{n+1} + \phi_{i-1}^{n+1} - 2\phi_i^{n+1}}{(\Delta x)^2} \right] \Delta t \quad (4.4.2)$$

Hence all the fluxes and source terms of the unknown variable values at the new time level are evaluated.

The result is a system of algebraic equations very similar to the one obtained for steady problems. The difference is in an additional contribution to the coefficient  $A_p$  and to the source term  $Q_p$ , which stems from the unsteady term. The Equation(4.4.2) may be written as:

$$A_p \phi_i^{n+1} = A_E \phi_{i+1}^{n+1} + A_W \phi_{i-1}^{n+1} \quad (4.4.3)$$

where:

$$A_E = \frac{\rho u}{2\Delta x} - \frac{\Gamma}{(\Delta x)^2}$$

$$A_W = \frac{-\rho u}{2\Delta x} - \frac{\Gamma}{(\Delta x)^2}$$

$$A_p = -(A_E + A_W) + \frac{\rho}{\Delta t} Q_p = \frac{\rho}{\Delta t} \phi_i^n$$

In this case the use of the implicit method allows arbitrary large time steps to be

---

taken, however on the negative side, first order truncation errors are introduced, but the overall picture tends to favour the scheme. In the iteration at the new time step, the best initial guess is the converged solution at the preceding time step. If the final steady state is the only result of interest and details of the development from the initial guess to the final stage are not of importance, it might be sufficient to carry out one iteration per time step. The disadvantage of one iteration per time step is that the scheme may not be very stable, however, it would be faster.

### §4.5 Pressure Calculation

The momentum equations determine the respective velocity components so their values are defined. The continuity equation can be used to simplify the resulting equation, leaving a Poisson equation for the pressure. This equation can be written in cartesian coordinate form as:

$$\frac{\partial}{\partial x_i} \left( \frac{\partial P}{\partial x_i} \right) = - \frac{\partial}{\partial x_i} \left[ \frac{\partial}{\partial x_j} (\rho U_i U_j - \tau_{ij}) \right] + \frac{\partial(\rho b_i)}{\partial x_i} + \frac{\partial^2 \rho}{\partial t^2} \quad (4.5.1)$$

In situations where the density and viscosity are constant, the above equation reduces to Equation(4.5.2) shown below:

$$\frac{\partial}{\partial x_i} \left( \frac{\partial P}{\partial x_i} \right) = - \frac{\partial}{\partial x_i} \left[ \frac{\partial(\rho U_i U_j)}{\partial x_j} \right] \quad (4.5.2)$$

In the pressure equation the term on the right hand side is the sum of the derivatives of terms in the momentum equations.

### §4.5.1 Implicit Time Advance Method

### §4.5.2 Introduction

In this section a method for the unsteady equations that illustrates how the numerical Poisson equation for the pressure is constructed and the role it plays in enforcing continuity. The semi-discretized momentum equations can be written as:

$$\frac{\partial(\rho U_i)}{\partial t} = -\frac{\partial(\rho U_i U_j)}{\partial x_j} - \frac{\partial P}{\partial x_i} + \frac{\partial \tau_{ij}}{\partial x_j} = H_i - \frac{\partial P}{\partial x_i} \quad (4.5.3)$$

The term  $\frac{\partial}{\partial x}$  represents a discretized spatial derivatives and  $H_i$  is the shorthand notation for the advective and viscous terms. For simplicity the Equation(4.5.3) can be solved with Explicit Euler method for time advancement. In this case the Equation(4.5.3) reduces to:

$$(\rho u_i)^{n+1} - (\rho u_i^n) = \Delta t(H_i^n - \frac{\partial p^n}{\partial x_i}) \quad (4.5.4)$$

The velocity at time step n is used to compute  $H_i^n$  and if the pressure field value is available,  $\frac{\partial p^n}{\partial x_i}$  may also be computed. This gives an estimate of  $\rho u_i$  at the new time step n + 1. However in general this velocity field does not satisfy the continuity equation:

$$\frac{\partial(\rho u_i)^{n+1}}{\partial x_i} = 0 \quad (4.5.5)$$

$$(\rho U_i)^{n+1} - (\rho U_i)^n = \Delta t\left(\frac{\partial(\rho U_i U_j^{n+1})}{\partial x_j} - \frac{\partial P^{n+1}}{\partial x_i} + \frac{\partial \tau_{ij}^{n+1}}{\partial x_j}\right) \quad (4.5.6)$$

The divergence of the velocity field at the new time step must be zero. The second term would be zero if continuity has been reached at time step n; in the equation.

This term must be retained, when an iterative process is used to solve the Poisson equation for the pressure and the iterative process is not converged. In a similar manner the divergence of the viscous component of  $H_i$  should be zero for constant  $\rho$ .

$$\frac{\partial}{\partial x_i} \left( \frac{\partial P^{n+1}}{\partial x_i} \right) = \frac{\partial}{\partial x_i} \left( \frac{\partial (\rho U_i U_j)^{n+1}}{\partial x_j} \right) \quad (4.5.7)$$

In this situation the term on the right hand side of Equation(4.5.7) can not be computed until the computation of the velocity field at the time  $n+1$  is completed and vice versa. This means that the momentum and the Poisson equations need to be solved simultaneously.

Equation(4.5.7) needs to be solved using the converged result from the preceding time step as the initial guess for the new velocity field and then converged to the solution at the new time step. The alternative way to deal with the non-linearity is by linearizing the equations at the preceding time step as follows:

$$U_i^{n+1} = U_i^n + \Delta U_i \quad (4.5.8)$$

The nonlinear term in the Equation(4.5.6) can be written as:

$$U_i^{n+1} U_j^{n+1} = U_i^n U_j^n + U_i^n \Delta U_j + U_j^n \Delta U_i + \Delta U_i \Delta U_j \quad (4.5.9)$$

In cases when  $\Delta t$  is small,  $\Delta U_i \approx \Delta t \partial U_i / \Delta t$ .

The last term in Equation(4.5.9) is second order in  $\Delta t$  and is generally neglected due to its small magnitude. The result would be to re write the Equation(4.5.6) in the following format:

$$\begin{aligned} \rho \Delta u_i = & \delta \left( \frac{\partial (\rho u_i U_j)^n}{\partial x_j} + \frac{\partial (U_i^n \Delta U_j)}{\partial x_j} + \frac{\partial (\rho \Delta U_i U_j^n)}{\partial x_j} \right. \\ & \left. - \frac{\partial P^n}{\partial x_i} - \frac{\partial \Delta P}{\partial x_i} + \frac{\partial \tau_{ij}^n}{\partial x_j} + \frac{\partial \Delta \tau_{ij}}{\partial x_j} \right) \end{aligned} \quad (4.5.10)$$

The system of equations is still large to solve, hence an alternative method is to split

---

the equations into a series of 1-D equations, so that the solution at each time step can be sought for with just one iteration. This method is generally known as the alternating direction implicit (ADI) method. The ADI approach is used to update the equations by using the old pressure gradient. The velocity field needs to be corrected using the following scheme:

- the velocity field is computed by updating the momentum equation using the old pressure gradient  $u_i^*$
- solve the Poisson equation for the pressure correction

$$\frac{\partial}{\partial x_i} \left( \frac{\partial \Delta P}{\partial x_i} \right) = \frac{\partial(\rho u_i^*)}{\partial x_i} \quad (4.5.11)$$

- the velocity value is updated

$$U_i^{n+1} = U_i^* - \frac{\partial \Delta P}{\partial x_i} \quad (4.5.12)$$

The above equation satisfies continuity. The procedures described so far produce an accurate solution for unsteady problems. However the accuracy of the solution is dependent on the size of the time step. The implicit method allows larger time steps to be used without introducing any instability.

### §4.5.3 Implicit Pressure-Correction methods

The reason that Implicit methods are chosen for steady state and transient flow situations is that they offer a greater facility in terms of selecting the time step size.

When the implicit method is used to advance the momentum equations in time, the discretized equations for the velocities at the new time step are non linear. If the

pressure gradient term is omitted from the source term, the equation may be written as:

$$A_P^{U_i} U_{i,P}^{n+1} + \sum_l A_l^{U_i} U_{i,l}^{n+1} = Q_{u_i}^{n+1} - \left( \frac{\partial P^{n+1}}{\partial x_i} \right)_P \quad (4.5.13)$$

- P- is the index of the velocity node
- l- denotes the neighbour points which appear in the discretized momentum equation
- Q- all the terms which may be calculated explicitly in terms of  $U_i^n$  as well as any body force or other linearized terms that may depend on the  $U_i^{n+1}$  or other variables at the new time level, e.g, body forces or other variables at the new time step. The pressure term is written in symbolic difference form to emphasize the independence of the solution method from the discretization approximation for the spatial derivatives.

The Equation(4.5.13) can not be solved directly as the coefficients A and possibly the source term depend on the unknown solution  $U_i^{n+1}$ . In an unsteady flow situation the iteration within each time step needs to be carried out until entire system of non-linear equation is satisfied to within a narrow tolerance.

The iteration process which updates the coefficients and source term matrices is called the outer iteration. The following equation is solved during each outer iteration:

$$A_p^{u_i} U_{i,P}^{m*} + \sum_l A_l^{U_i} U_{i,l}^{m*} = Q_{U_i}^{m-1} - \left( \frac{\partial P^{m-1}}{\partial x_i} \right)_P \quad (4.5.14)$$

The time step index  $n + 1$  has been dropped and an outer iteration counter  $m$ ;  $U_i^m$ , thus represents the current estimate of the solution  $U_i^{n+1}$ . At the beginning of each outer iteration, the terms on the right hand side of Equation(4.5.13) are solved using the variables at the preceding outer iteration.

The momentum equations are solved as a set of algebraic equations for each com-

---

ponent of the momentum, but as the pressure used in these iterations is from the previous time step, the velocities computed, do not satisfy the discretized continuity equation. In order to satisfy the continuity equation, which implies the pressure field needs to be modified. The velocity at node P, obtained by solving the linearized momentum equations can be expressed as:

$$U_{i,P}^{m*} = \frac{Q_{U_i}^{m-1} - \sum_l A_l^{U_i} U_{i,l}^{m*}}{A_P^{u_i}} - \frac{1}{A_P^{u_i}} \left( \frac{\partial P^{m-1}}{\partial x_i} \right)_P \quad (4.5.15)$$

The variable  $U_{i,P}^{m*}$  is the predicted value, for the iteration m. The first term on the right hand side can be substituted by  $\tilde{U}_{i,P}^{m*}$ . This procedure in effect removes the contribution of pressure gradient. The corrected velocity and pressure field are linked together by the following equation:

$$U_{i,P}^m = \tilde{U}_{i,P}^{m*} - \frac{1}{A_P^{u_i}} \left( \frac{\partial P^m}{\partial x_i} \right)_P \quad (4.5.16)$$

Continuity can be enforced by inserting the expression for  $U_i^m$  into the continuity equation, to obtain a discrete Poisson equation for pressure:

$$\frac{\partial}{\partial x_i} \left[ \frac{\rho}{A_P^{u_i}} \left( \frac{\partial P^m}{\partial x_i} \right) \right]_P = \left[ \frac{\partial \rho \tilde{U}_i^{m*}}{\partial x_i} \right]_P \quad (4.5.17)$$

The solution of Poisson equation (4.5.17) for the pressure, provides a solution for the velocity at the new iteration  $U_i^m$ , which satisfies the continuity equation.

#### §4.6 Quadratic Upwind Interpolation Scheme: QUICK

The quadratic upstream interpolation for convective kinetics (QUICK) scheme of Leonard <sup>(41)</sup> uses a three-point upstream-weighted quadratic interpolation for cell face values. This interpolation scheme was used in the studies carried out, as it gives accurate results on coarse meshes. The face value of  $\phi$  is obtained from a quadratic function passing through two nodes (on each side of the face) and a node on the upstream side. This is best illustrated in the Figure (4.1.2). For example, when  $U_w$

$> 0$  and  $U_e > 0$  a quadratic fit through WW, W and P is used to evaluate  $\phi_w$ , and a further quadratic fit through W, P and E to calculate  $\phi_e$ . The value of  $\phi$  at the cell face between two bracketing nodes  $i$ , and  $i-1$ , and upstream node  $i-2$  is given by the following Equation(4.6.1).

$$\phi_{face} = \frac{6}{8}\phi_{i-1} + \frac{3}{8}\phi_i - \frac{1}{8}\phi_{i-2} \quad (4.6.1)$$

In the situation where  $u_w > 0$  the nodes for the west face  $w$  are W and P, the upstream node being WW.

$$\phi_w = \frac{6}{8}\phi_W + \frac{3}{8}\phi_P - \frac{1}{8}\phi_{WW} \quad (4.6.2)$$

In the case where  $u_e > 0$ , the nodes for the east face  $e$  are P and E, the upstream node is W.

$$\phi_e = \frac{6}{8}\phi_P + \frac{3}{8}\phi_E - \frac{1}{8}\phi_W \quad (4.6.3)$$

The diffusion term is evaluated using gradient of the appropriate parabola. Using Equations (4.6.2 and 4.6.3) for the convective terms and central differencing for the diffusion terms, the discretised form of the one-dimensional convection-diffusion transport equation may be written as:

$$\begin{aligned} [D_w - \frac{3}{8}F_w + D_e + \frac{6}{8}F_e]\phi_P &= [D_w + \frac{6}{8}F_w + \frac{1}{8}F_e]\phi_W \\ &+ [D_e - \frac{3}{8}F_e]\phi_E - \frac{1}{8}F_w\phi_{WW} \end{aligned} \quad (4.6.4)$$

The discretised form can be written as:

$$a_P\phi_P = a_W\phi_W + a_E\phi_E + a_{WW}\phi_{WW} \quad (4.6.5)$$

$a_W$	$a_E$	$a_{WW}$	$a_P$
$D_w + \frac{6}{8}F_w + \frac{1}{8}F_e$	$D_e - \frac{3}{8}F_e$	$-\frac{1}{8}F_w$	$a_W + a_E + a_{WW} + (F_e - F_w)$

Table (4.6.1) Discretised form of the QUICK scheme

#### §4.6.0.1 Remarks on the QUICK scheme

The QUICK scheme uses a quadratic interpolation profile to calculate the cell face values between two nodes and the upstream node. The transportiveness property is built into the scheme as the quadratic function is based on two upstream and one downstream nodal values. If the flow field satisfies continuity the coefficient  $a_p$  equals the sum of all neighbour coefficients which is desirable for boundedness.

The disadvantage of the system is that, the main coefficients (E and W) are not guaranteed to be positive and the coefficients  $a_{WW}$  and  $a_{EE}$  are negative.

### §4.7 Unstructured Grids

The use of unstructured grids has meant that control volumes of arbitrary shapes with any number of cell faces can be used. This is of particular advantage when trying to match the grid to domain boundaries.

The way data is formulated depends on the type of CV used. Whenever a grid is generated a list of vertices is generated. Each CV is defined by four or eight vertices, so the list of CVs contains a list of associated vertices. The order of vertices in the list represents the relative positions of the cell faces.

§4.7.1 Underrelaxation Criterion

It is often desirable to speed up or slow down the changes from one iteration to the next. Under-relaxation is a very useful device for providing this flexibility. When relaxation values are within the range 0 to 1, the effect is under-relaxation, Patankar (67). There are no general rules for choosing the best value of under-relaxation. The optimum value depends upon a number of factors, such as the nature of the problem, the number of grid points, grid spacing and the iterative procedure used. The best values are generally determined from experience. In mathematical form it can be shown to be as follow if we start with the algebraic equation for a generic variable  $\phi$  at a typical point P:

$$A_p \phi_p^n + \sum_l A_l \phi_l^n = Q_p \tag{4.7.1}$$

Q represents all the terms that do not depend explicitly on  $\phi^n$

the coefficients  $A_l$  and the source Q may involve  $\phi^{n-1}$

The value of  $\phi^n$  is allowed to change only by a fraction  $\alpha_\phi$ , so that a relationship can be established.

$$\phi^n = \phi^{n-1} + \alpha_\phi (\phi^{new} - \phi^{n-1}) \tag{4.7.2}$$

The new solution can replace the old iteration by the following relationship:

$$\underbrace{\frac{A_p}{\alpha_\phi} \phi_p^n + \sum_l A_l \phi_l^n}_{\text{left side}} = \underbrace{Q_p + \frac{1 - \alpha_\phi}{\alpha_\phi} A_p \phi_p^{n-1}}_{\text{right side}} \phi_p^{new} = \frac{Q_p - \sum_l A_l \phi_l^n}{A_p} \tag{4.7.3}$$

hence a modified equation for the node P can be written:

$$\underbrace{\frac{A_p}{\alpha_\phi} \phi_p^n + \sum_l A_l \phi_l^n}_{\text{left side}} = \underbrace{Q_p + \frac{1 - \alpha_\phi}{\alpha_\phi} A_p \phi_p^{n-1}}_{\text{right side}} \tag{4.7.4}$$

If we let the term on the right hand side of the equation identified by an underbrace be  $A_p^*$  and the term on the left  $Q_p^*$ , these two terms would represent the modified diagonal matrix elements and source vector components. This modified equation is

solved within inner iterations. When the outer iterations converge, the terms involving  $\alpha_\phi$  cancel out and the solution to the original problem is obtained. This type of underrelaxation has a positive effect, since the diagonal dominance of matrix A is increased, hence it is more efficient than explicit application of the Equation(4.7.3)

### §4.7.2 Convergence Criterion

In an iterative procedure it is important to realize when the iteration process can be terminated. The most common procedure adopted is to take the difference between two successive iterations to be less than a pre-selected value.

- i) Start with an estimated value for variable at the grid points.
- ii) From the guessed value of the variable values of the coefficients in the discretisation equation are calculated.
- iii) The linear set of algebraic equations are solved to obtain a new value for the variable.
- iv) with the new value of the variable as a more accurate approximation, steps ii and iii are repeated until the new values obtained do not differ significantly from the previous values.
- The convergence criteria for the residuals is set typically to a value of  $10^{-6}$ . Once the values of the variables being calculated reach this pre selected value the iteration is terminated.

## §4.8 Staggered Grid

In the finite volume technique, the initial stage starts with the discretisation of the transport equation. The problem to consider is the location at which the variables,

---



§4.9 Momentum Equations Variables

It can be seen from Figure(4.9.1) [Versteeg <sup>(68)</sup>] that the U-velocities are stored at the e and w cell faces of a scalar control volume. These are located at the intersection of a line defining a cell boundary and a grid line and are represented by a combination of lower case letter and a capital letter. The type of grid represented in Figure(4.8.1) is classed as a backward staggered grid, since the i- direction for the U-velocity  $U_{i,J}$  is at a distance of  $\frac{-1}{2\partial x_U}$  from the scalar node (I,J). This new coordinate system allows the discretised U-momentum equations at location(i,J) can be written as:

$$a_{i,J}U_{i,J} = \sum a_{nb}U_{nb} - \frac{P_{I,J} - P_{I-1,J}}{\partial x_U} \Delta V_U + \bar{S} \Delta V_U \quad (4.9.1)$$

where:  $\Delta V_U$  is the volume of the U-cell

$b_{i,j} = \bar{S} \Delta V_U$  is the momentum source term

$i,J$  is the east or west cell face area of the U-control volume.

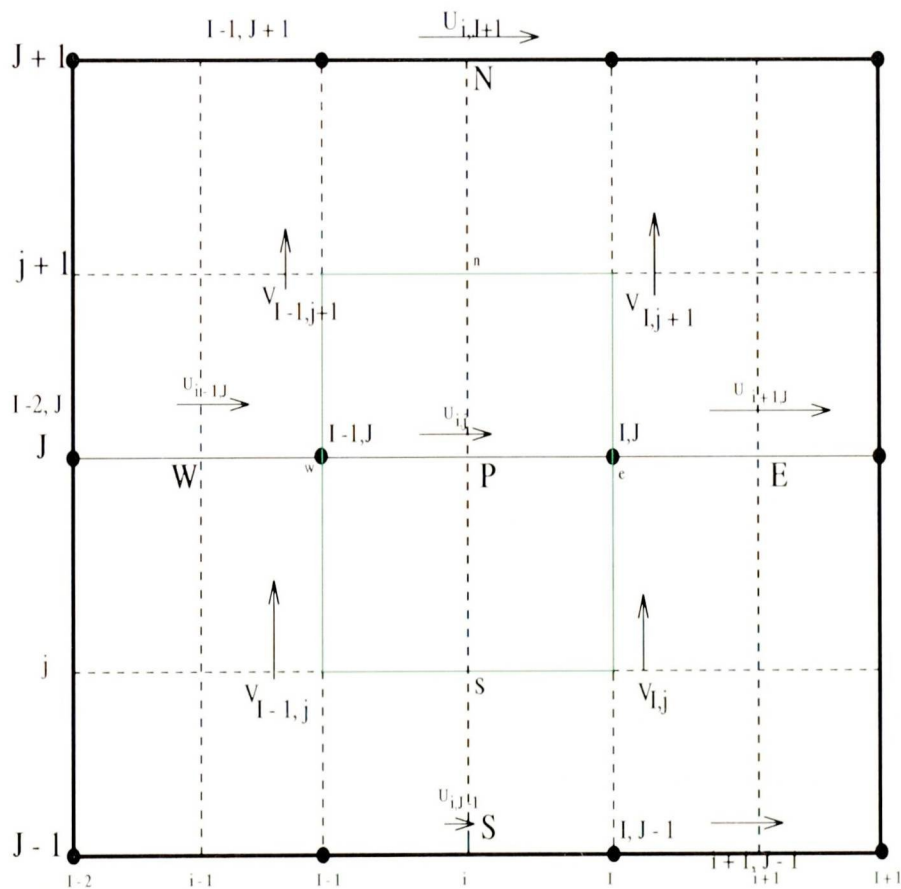


Figure 4.9.1: V-control volume and its neighbouring velocities

Source: Versteeg and Malalasekera, 1995

## Experimental Technique

*In addition to the numerical study an experimental programme was carried out in collaboration with Brighton and Loughborough universities. The experimental study consisted of flow visualization and Laser Doppler Anemometry(LDA). The methods employed are described in detail in this chapter. The objectives of the experimental programme were, a) to provide a better understanding of the flow, and b) to validate the numerical model. In this chapter an introduction into Laser Doppler Anemometry(LDA) and detailed experimental procedure and equipment used is given.*

### §5.1 Introduction

The complexity of fluid motion, and associated difficulties in obtaining accurate theoretical solutions, has meant that, fluid dynamicists have had to rely on experimental techniques to validate their results. It is therefore important to know how the instruments used in flow measurements record the various fluid dynamic parameters. This understanding becomes particularly important where the flow is turbulent in nature. There are various experimental techniques available, but for our studies only laser Doppler anemometry and flow visualization techniques have been used.

Laser Doppler Anemometry(LDA) is an optical instrument that can be applied to the measurement of the velocity and velocity fluctuation in fluid flows. For such

measurements, the flow must be seeded, either by naturally occurring particles (e.g. air bubbles) or through artificially introducing fine particles that are chosen to follow the mean flow and frequency of fluctuation adequately. LDA utilises Laser light beams to measure a velocity component of the flow particles at a single point in the flow as a sequence of near instantaneous samples. The LDA technique is non-intrusive to the flow, has a high spatial and temporal resolution and requires no calibration. The output signal is a linear function that is proportional to the velocity. With suitable frequency shifting techniques, directional ambiguity in the flow pattern can be removed. As such, it is particularly suited to the measurement of unsteady and turbulent flows.

### §5.2 Laser Systems

The invention and introduction of laser techniques has made it possible to make point measurements in experimental fluid dynamics. The first laser Doppler technique was introduced by Yeh <sup>(72)</sup>, Since then there have been many advances both in signal processing and optical methods. There are several advantages in using laser techniques compared to other experimental velocity measurement techniques. These are:

- the measurement technique is non-invasive, hence the flow field is not disturbed
- no calibration is required
- the instrument measures velocity in a specified direction, the output being a linear function of this velocity component
- the method can be used in turbulent flows, or for velocities ranging from a few millimetres per second to supersonic flows
- velocity measurements can be made in three directions simultaneously

#### §5.3 Laser Doppler Velocimetry Configuration

The first type of LDV system of Yeh <sup>(72)</sup> was of the heterodyne type. The way this system operates is simply directing the laser beam into the path of fluid. The scattered light is then observed by the photodetector at an angle to the original direction of the propagation of the beam. It can be assumed from the Doppler shift equation, that the frequency of the scattered light is proportional to the flow velocity, but in most practical situations the frequency shift is going to be extremely small compared with the optical frequencies involved. The shift in frequency can be observed if the scattered light is mixed with light from the laser which is unshifted in frequency. The photodetector signal then contains a beat frequency equal to the Doppler shift frequency proportional to the flow velocity. The schematic arrangement is shown in Figure(5.3.1). The laser beam is split into two beams and the beams are focused into the flow region known as the control volume. The photodetector is aligned with the reference beam on the other side of the flow. In the standard laser setups the region where the scattered light is collected from can be adjusted, by placing two apertures in front of the detector.

The frequency of the LDV system is given by the following equation:

$$f_0 = \frac{2U \sin\theta n_f}{\lambda} \quad (5.3.1)$$

- $U$  is the magnitude of velocity
- $\lambda$  wavelength of the illuminating laser
- $f_0$  Doppler frequency of the system
- $n_f$  refractive index of the flow medium

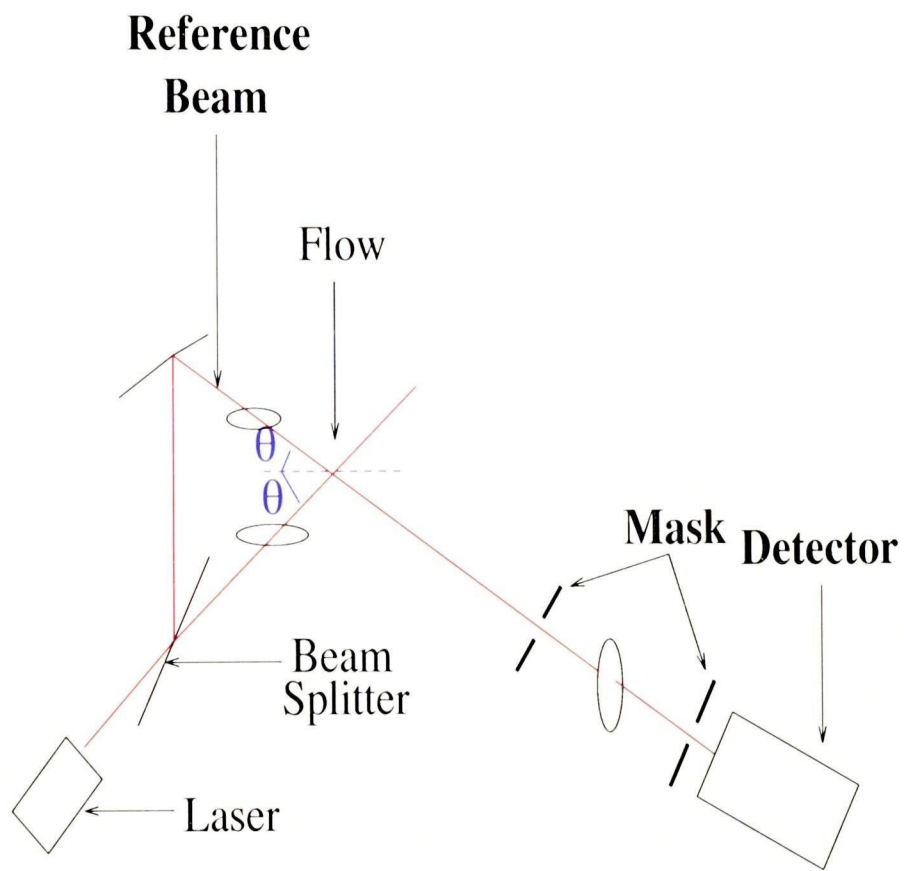


Figure 5.3.1: Schematic representation of LDV System

The system described is a basic unit consisting of three major components,

- The illuminating
- The reference and
- The collection units

In order to obtain good signal to noise ratio the three components have to be kept aligned. This is achieved by mounting the whole system on an optical table. The other region which requires careful consideration is the flow region. In this region we need to obtain the relevant information. In the flow regions the beams do not need to go through the region, instead a device is used causing the beams to split and be directed around the flow forming a control volume. The original system used by Yeh <sup>(72)</sup>, Angus <sup>(1)</sup>, Rizzo <sup>(57)</sup>, was of this type.

This generally overcome by using a lens, which is placed in the path of the beams. The function of the lens is to focus the incident and the reference beams. The set up is shown diagrammatically in Figure(5.3.2) as proposed by Bedi <sup>(4)</sup>. The beam splitter is placed in the path of the emerging beam from the laser. The beam can then travel straight through to the detector. The advantage of this set up is that alignment is made easy for measuring fluid flow in circular ducts and also it allows the flexibility to rotate the measuring direction without the observation volume being moved. The emitted rays are not generally of the same length, This would result in a reduction of the signal. In order to compensate for this shortfall a path length compensator which is generally a block of glass is placed in the path of the reference beam in the region from the beam splitter to the observation volume. The disadvantage of this optical configuration is that the actual flow velocity is not measured, but instead the velocity component in a direction perpendicular to bisector of the angle between the reference and the illuminating beams is measured. The error introduced is generally very small due to the fact that the angle between the two beams is small.

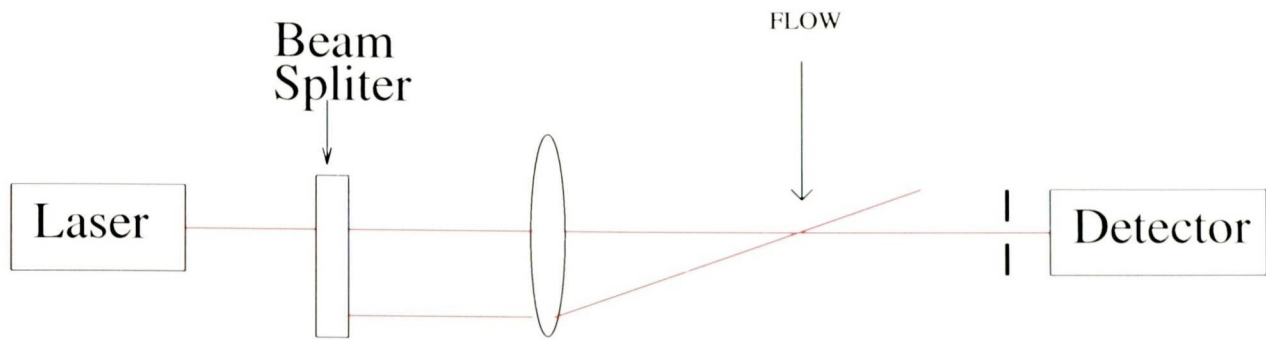


Figure 5.3.2: Schematic representation of single lens LDV System

### §5.4 Real Fringe Systems

It was the research carried out by Rudd <sup>(60)</sup> who realized that, by focusing two parallel beams in the flow, resulted in creating the Young's interference fringes. The arrangement is shown in Figure(5.4.1). The laser beam is diverged and collimated to produce a parallel beam of a few centimetres, which passes through a mask with two parallel slits. The resulting beams are refocused to form two interference patterns in the flow region and the beams emerging through the flow are brought to focus in the photo detector. This simple arrangement allows the exact nature of the Doppler signal to be calculated. The light intensity in the focal plane is given by:

$$I(x, y) = \frac{\sin^2(k_1 x)}{(k_1 x)^2} \frac{\sin^2(K_2 y)}{(K_2 y)^2} \cos^2(bK_1 x/a) \quad (5.4.1)$$

where

a aperture width

c depth of aperture

b distance between fringes

$K_1 \pi a n_f / (\lambda L)$

$K_2 \pi c n_f$

$\lambda$  wave length

L focal length of the lens

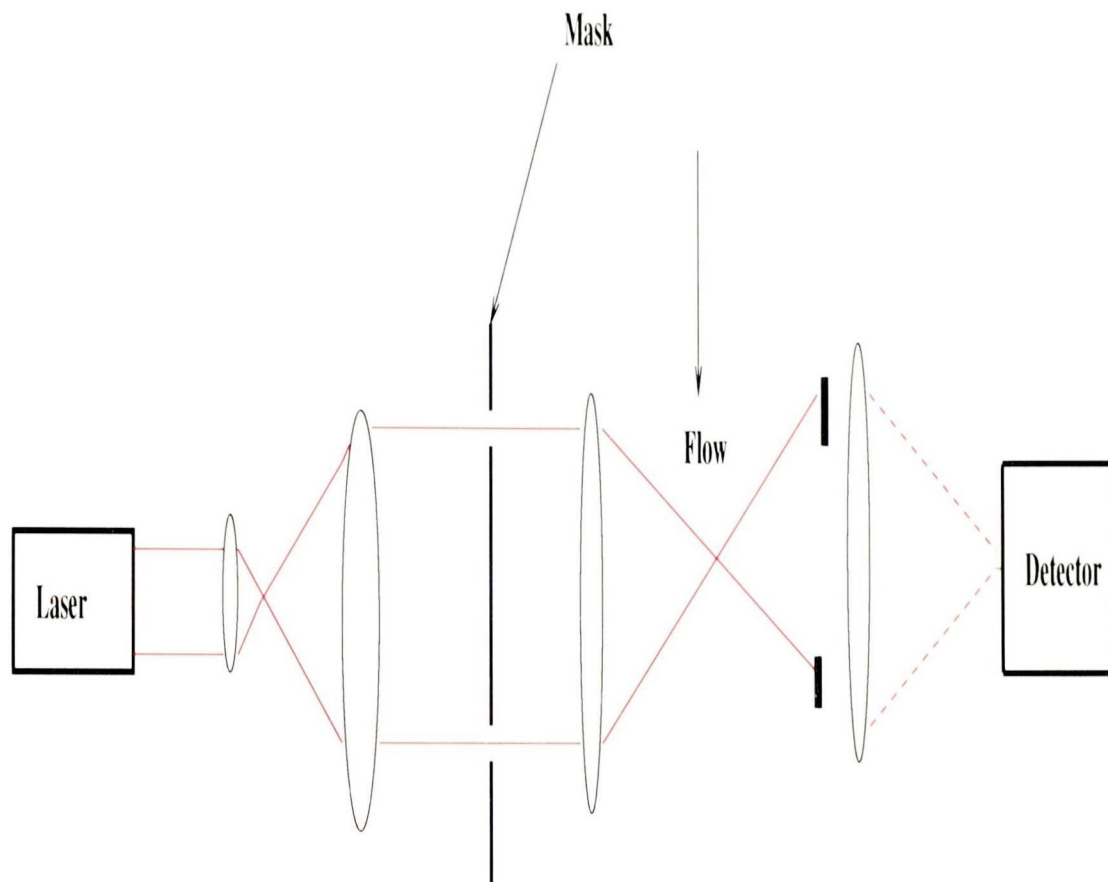


Figure 5.4.1: Modified Version of the Optical system Proposed by Rudd

The major draw back encountered with the Rudd system is that the unscattered portion of the beam falls directly onto the photo detector, hence the small fluctuations would appear as noise. The modified version of the Rudd system is the most commonly used LDV setup and is referred to as the forward scatter real fringe system, as shown in Figure(5.4.2).

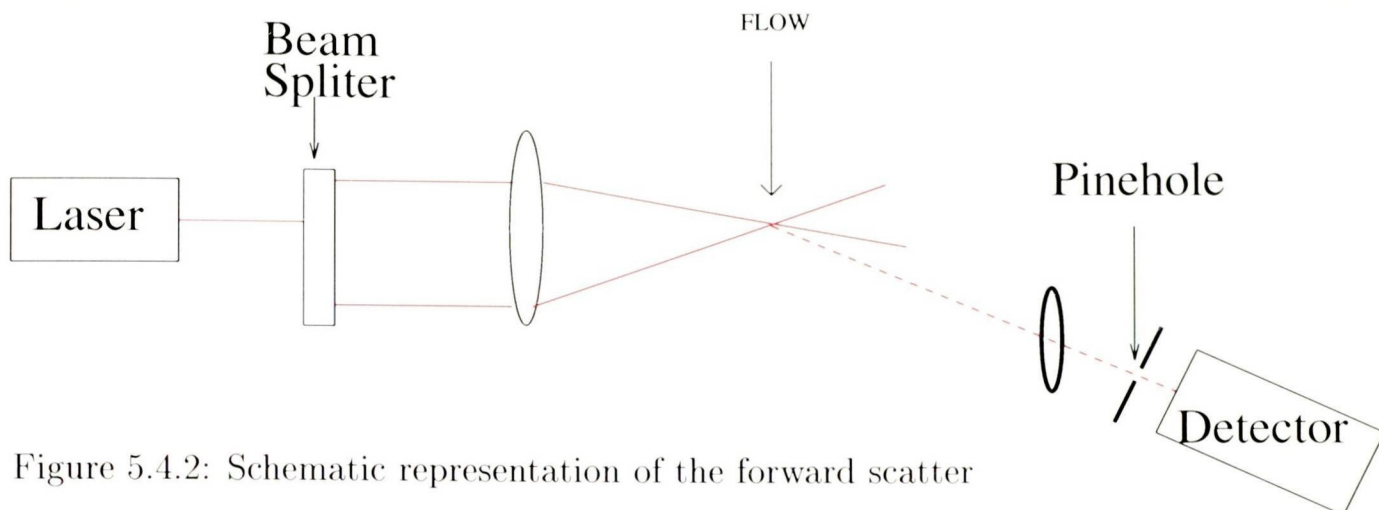


Figure 5.4.2: Schematic representation of the forward scatter real fringe LDV System

### §5.5 Backscattering Geometries

This system only requires one opening to make the necessary measurements, however the down side of this system is that it requires lasers with higher intensities than the forward scatter configurations. The backscatter arrangement is shown in Figure(5.5.1). The lens  $L_1$  brings the two beams to a focus at the measuring point and the light scattered in the backward direction is collected back through the same lens and deflected by the mirror. A second lens  $L_2$  projects the fringe onto the photodetector. A pinhole in a mask  $M_2$  can be used in front of the detector to limit the observation volume. The other advantage of this system is that once it is aligned at construction the system does not need to be realigned again.

### §5.6 The Side Wall Effect

In any kind of flow measurements involving optical systems, the beam has to travel through the air and the side wall of the container. This would cause the beam to refract due to changes in density. The Doppler frequency is determined by the half-angle  $\theta$  between the beams at their point of intersection. The refractive index  $n_f$  of

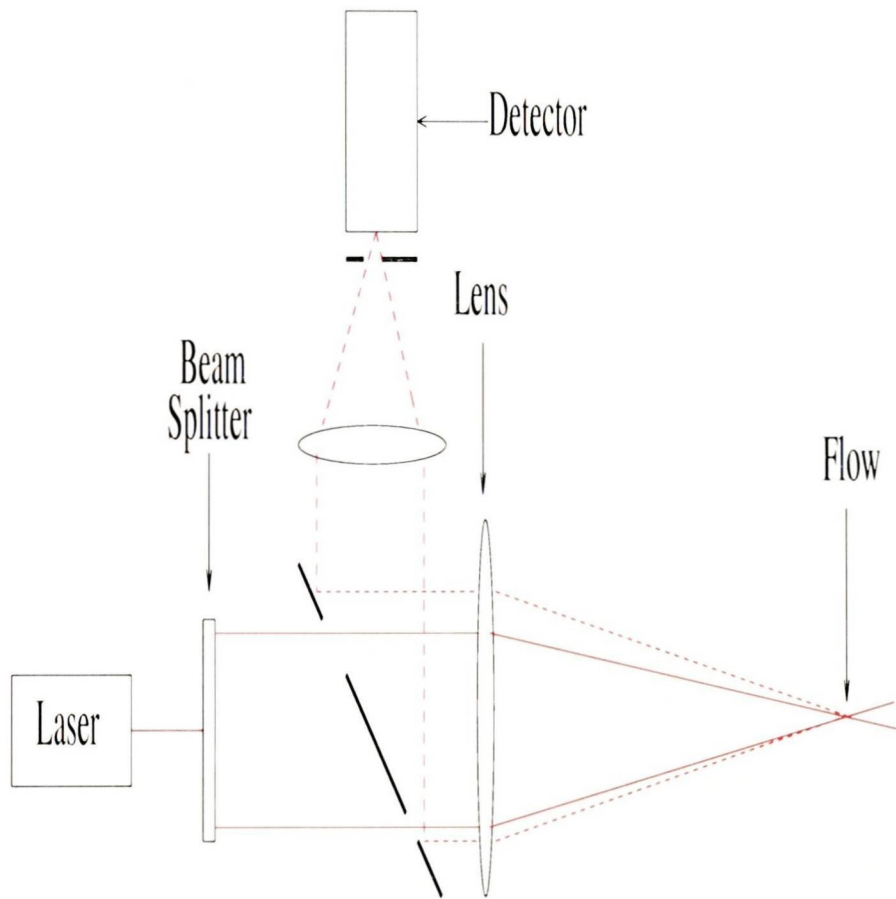


Figure 5.5.1: Typical backscatter optical system

the fluid and the free space wavelength  $\lambda$  which is constant for a given light source. The expression for the Doppler frequency  $f_0$  can be derived and be shown that the Doppler frequency is independent of the refractive index effects. If we assume the angle between each beam and the optical axis is  $\theta_a$  in air, and that the refractive index for air is given by

$$n_{air} = 1$$

$$\sin \theta = \frac{\sin \theta_a}{n_f},$$

irrespective of the side wall effects. The Doppler frequency can be written as:

$$f_0 = \frac{(2U \sin \theta_a)}{\lambda} \quad (5.6.1)$$

The above result would eliminate the effect of wall refractive index for uniform wall thickness situations. It must be pointed out that for non uniform walls this effect must be taken into account, but is beyond the scope of this work.

### §5.7 Frequency Shifting

In most industrial situations, the velocities are continuously changing signs. The implication being that the lower Doppler systems produce signals with the same frequency whether the particles are moving forward or backwards. This problem can be overcome by incorporating a form of frequency shifting device. The most commonly used device of this type is known as the Bragg cell, as shown in Figure(5.7.1). The Bragg Cell is placed in the path of one beam. The beam is refracted as it emerges through the Bragg cell and is re aligned by incorporating mirrors. A mask is placed in the path of the beams with two narrow apertures so that only first order beams are allowed to pass through. The frequency shift is therefore superimposed on the Doppler frequency shift and is equal to  $\omega_s$ (which is the frequency of the acoustic wave), this implies that, the frequency is independent of the angle  $\theta$  at which the focused beams converge. This arrangement is used in many LDV set-ups.

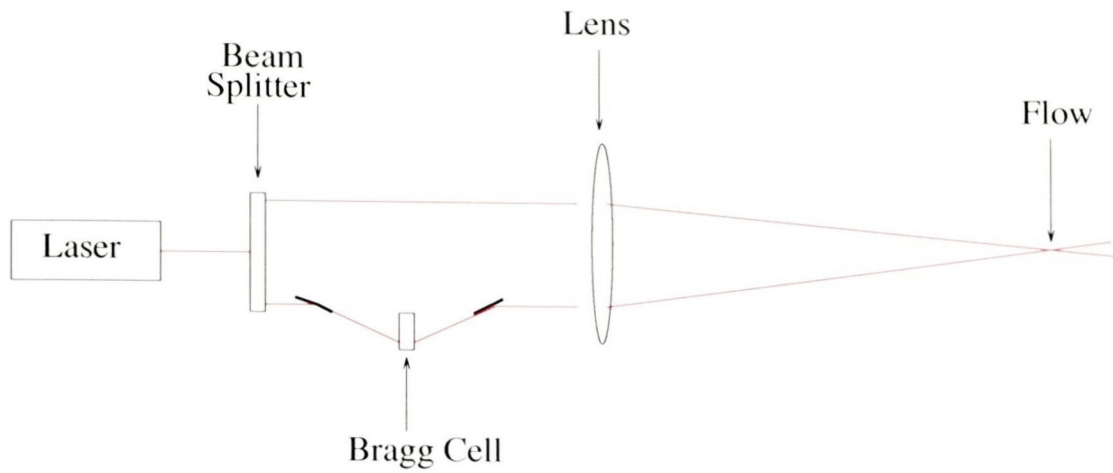


Figure 5.7.1: Braggcell Configuration

### §5.8 Experimental Procedure

#### §5.8.1 Laser Doppler Anemometry

A Ventolin<sup>TM</sup> Inhaler utilises a canister of compressed propellant and drug in powder form to disperse a metered 100 micrograms of Salbutamol per actuation. The canister is inserted within a plastic holder with a central nozzle positioned centrally in the exit orifice. The inhaler is then inserted into the Volumatic<sup>TM</sup> Spacer Device from which the patient inhales the drug. The compressed liquid propellant exits the nozzle orifice carrying the powder particles in a two-phase jet flow. The propellant evaporates, leaving the particles dispersed in the gas phase. The particle motion is characterised by unsteady and turbulent interaction with the surrounding quiescent gas. The jet flow is bounded by the volume of the Spacer Device and is observed to collide with the opposite walls of the chamber and circulate back towards the nozzle orifice. As such, any velocity measurement must be time-stamped to enable differentiation between those measurements performed during injection and those observed between injection events.

### §5.9 Experimental Apparatus and Setup

The experimental apparatus was set-up as shown in Figure(5.9.1).

The spacer device was mounted horizontally using two sets of glass lens holders onto an optical rail with height adjustment. A third lens holder with rigid jaws and a rotational vernier allowed the device to be held securely and rotated about its axis of symmetry. The device was aligned such that the inhaler orifice was horizontal to the plane of the optical bench. The mounting assembly is shown in Figure(5.9.1). The optical rail and assembly were mounted on a two- axis, rectilinear, automated traverse made by Time and Precision Instruments. A customised software controlled the fine movements of the probe, relative to the grid, within the Volumatic<sup>TM</sup> spacer. The traverse operates with fine pitch lead screws and stepper motors to achieve a positional accuracy to within  $\pm 0.2$  mm.

The automated traverse, optical rail, spacer device and LDA transmission optics were mounted on a vibration isolation air breadboard as shown in Figure(5.9.2). The reference point for the LDA measurements (and the traverse read as zero) was chosen at a point co-linear with the centre of the orifice cross-section and 5 mm from the vertical plane of the exit orifice of the inhaler. The grid for the measurement points were then defined relative to this point and the traverse was computer programmed to move the LDA probe, measuring volume over a two-dimensional grid within the vertical symmetry plane of the spacer device.

The probe targeting was achieved by the use of a dummy inhaler holder with an orifice packed with epoxy filler. The filler was smoothed to be level with the edges of the orifice. A vernier calliper was used to find the centre of the orifice. A 1 mm diameter hole was drilled at the centre and a fine pin was inserted until only 5 mm protruded perpendicular to the level surface. This was verified with a depth micrometer and the pin glued into place. The LDA beam intersection was then focused onto the tip of the pin using the method of tuning the photomultiplier anode current with the

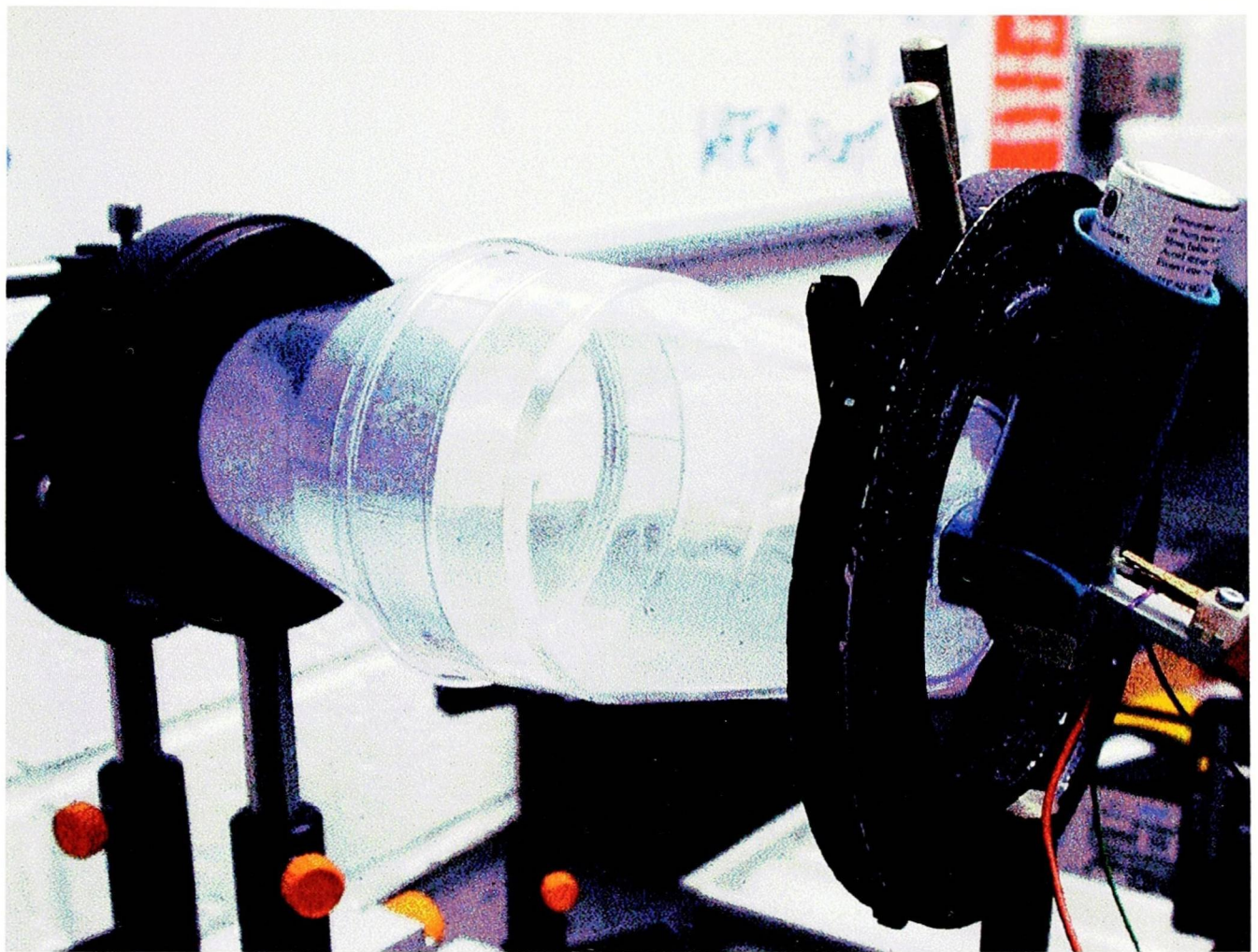


Figure 5.9.1: Lens Mounting Assembly of The Volumatic Spacer

processor operating with the internal trigger mode. The probe volume was returned to this point and the method repeated after each sweep of the grid points to ensure repeatability.

A single component, backscatter LDA system, based on a Spectra- Physics Stabilite 2017 argon-ion laser (green line at  $\lambda=514.5$  nm) was used in conjunction with a Bragg cell, operating as both a 50/50 beam splitter and a 40 MHz frequency shifter. The coherent beam pair was then transmitted via a fibre-optic cable to a  $\phi 14$  mm Dantec Fibre Flow probe fitted with a times four beam expander and front lens. The powder particle diameters were not known and therefore some preliminary tests were undertaken to assess the effect of the fringe spacing in the LDA probe volume on the measured velocity and turbulence intensity distributions and the validated data rate.

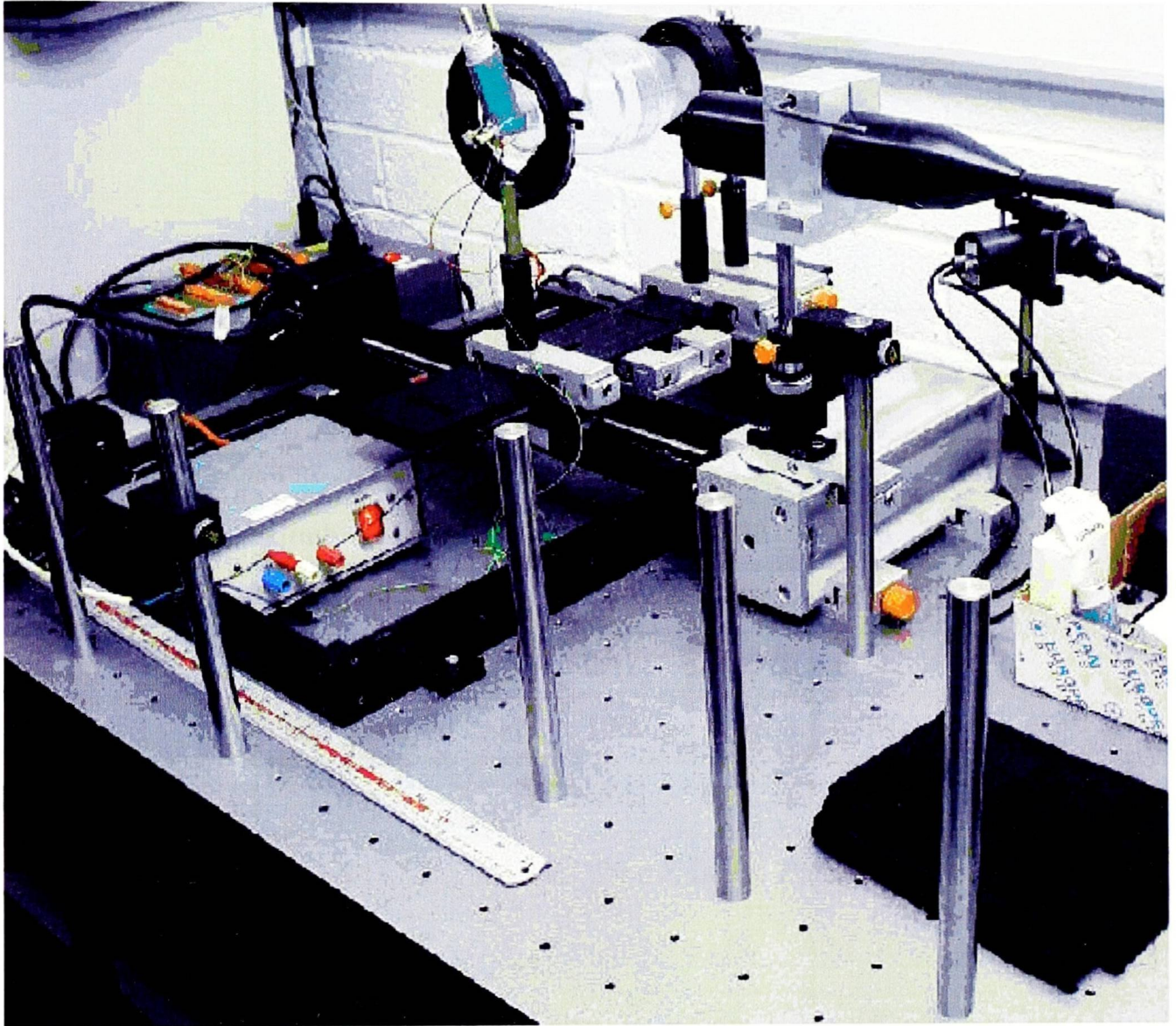


Figure 5.9.2: Optical Breadboard and Optics

## 5.9. Experimental Apparatus and Setup

---

Three optical configurations were tested as presented in Table(5.9.1). In each case, measurements were performed over the entire grid using suitable bandwidths to include all velocity ranges. The output was processed by a Dantec 58N80 MultiPDA Signal Processor. The Doppler Bursts were band pass filtered to remove the low frequency Gaussian beam profile and any high frequency noise from the signal. Furthermore, the bandwidth and the gain of the LDA processor were selected depending on the location and the range of velocities to be measured.

Focal length (mm)	50	160	400
Beam Separation (mm)	8	32	32
Fringe Spacing (mm)	3.23	2.58	6.44
Number of Fringes	38	38	38
Probe Volume $\Delta x$	0.1216	0.0975	0.2428
Probe Volume $\Delta y$	0.1213	0.0970	0.2426
Probe Volume $\Delta z$	1.5212	0.9753	6.0704

Table (5.9.1) LDA Optical Transmission Parameters

To enable time series of measured velocity data from the start of injection to be acquired, it was necessary to instrument the inhaler such that the depression of the canister inside the holder would trigger the start of measurements using the LDA processor external encoder input. A single holder was modified externally so that a micro-switch could be attached to the lower part as shown in Figure(5.9.3). One contact arm of the switch protruded several millimetres inside the holder, at a level just beneath the normal (dormant) position of the raised shoulder on the canister. Once the canister is depressed, electrical contact is made and the LDA processor

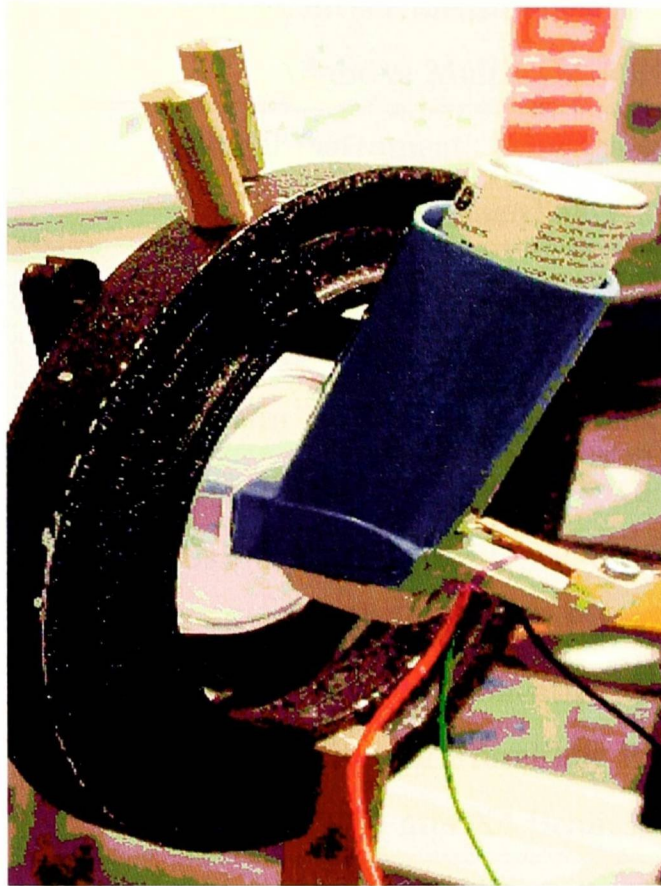


Figure 5.9.3: Inhaler Trigger Switch Arrangement

receives a trigger signal. The time is only reset when the canister is depressed once again. The LDA system specification used for the above study are shown in Table(5.9.2).

## 5.10. Methodology

Signal Processor	Dantec/Invent Measurement technology Adaptive MultiPDA 58N80
Interface	National Instruments Data translation PCI Interface Board 58G130
Laser	Spectra-Physics Stabilite 2017 5W Argon Ion Laser (=514.5 nmgreen) Spectra-Physics 2670 remote Controller and Transformer
Transmission	Disa 40 MHz Bragg Cell Dantec 60X24 fibre-Optic Manipulators Anaconda Sealite Single Strand Fibre-Optic Cable and light Sheath Dantec $\phi$ 14 mm FibreFlow Probe Head Dantec $\phi$ 60 mm X4 Beam Expander
Collection	Dantec Classical PDA Collection Optics Disa PMT (x3) 55X08

Table (5.9.2) The LDA/PDA System Specification

### §5.10 Methodology

The measurement locations are shown in Figure(5.10.1). The choice of the final grid locations was based on a set of extensive measurements carried out across the complete chamber. A compromise was sought between available data (points in the jet flow with good data rates), the number of depressions of the canister required to produce a statistically significant data set (differing at each location) and the number of canisters available. In addition, care was taken to avoid locations where changes in the thin wall of the spacer device deviated the beam or introduced regions of high backscatter light intensity from internal reflections. Preliminary tests were performed to study the following points:

- Study the effects of consecutive injections and nozzle fouling; the likelihood of the first injections of a new canister being unrepresentative of the subsequent injections;
- The effect of the period between consecutive injections
- The performance of the individual injections up to 200 doses (decay)

Based upon these findings, the following measurement procedure was devised. Measurements of instantaneous velocity and turbulence intensity were made in a single plane of symmetry bi-secting the spacer device volume, and recorded at a total of 34 points along four vertical height positions in the y-direction, in increments of 5 mm along the x-direction, to a maximum distance of 55 mm from the orifice exit plane. The positive velocity direction was taken as the positive x-direction away from the nozzle exit. For each measurement point, the canister was shaken and the first 25 charges dispelled (in order to account for any irregularities in the discharge). Data was then collected for 25,000 validated velocity measurements or until ten consecutive shots from the inhaler were completed. A period of several seconds separated each injection event.

The number of collected velocity samples at each point was dependent on the validated data rate and the number of available canisters to complete all tests. In any one set of tests, the number of charges from a single inhaler never exceeded 100, even though the inhalers were rated for 200 metered doses.

Between each set of measurements, the traverse moved the spacer device to the next grid location and the nozzle was cleared of frozen deposits. After each set of four test points, the canister was changed and the spacer device removed and cleaned with warm water. This maintained the signal to noise ratio at an acceptable level. For a range of grid locations, measurements were repeated to ensure data consistency (three times along the  $y = 0$  plane). These were repeated for the range of probe volume sizes given in Table(5.9.1) A 160 mm focal length transmission lens with 32 mm beam separation was chosen to give the highest data rate.

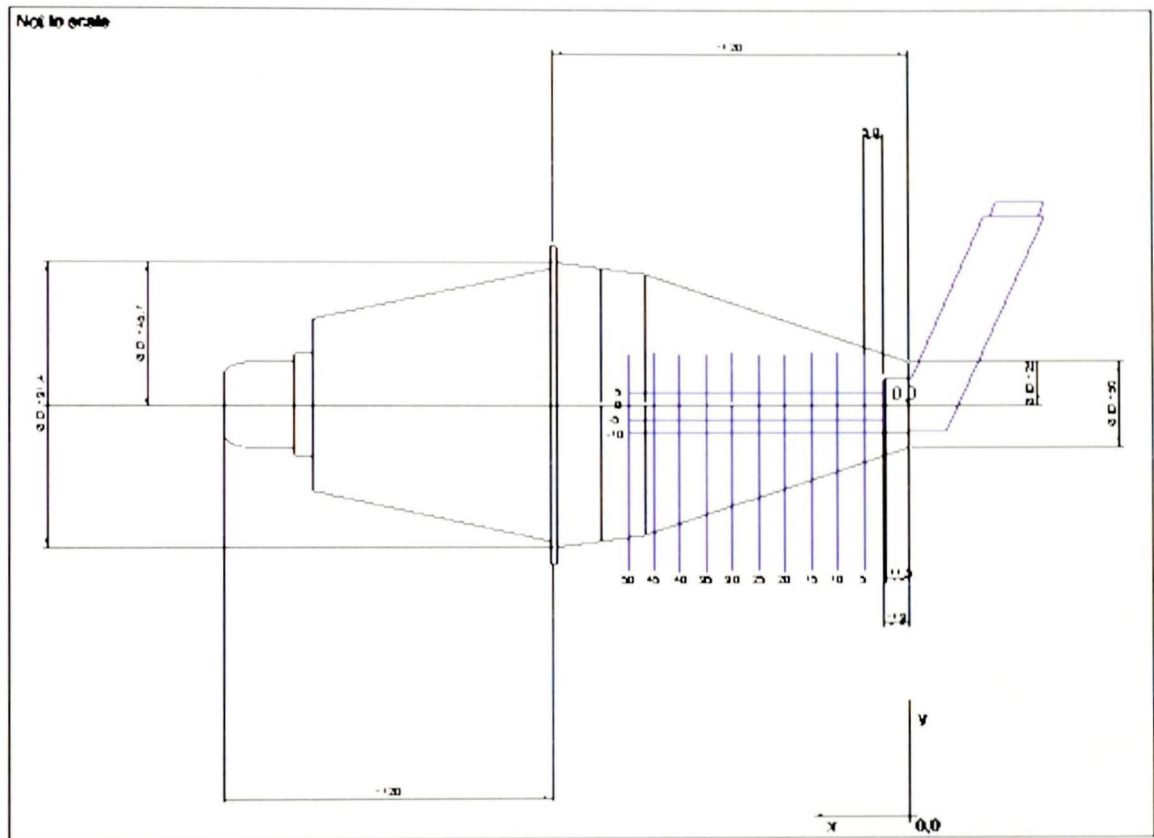


Figure 5.10.1: Measurement Grid Used In the Study

### §5.11 Flow Visualization

#### §5.11.1 Introduction

In flow studies it is of interest to visualize the flow field in thin plane layers. The laser light sheet technique is a useful tool for obtaining a better understanding of the flow characteristics Johnson et al. <sup>(35)</sup>, Rouse <sup>(59)</sup>, Nebeker <sup>(49)</sup>, Baev, <sup>(3)</sup>. The light sheet is a thin plane layer of approximately 1 mm of thickness which is illuminated normally by a high-power laser. The particles in the flow reflect the laser light while passing through the light sheet. Due to the scattered light, these particles are visible and their flight paths can be optically recorded.

#### §5.11.2 Laser Light Sheet Unit

In order to visualize flow light sheet has to be generated in the flow field. As a general rule, continuously operated or pulsed high-power lasers are used to create the light sheet. The light sheet behind the focal point is created by means of collimating the beam, using a cylindrical lens. The thickness of the light sheet is determined by the diameter of the collimated laser beam. To increase the light intensity in the visualization area of interest, the light is concentrated by fibre-optics and a cylindrical lens in the horizontal direction

#### §5.11.3 Experimental Set-Up

In order to conduct flow visualization studies, an experimental set-up was designed to record the images of the drug injection into the spacer by means of a laser light sheet technique as shown in Figure(5.11.1). The visualization technique works on the principle that when particles pass through the light sheet, they scatter laser light

and become visible. Within the light sheet an image of the flow pattern appears that can be recorded by a CCD camera. The high speed camera has the following specifications:

- Kodak Ektapro HS motion analyzer 4450
- CCD-sensor 256x256 pixel
- Full-frame 4500 frms/s respectively
- Sensitivity of 0.1 lux.

Due to the low speed data transfer from the digital interface of the motion analyzer to the digital image processing computer (PC PIII-450), an analogue video signal is used, i.e. the signal is digitized online by means of a fast frame grabber board (Imaging Technology IC-PCI AM-FA) and stored on a PC hard disk. In addition the analogue video signal was also stored on video tape for reference.

### §5.12 Conclusion

The Laser Doppler experiments were relatively expensive to design and set up and required highly accurate equipment. There had to be considerable planning prior to running the experiments. A trigger switch had to be designed to activate the LDA and measurements and the drug injection simultaneously. The accuracy of the experiments were maximized by dispelling the first 25 charges and then data was collected for 25,000 validated velocity measurements. The nozzle was cleared of frozen deposits prior to the next measurements.

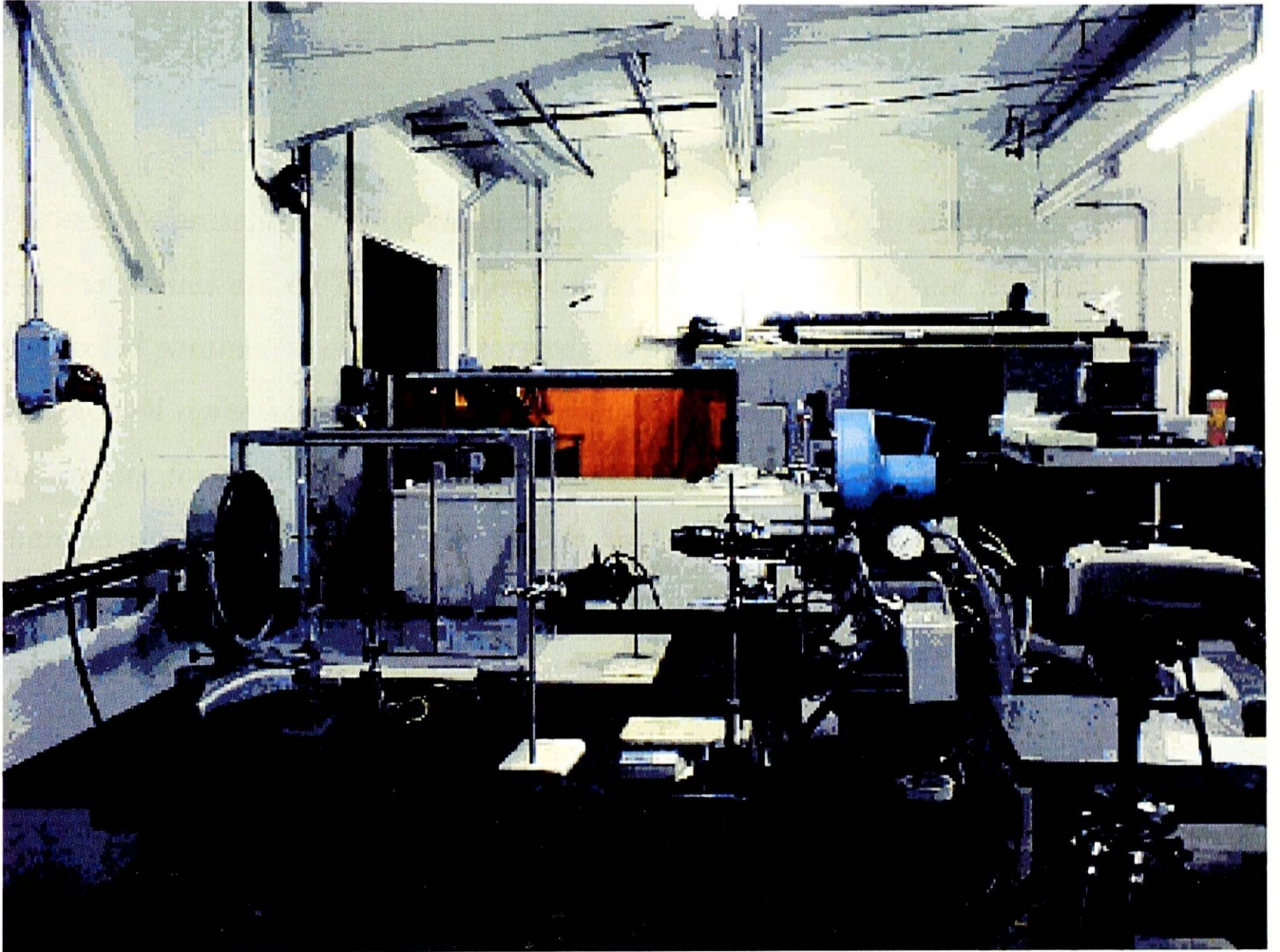


Figure 5.11.1: Flow Visualization Equipment

*The results presented in this chapter are a combination of three different techniques. The techniques are CFD, Laser Doppler Anemometry (LDA) and flow visualisation. A detailed parametric study was carried out for the Volumatic<sup>TM</sup> and the results have shown good agreement with the LDA and flow visualisation results. In this chapter the results for a more efficient drug delivery device similar in design to the Aero chamber are also presented. The results have shown efficiencies in the order of 71% compared to the current design which is only about 10% efficient. The findings from this novel study have lead to the following publications [Jalili <sup>(30)</sup>, <sup>(31)</sup>, <sup>(32)</sup>, <sup>(33)</sup>, <sup>(34)</sup>]*

### §6.1 Introduction

In recent years efforts have been made to improve the amount of drug reaching the affected region,[Newman <sup>(51)</sup>,Moren <sup>(46)</sup>, Versteeg <sup>(69)</sup>]. The research has mainly concentrated around the actuator and the nozzle itself. This research has taken the view that, the delivery device, in this case the spacer, plays a far more important role than it has been given credit for. Furthermore to our knowledge no CFD or experimental study has been undertaken to optimise the design of the current commercially available spacer. It will be shown in the results section, how a commercial CFD code has been used in carrying out a series of parametric studies, in order to optimise the design of the Volumatic<sup>TM</sup>, thus improving the amount of drug delivered to the

affected region. In order to achieve an optimum design in terms of drug delivery the research had to be performed as a multi-disciplinary task and broken down into the following stages:

- Initial study using air
- Parametric study
- Experimental study
- Flow visualization

In the initial part of the research, the aim was simply to gain an understanding into the flow patterns within the spacer. The study was carried out by injecting air carrying a concentration into the spacer. This represented a simple model of the drug.

In the first part of the research the commercially available Volumatic<sup>TM</sup> was modelled using the simple model of the drug discussed above. In this study flow patterns and regions of recirculations were highlighted, the study also highlighted the time step and the region where maximum concentration occurred. In this part of the study a series of parametric studies were carried out. These included different jet configurations at the inlet to the spacer. The second part of this research investigated the effects of changing parameters such as the spacer length, and the shape of the spacer device in terms of the drug delivery efficiency. The parametric study revealed that the geometry and the length of the device played an important role in terms of drug delivery. The results are discussed in detail under the CFD results section. The experimental study was carried out in two parts. Initially flow measurements were made using LDA to provide a value for the exit velocity of the drug into the spacer and validating the CFD model using air. In the second part of the experimental study a series of detailed LDA measurements have been taken from the nozzle along the centre line up to the mid way point in the spacer. There have also been vertical

measurements (along the Y axis) at four different locations. At each location 25,000 data samples have been taken and their value averaged. Each measurement location has been separated by 5 mm from the previous measurement location.

Finally laser light sheeting technique has been employed to capture the flow field in the spacer. The high speed camera used recorded 4500 frames per second. The frames were then analysed and equivalent time steps have been compared.

### §6.2 CFD Results

This study was carried out as a 2D polar axisymmetric analysis, and two different codes have been used. The commercial codes used were Fluent 5.3.1 and Phoenics 2.1.3

In the current study the following assumptions have been used:

- The particles do not have any static charge
- The particles do not stick together
- There is no static charge between the spacer and the particles, hence the particles do not stick to the sides of the spacer
- The drug does not change phase within the spacer

#### §6.2.1 Boundary Conditions

Inlet Velocity in the axial direction = 40m/s

V-velocity = 0m/s

No-slip boundary conditions at the walls

The flow is axisymmetric

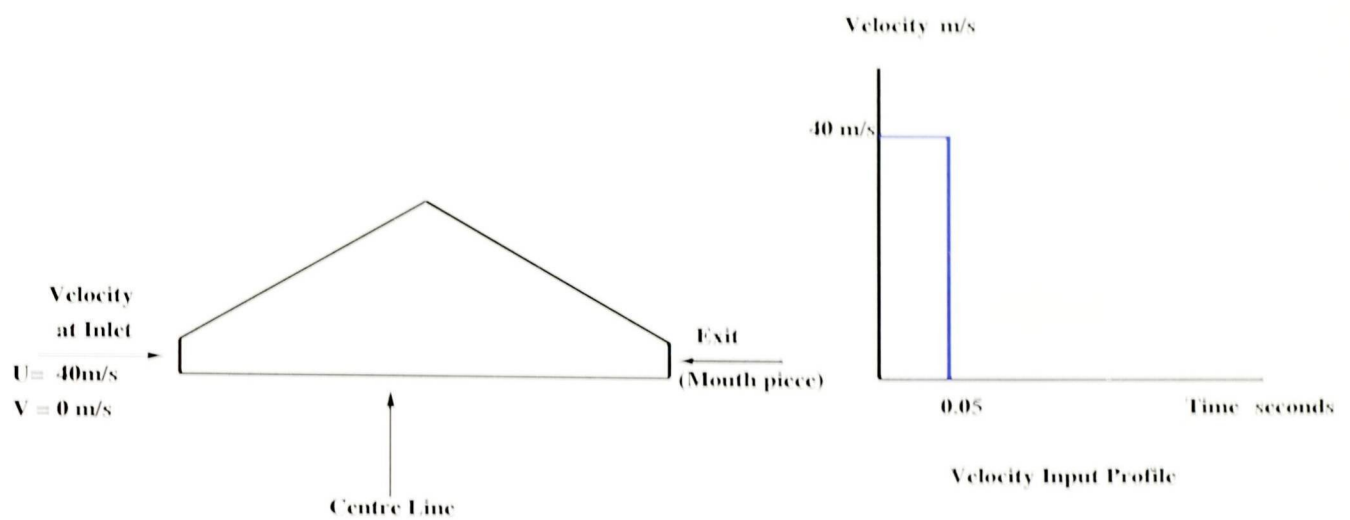


Figure 6.2.1: Boundary conditions for the CFD simulations

Drug composition by mass fraction

propellant 0.98

Drug Liquid 0.01

Propellant vapour 0.01

Turbulence intensity 43%

Characteristic length 0.007m

Particles of 0.005 mm in diameter are injected at the inlet. the particles are of evaporating and inert type

The drug composition was eventually obtained from Astra Zeneca Pharmaceutical Company. The CFD simulations were carried out six months prior to LDA experiments. The boundary conditions discussed in this section refer to Figure (6.2.1). The inlet velocity was set to 40m/s. The inlet velocity was kept at the given value for a duration of 0.05 seconds, then the value was set to zero for the duration of the cycle, i.e. the remaining 0.95 seconds. The values for turbulence intensity and characteristic lengths were obtained by running a number of simulations until the separated jet was captured numerically. The values at this stage were then chosen to be the correct initial values for the CFD case analysed.

## §6.2.2 Grid Dependency test

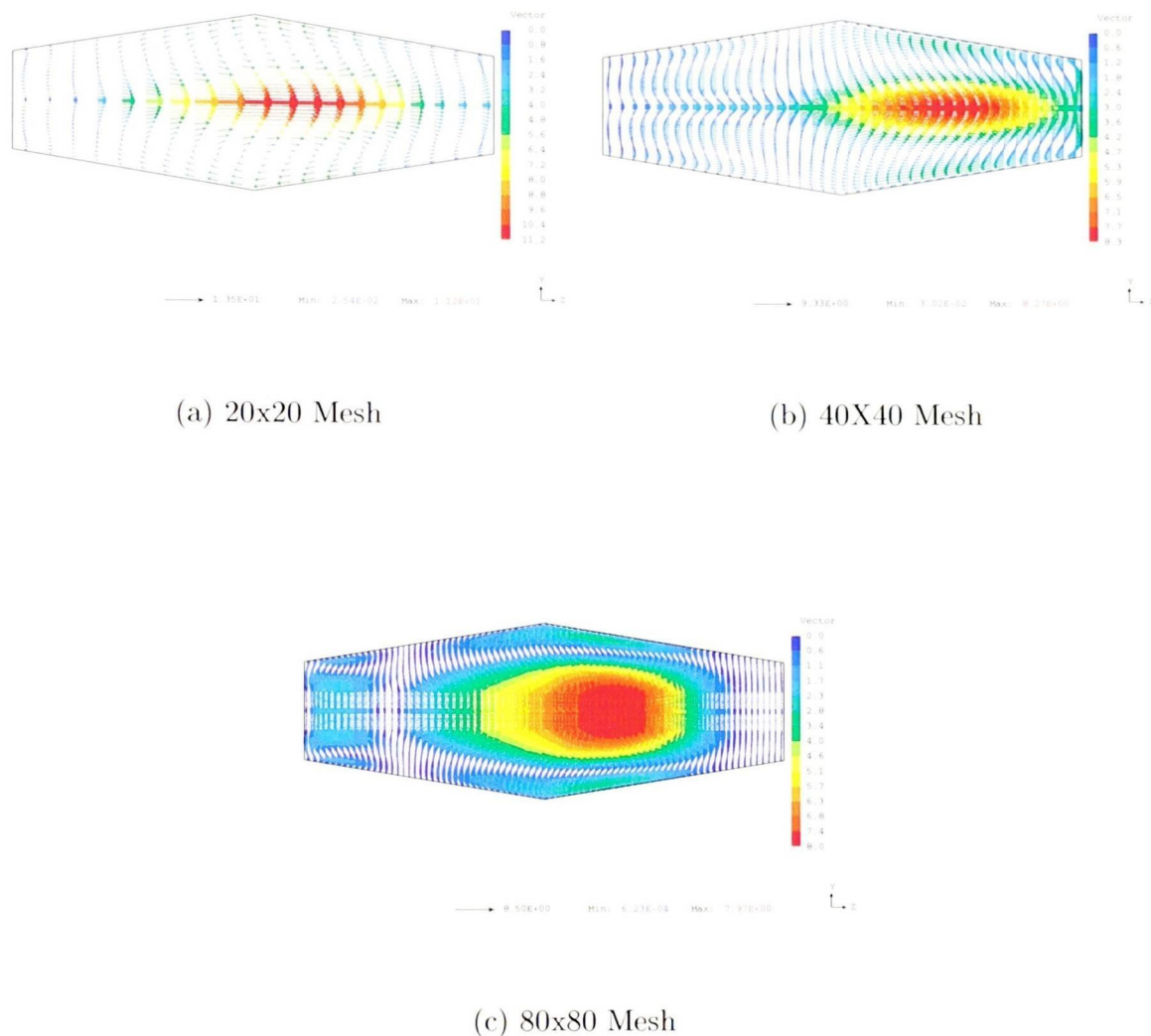


Figure 6.2.2: Vector Plots Showing The Effect of Different Meshes Used In This Study

In any CFD simulation it is important to have a fine enough mesh to capture all the flow characteristics, yet at the same time one needs to strike a balance between the accuracy required and the computational time needed to arrive at the pre-defined accuracy value set. In the present study four grid arrangements were used, these were 20x20, 40x40, 80x80 as shown in Figure(6.2.2).

It was known that the maximum velocity value was 40 m/s just as the drug left

the nozzle along the centre line, therefore this location was chosen when comparing the velocity values for different meshes. The values for different meshes have been plotted along the centre line as shown in Figure(6.2.3). It can be seen from this figure that the level of accuracy improved very marginally by increasing the mesh density from 80X80 to 200x100. The above findings were verified by analysing the velocity contours at the initial and final time steps for different mesh configurations. These are shown in Figure (6.2.4a- 6.2.4.f).

The first mesh arrangement to be analysed was the 20x20 mesh. At the initial time step i.e. 0.05 seconds as shown in Figure (6.2.4a), it can be seen that the jet of air has entered the spacer with a captured velocity of 38.84 m/s compared to the 40 m/s which has been reported in the literature. The extent to which the jet has advanced in the spacer is not clear. It is clear looking at the jet profile that, the, middle section of the jet around the centre line is travelling with maximum velocity, as is expected. At time step 1.0 second it can be seen from Figure (6.2.4b) that the jet has advanced to the mouth piece end of the spacer, creating a large recirculation region around this area. The maximum velocity at this time step has reduced to 12.7 m/s compared to the 40 m/s at time step 0.05 second. It was expected that at this time step the complete detachment of the jet could have been observed, but this is not clearly the case as can be seen in Figure (6.2.4b). There are symmetrical recirculation regions, one on either side of the jet inlet and one near the top wall and a similar one near the bottom wall of the chamber.

The next case analysed was the 40x40 mesh, this is shown in Figures (6.2.4c-6.2.4d). In the initial time step i.e. 0.05 seconds the jet of air has entered the spacer, once again the recorded velocity at 39.83 m/s, is below the recorded 40 m/s velocity. At the final time step during the cycle it can be seen clearly that the jet of air has detached itself from the inlet and there are three recirculation regions present within the spacer. There are two recirculation regions opposite each other near the exit or the mouth piece of the spacer and one recirculation region near the inlet from the nozzle.

The 80x80 mesh is shown in Figures (6.2.4e-f). It can be seen from Figure(6.2.4e) that the jet of air has been captured accurately and the extends to which it has penetrated into the spacer is clearly defined. This is a big improvement compared to the previous four figures. The velocity contours also have clear region showing the changes in the jet velocity. The maximum recorded velocity is 40 m/s, which is a very small region shown in red. At the 1.0 second time step the maximum jet velocity has reduced to 0.07 m/s as shown in Figure (6.2.4f). It can be seen from the same figure that the jet has completely detached itself from the inlet region and there is a large recirculation region near the mouth piece. It can also be observed from the same figure that, there are a further four smaller recirculation regions. There are two on either side of the inlet and a further two on either side of the big recirculation region near the top and the bottom wall of the spacer. This has confirmed that it was not necessary to use a larger mesh than 80x80.

The mesh was refined further just to ensure our solution was mesh independent. The mesh was increased to 200x100 in x and y directions respectively. This further refinement did not reveal any further flow characteristics. The results are plotted and shown in Figure (6.2.3).

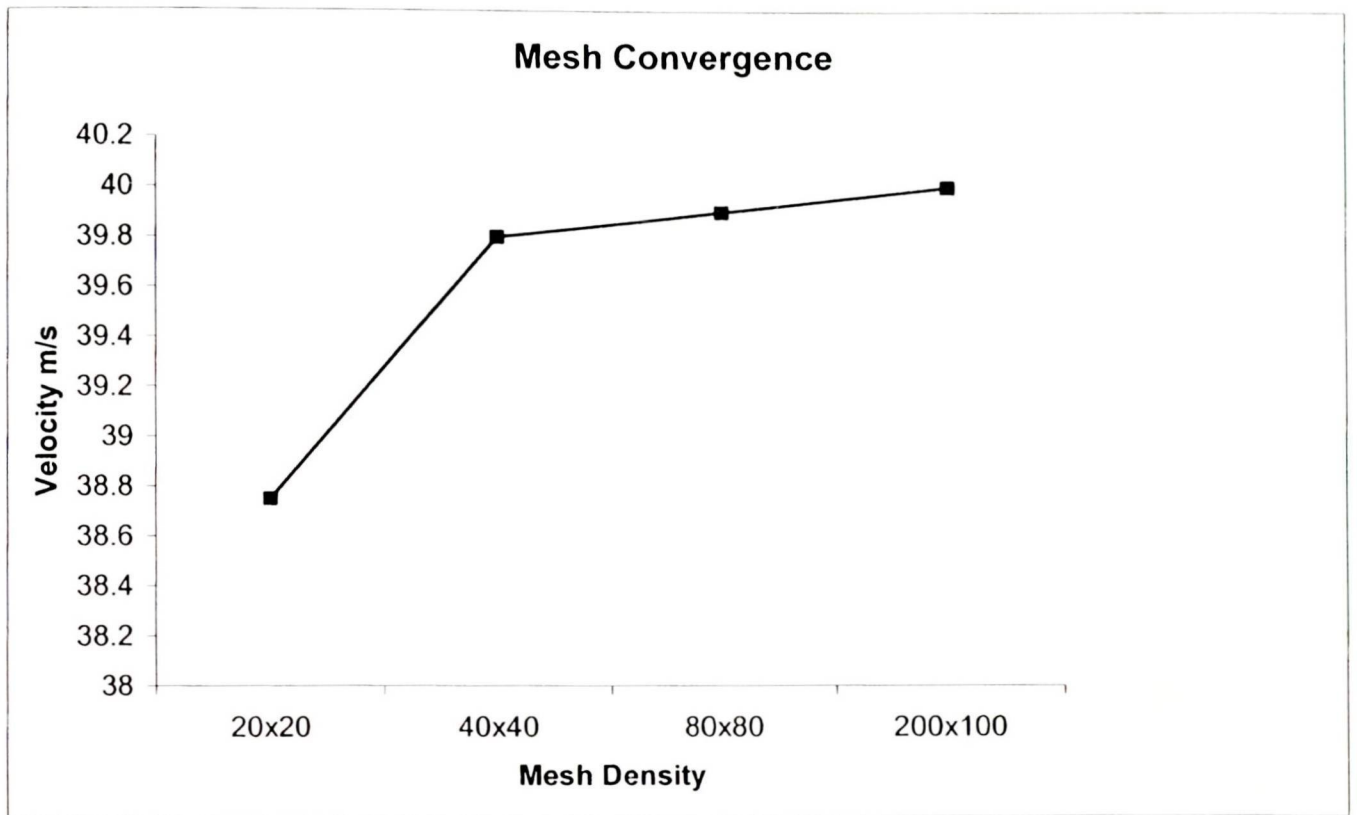
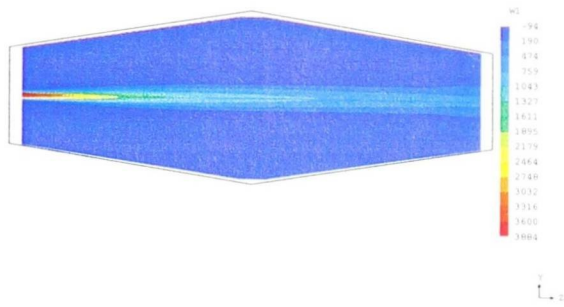
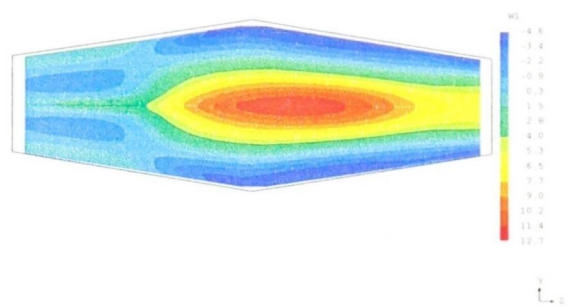


Figure 6.2.3: Converged Velocity Values For Different Meshes Used  
Velocities Plotted along the Centerline

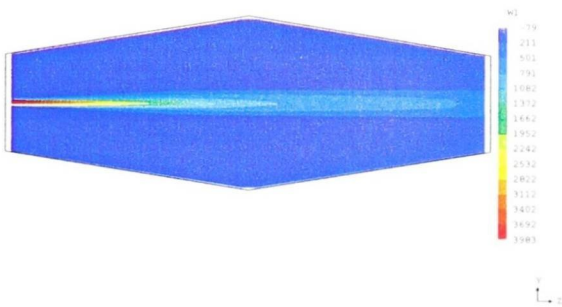
## 6.2. CFD Results



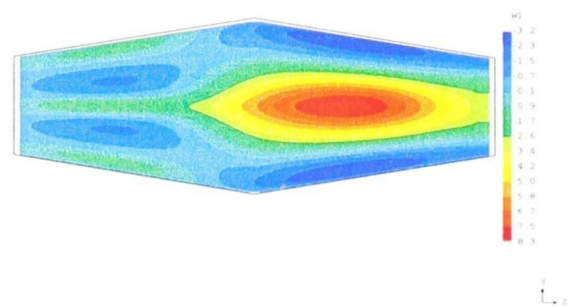
(a) Velocity Contour Time Step 0.05  
20x20 Mesh



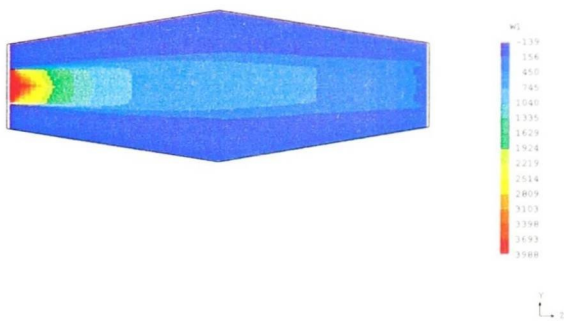
(b) Velocity Contours Time Step 1.0  
Sec. 20X20 Mesh



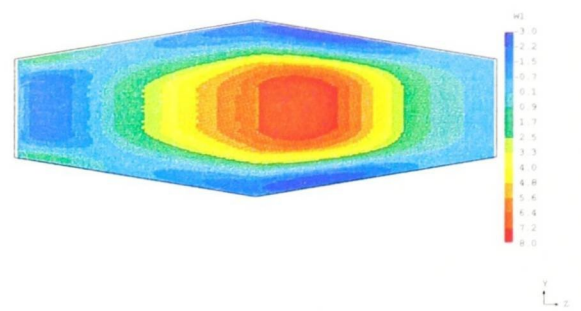
(c) Contours of Velocity Time Step 0.05  
Sec. 40x40 Mesh



(d) Contours of Velocity Time Step 1.0 Sec.  
40X40 Mesh



(e) Contours of Velocity Time Step 0.05  
Sec. 80x80 Mesh



(f) Contours of Velocity Time Step 1.0 Sec.  
80X80 Mesh

Figure 6.2.4: Mesh Dependence Study

### §6.3 Parametric Studies

A detailed study was carried out, investigating the effects each parameter had on the efficiency of the device. The parametric study is described in the order it was carried out. For each simulation a snap shot at four different time steps has been plotted. The obvious starting point was to use the current Volumatic<sup>TM</sup> which has a length of 24 cm and a diameter of 9 cm at its widest point. The mesh used for this study was the 80x80 mesh, this was adequate as shown by the previous section.

The initial case studied was the standard situation encountered by patients using the pMDI and the spacer. The discharge from the pMDI nozzle entered the spacer in the form of a straight jet, Figure (6.3.1a-d) The drug concentration at different time steps during the cycle has been plotted.

At the initial time step i.e. 0.05 seconds the discharge from the nozzle has entered the spacer, Figure (6.3.1a). The jet has a narrow profile and has extended inside the spacer about 2/3 of its length. The drug at this time step was still being injected into the spacer, so the maximum concentration was at the nozzle. It has been shown in Figure(6.3.1a) that the jet of air has entered the spacer and has traveled roughly about two-thirds of the spacer length into the device. The jet has then come to rest and started to diffuse.

At time step 0.4 seconds as shown in Figure(6.3.1b), the maximum concentration had reduced to 0.069 of the original value (1.0), and accumulates near the exit or the mouth piece of the device. This concentration level was in the reported range of 6.9- 10%, [Dolovich <sup>(16)</sup>].

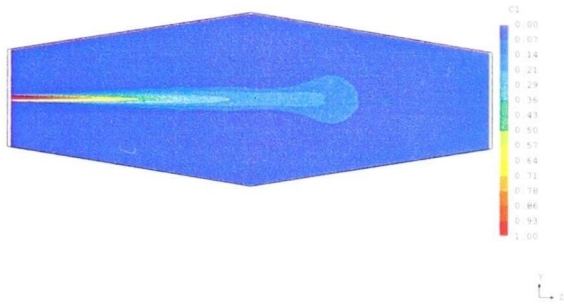
At 0.75 seconds, shown in Figure (6.3.1c), maximum concentration had reduced to 6.6% and the highest concentration levels were around the mouth piece and extended backwards half way in the spacer. It was also observed that about 1/3 of the spacer volume did not contain any drug. The elimination of this empty space would benefit

the manufacturers by reducing the cost of materials and the patients, by making the device smaller and more portable.

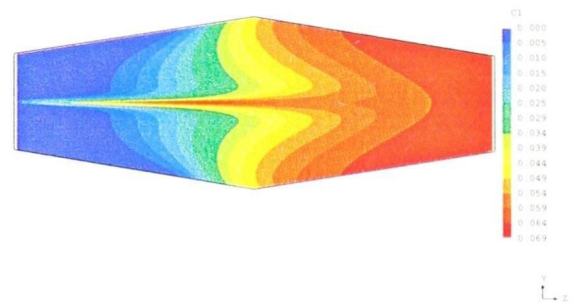
Finally the last time step in the simulation was analysed, i.e. 1.0 second, Figure (6.3.1d) the drug concentration had reduced from 6.6% to 6.5%. The common feature of all the time steps analysed was that, the maximum drug concentration always accumulated around the mouth piece and also about 1/3 of the spacer volume remained empty of any drug. The understanding obtained from the flow studies for the standard Volumatic<sup>TM</sup> design has lead to further parametric studies, in order to optimise the current design.

#### §6.3.1 Jet configuration

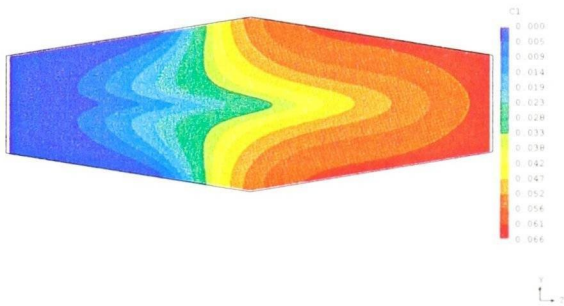
The process of optimising the current Volumatic<sup>TM</sup> design was initiated by looking at the various jet profiles at inlet and the over all effect they had introduced in terms of the drug delivery efficiency and mixing of the drug. For this purpose a number of different jet configurations have been studied. These are shown in Figure (6.3.2). The straight jet configuration has not been discussed here again, as it has been used in detail in the previous section and the grid dependency study.



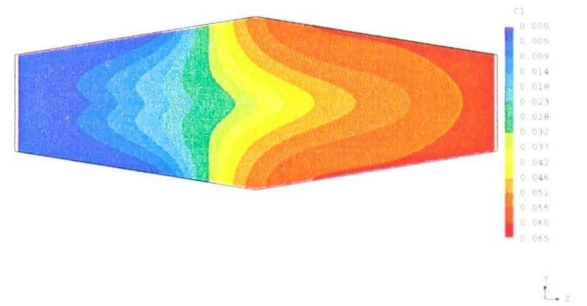
(a) Concentration Distribution Time Step 0.05 Sec.



(b) Concentration Distribution Time Step 0.4 Sec.



(c) Concentration Distribution Time Step 0.75 Sec.



(d) Concentration Distribution Time Step 1.0 Sec.

Figure 6.3.1: Concentration Distribution For Straight Jet

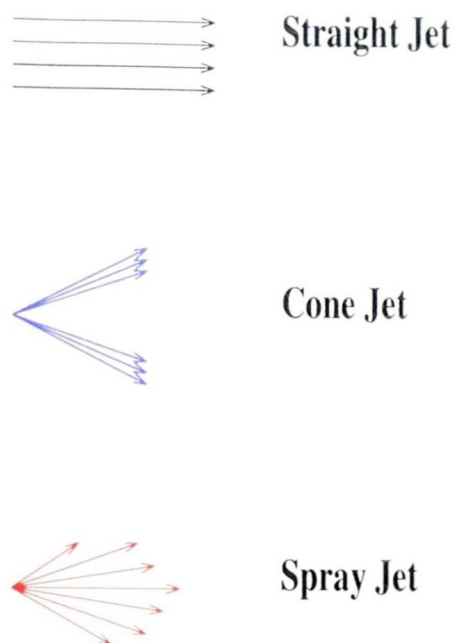


Figure 6.3.2: Different Jet Configurations

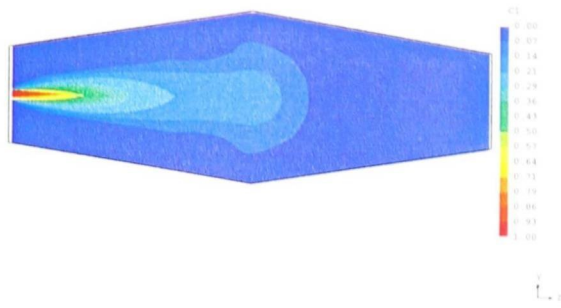
The initial jet configuration study was that of a cone shape. The cone angle was defined to be  $5^\circ$  as shown in Figure(6.3.2). The time steps have been analysed and presented in Figure (6.3.3a-d). It has been shown in Figure(6.3.3a), that at 0.05 seconds, the jet has entered the spacer and travelled approximately half way inside the spacer. The jet was shown to expand out and resembles a mushroom like structure. This was attributed to the highly turbulent nature of the jet within the spacer. At this stage the maximum drug concentration was around the inlet region. This was due to the fact, that the drug was still being injected into the spacer.

The analysis for the time step 0.4 second, shown in Figure(6.3.3b) that there was a considerable amount of mixing taking place. This mixing had helped the whole volume of the spacer to be utilised. At this time step the highest drug concentration level has reduced to 10.2%, however the highest concentration level although large in volume was no longer near the mouth piece, but was surrounded by regions where the drug concentration was lower, near the mouth piece.

At 0.75 second the maximum drug concentration level had reduced to 9.5%. This was slightly lower than the 10.2% recorded at time step 0.4 second. This was not totally unexpected, as it was commonly observed, the maximum concentration occurred around 0.4 second.

The flow patterns at time step 1.0 second were analysed. It is clear that, the maximum drug concentration had reduced very slightly to a value of 9.4%. The highest drug concentration level has spread out more and had extended backwards towards the injection location as shown in Figure (6.3.3d).

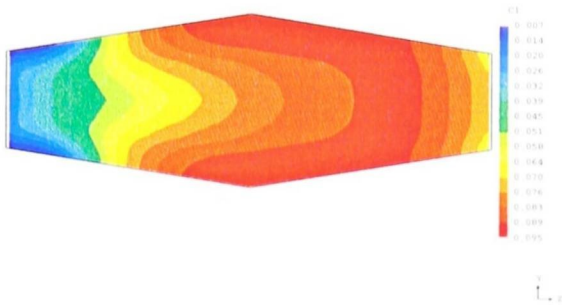
In concluding this part of the research, the conclusions drawn were that, the jet with the cone angle profile had increased the percentage of the drug delivered, but the highest concentration was not found to be near the mouth piece. The second important feature of this study was that, a higher percentage of the volume of the spacer was utilised.



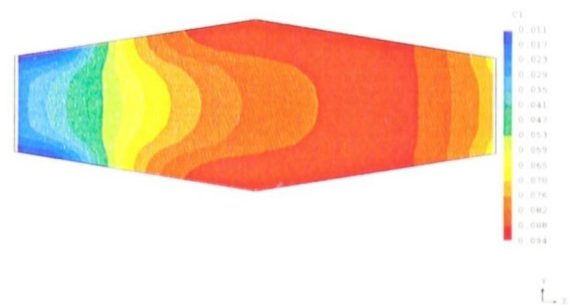
(a) Concentration Distribution  $5^\circ$  Jet Angle Time Step 0.05 Sec.



(b) Concentration Distribution  $5^\circ$  Jet Angle Time Step 0.4 Sec.



(c) Concentration Distribution  $5^\circ$  Jet Angle Time Step 0.75 Sec.



(d) Concentration Distribution  $5^\circ$  Jet Angle Time Step 1.0 Sec.

Figure 6.3.3: Concentration Distribution For The  $5^\circ$  Jet Angle

### §6.3.2 Jet With $30^\circ$ Cone Angle

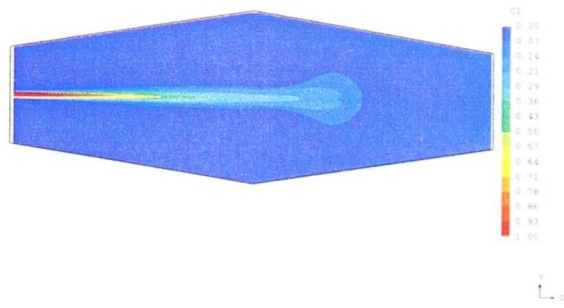
There are numerous cone jet configurations which can be studied, but due to the time constraint only two cone jet profiles have been modelled.

In this study the jet with a conical profile with a cone angle of  $30^\circ$  was modelled. The purpose has been to study what effects varying the jet cone angle made in terms of

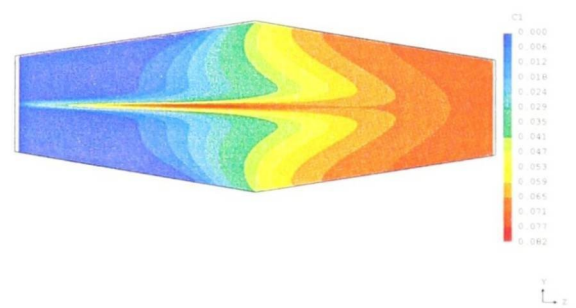
the percentage of the drug delivered and the volume of the spacer being occupied by the drug. In all the studies carried out so far the highest drug concentration within the spacer has been in the range reported in the respiratory journals.

The analysis carried out has been presented in Figure (6.3.4a-d). It can be seen from Figure (6.3.4a) that the jet of drug had entered the spacer. The jet had a very narrow profile and extended approximately 2/3 of the way inside the spacer. The jet then, began to diffuse. Once again the maximum drug concentration at this time step was formed around the nozzle or the inlet to the spacer.

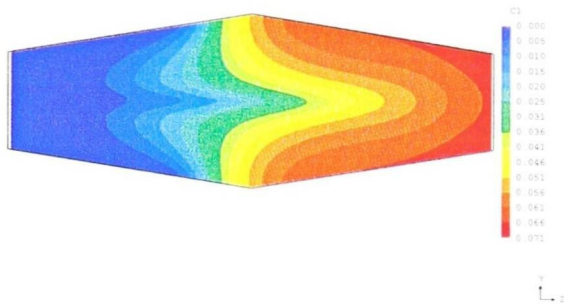
At 0.4 seconds the maximum concentration around the mouth piece was about 7.7%, however there was a higher drug concentration region just along the centreline as shown in Figure (6.3.4b). The noticeable change in this jet configuration was the considerable volume of the spacer, which was completely empty of any drug concentration, hence not serving any purpose. At time step 0.75, as shown in Figure (6.3.4c), it was observed that, the region containing the maximum drug concentration was near the mouth piece. This region was very narrow compared to the similar time steps in the previous studies. The highest drug concentration value has reduced from 8.1% to 7.1%. At the end of the cycle, time step 1.0 second the concentration of the drug delivered had reduced slightly from 7.1% to 7.0%. This maximum concentration region was still near the mouth piece and had slightly increased in volume around the centre line. This study and the previous analysis have shown that, there was no significance in terms of drug concentration from 0.75 second to the final time step, which is 1.0 second.



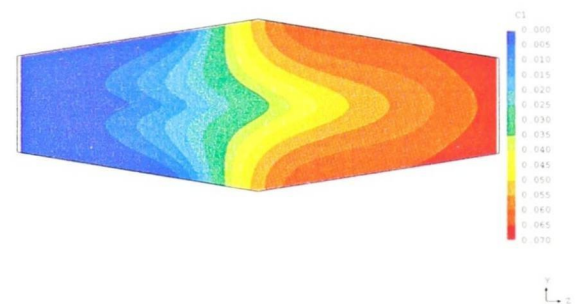
(a) Concentration Distribution 30° Jet Angle Time Step 0.05 Sec.



(b) Concentration Distribution 30° Jet Angle Time Step 0.4 Sec.



(c) Concentration Distribution 30° Jet Angle Time Step 0.75 Sec.



(d) Concentration Distribution 30° Jet Angle Time Step 1.0 Sec.

Figure 6.3.4: Diagram Showing 30° Jet Cone angle Results

### §6.3.3 19.5° deg spray Angle

The next parameter that was changed, was the jet profile at inlet to the spacer. The profile modelled was in the shape of a spray with an angle of 19.5°. In this study the spray angles ranging from 19.5° to 60° have been studied and the results have been shown graphically in Figure (6.3.5a-d). The significance of this angle was that, it caused the jet to enter the spacer parallel to the top wall of the spacer. The jet

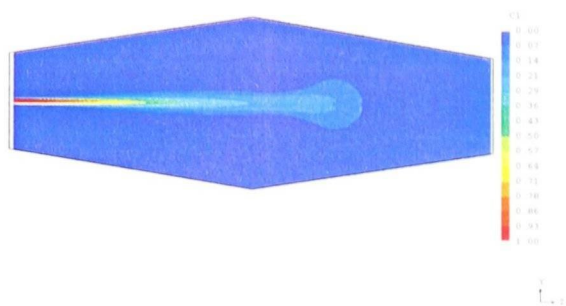
configuration used is shown in Figure (6.3.2). The result for this particular study have been analysed in detail. In order to be consistent with previous studies, the same time steps have been analysed.

At the initial time step the jet entered the spacer and extended approximately  $2/3$  of the spacers length inside the device as shown in Figure (6.3.5a-d). The jet was then observed to diffuse and adopted a shape similar to the glass balloon formed at the end of a glass blower's tube.

At time step 0.4 second majority of the drug had accumulated in the second half of the spacer and the highest concentration had accumulated in a thin layer near the mouth piece spreading upwards towards the top wall of the spacer. The highest concentration value had reduced to 7.3% as shown in Figure (6.3.5b).

At time step 0.75 seconds the highest concentration had reduced from 7.3 to 6.8%. The region with the highest concentration was seen to fill a small region near the mouth piece, and extending backwards against the top wall towards the centre line. This particular jet configuration does not appear to be as efficient in terms of drug delivery as the previous configurations already discussed. This jet configuration leaves about  $1/3$  of the spacer volume empty of any drug, once again raising the question, that is the current size the optimum size for the spacer.

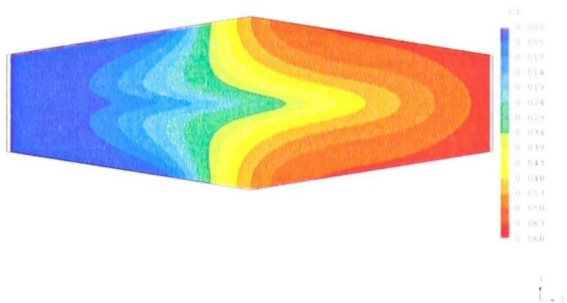
At time step 1.0 second, the highest concentration value had reduced to 6.7%. The region was concentrated more closely to the mouth piece and did not extend backwards as far as in the previous time steps for the same jet profile. Once again about  $1/3$  of the spacer volume remained empty of the drug.



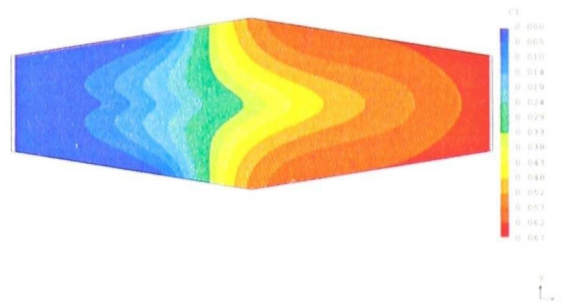
(a) Concentration Distribution 19.5° Jet Angle Time Step 0.05 Sec.



(b) Concentration Distribution 19.5° Jet Angle Time Step 0.4 Sec.



(c) Concentration Distribution 19.5° Jet Angle Time Step 0.75 Sec.



(d) Concentration Distribution 19.5° Jet Angle Time Step 1.0 Sec.

Figure 6.3.5: Diagram Showing 19.5° Spray Jet angle Results

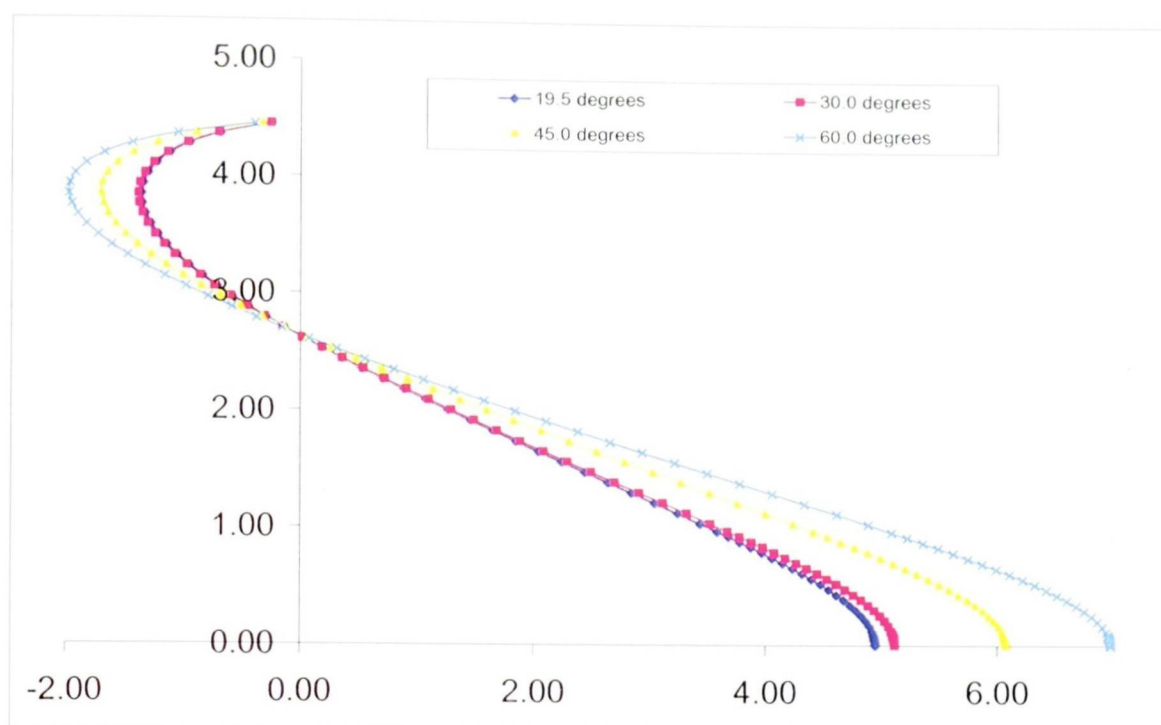


Figure 6.3.6: Comparison of Different Jet Angle Inclinations  
the values are plotted along the centerline

#### §6.4 Geometry Effects

The jet configuration studies had revealed that under certain conditions about one third of the spacer volume remained completely empty of any drug. This finding indicated, the efficiency may be improved by reducing the size of the spacer. The geometrical changes have been studied in detail and the findings are reported in the following sections: It has to be noted the original spacer would not be described here again, as this has been covered in detail in previous sections.

### §6.4.1 New Spacer Model Length, 12cm

The geometry effect was the final part of the parametric study. The aim in this section was to re-design the spacer by making a simple dimensional change, hence producing a more efficient and portable device.

The new refined spacer was modelled and the flow behaviour analysed in terms of the regions where the drug with the highest concentration accumulated. In order to magnify the geometry effects the spacer length was reduced from 24 cm to 12cm. The other dimensions such as the inlet diameter and outlet diameter of the mouth piece remained unchanged.

In the initial study the spacer length was 12 cm. The drug was injected into the spacer with the jet having a straight profile and an inlet velocity of 10 m/s. The results are shown in Figures (6.4.1a-d).

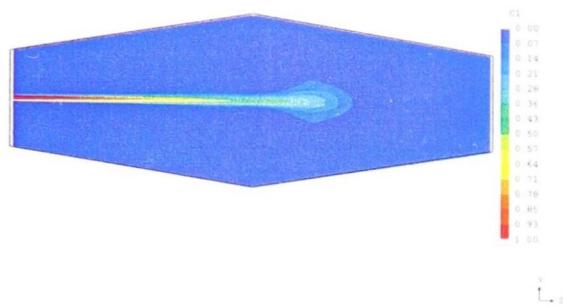
At the first time step shown in Figure(6.4.1a), the jet has entered the spacer and travelled 2/3 of the way inside the spacer. The jet then has shown to diffuse.

At time step 0.4 seconds the maximum drug concentration was 13.8% and had occupied the region around the top and bottom wall on either side of the mouth piece shown in Figure (6.4.1b). At this time step the the jet of drug had reached the end of the spacer and the trailing jet of drug had pushed the region containing the higher concentration away from the mouth piece. However the reduction in the size of the spacer accompanied by the reduction in velocity does not seem to have made any difference in terms of utilising the whole volume of the space.

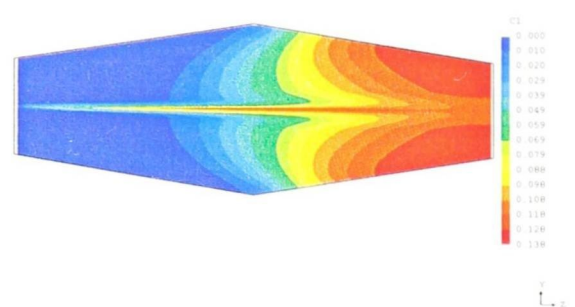
At time step 0.75 seconds the trailing jet of drug had disappeared and the regions containing the highest drug concentration had settled around the top and bottom side wall in a symmetrical manner. The maximum drug concentration, although marginally higher at 12.5% than previous studies was not a hug improvement. This

## 6.4. Geometry Effects

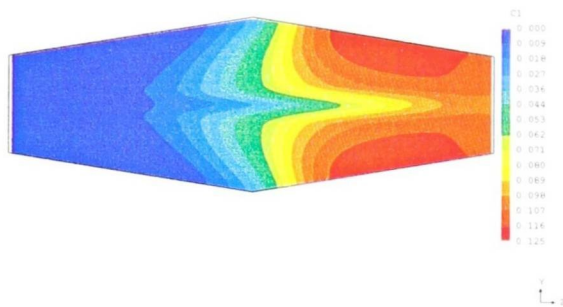
value is shown to reduce slightly for the 1.0 second time step as shown in Figure (6.4.1d).



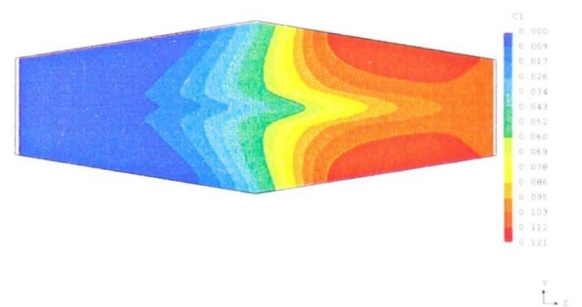
(a) Concentration Distribution Straight  
Jet Velocity 10m/s Time Step 0.05 Sec.



(b) Concentration Distribution Straight  
Jet Velocity 10m/s Time Step 0.4 Sec.



(c) Concentration Distribution Straight  
Jet Velocity 10m/s Time Step 0.75 Sec.



(d) Concentration Distribution Straight Jet Ve-  
locity 10m/s Time Step 1.0 Sec.

Figure 6.4.1: Jet Inlet Velocities At 10 m/s For The Spacer Length 12cm

The velocity was then increased to 30 m/s and the results for the same four time steps, shown in Figures (6.4.2a-d). The immediate noticeable feature was that the jet had travelled a long distance inside the spacer and due to highly turbulent nature of the flow, the jet had diffused at a much faster rate.

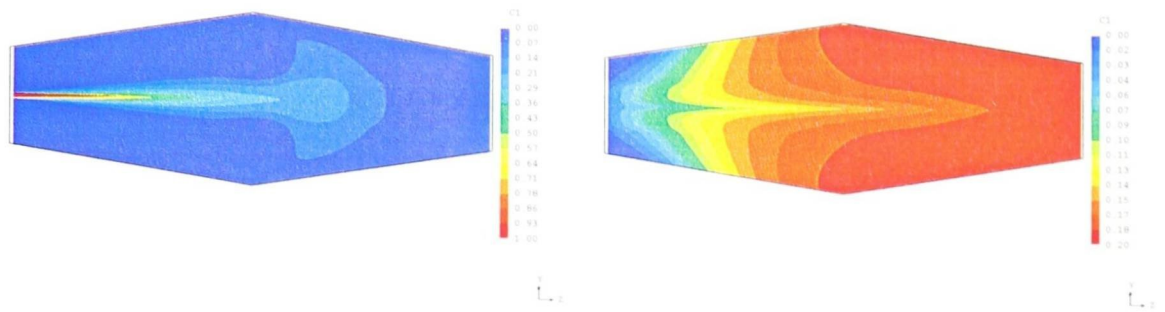
At 0.4 seconds as shown in Figure (6.4.2b), the highest drug concentration had risen

to 20%. This region was quite large in terms of volume compared to the previous cases studied. It was also noticeable that there was hardly any empty volume free of drug in this modified spacer. This increase in the drug concentration level, was almost twice higher than any figure reported in the literature. Furthermore the highest concentration had occurred around the mouth piece.

At 0.75 seconds the concentration level has reduced slightly to 19%, but the highest concentration region was still around the mouth piece as shown in Figure (6.4.2c).

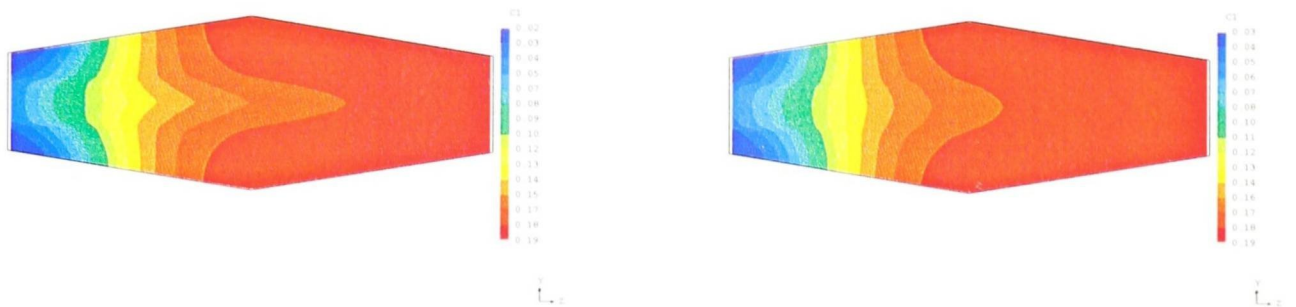
Finally at 1.0 second the only noticeable difference observed shown in Figure (6.4.2d) was that the, highest concentration level reduced slightly and the region became more uniform in terms of drug concentration distribution.

## 6.4. Geometry Effects



(a) Concentration Distribution Straight  
Jet Velocity 30m/s Time Step 0.05 Sec.

(b) Concentration Distribution Straight  
Jet Velocity 30m/s Time Step 0.4 Sec.



(c) Concentration Distribution Straight  
Jet Velocity 30m/s Time Step 0.75 Sec.

(d) Concentration Distribution Straight Jet Ve-  
locity 30m/s Time Step 1.0 Sec.

Figure 6.4.2: Inlet Velocities 30m/s Spacer Length 12cm

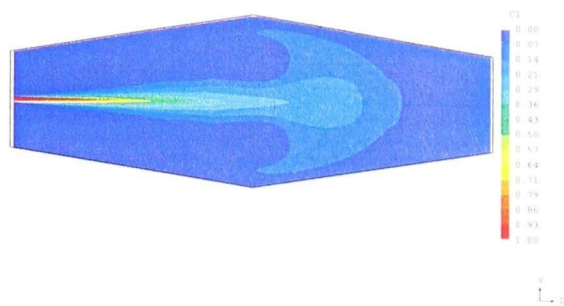
A new study was undertaken, with the jet inlet velocity set at 40 m/s, shown in Figures (6.4.3a-d). It was observed that at time step 0.05 second the jet had entered the spacer and travelled a long distance inside the device. The flow was highly turbulent, hence explaining the rapid diffusion of the jet as shown in Figure (6.4.3a).

At 0.4 seconds shown in Figure (6.4.3b), that the majority of the spacer was filled with drug containing the highest concentration. This concentration was 24% of the original concentration being injected into the spacer. It can also be seen that the jet

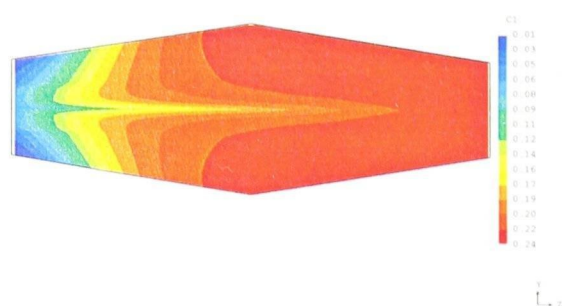
had completely detached itself from the nozzle as expected, and the trailing jet is diffusing and mixing with the bulk of the drug in the spacer.

At 0.75 second the highest concentration level had reduced to 23% ,shown in Figure (6.4.3c). It was also clear from the above figure that, the trailing jet had almost completely diffused within the spacer. The other noticeable feature was the full utilisation of the spacer volume.

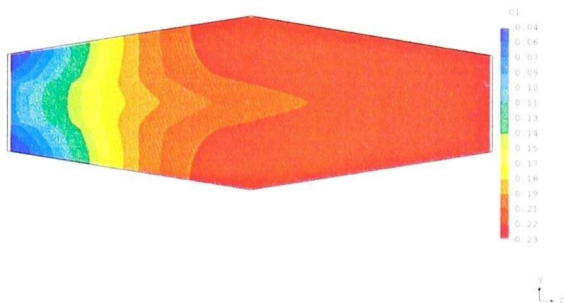
At 1.0 second there were no major changes in the flow pattern, except for a slight reduction in the level of drug concentration. One major feature of this particular case was that, the volume of the spacer containing the highest drug concentration was immediately accessible to the patient, as it had filled entirely 2/3 of the spacer volume, as shown in Figure (6.4.3d).



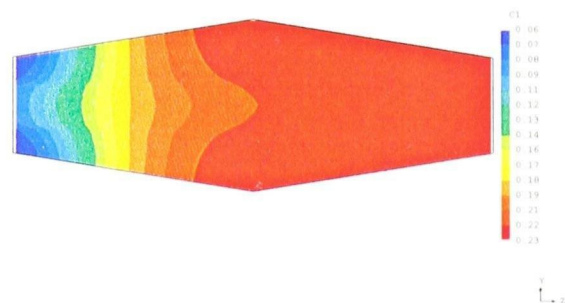
(a) Concentration Distribution Straight  
Jet Velocity 40m/s Time Step 0.05 Sec.



(b) Concentration Distribution Straight  
Jet Velocity 40m/s Time Step 0.4 Sec.



(c) Concentration Distribution Straight  
Jet Velocity 40m/s Time Step 0.75 Sec.



(d) Concentration Distribution Straight Jet Velocity 40m/s Time Step 1.0 Sec.

Figure 6.4.3: Inlet Velocities 40m/s Spacer Length 12cm

The analysis of the above studies have shown that, the most efficient spacer in terms of drug delivery, would have a straight jet profile and an inlet velocity of 40 m/s. This combination has shown to deliver approximately 23% of the drug to the mouth piece.

### §6.4.2 New Spacer Model Length, 6cm

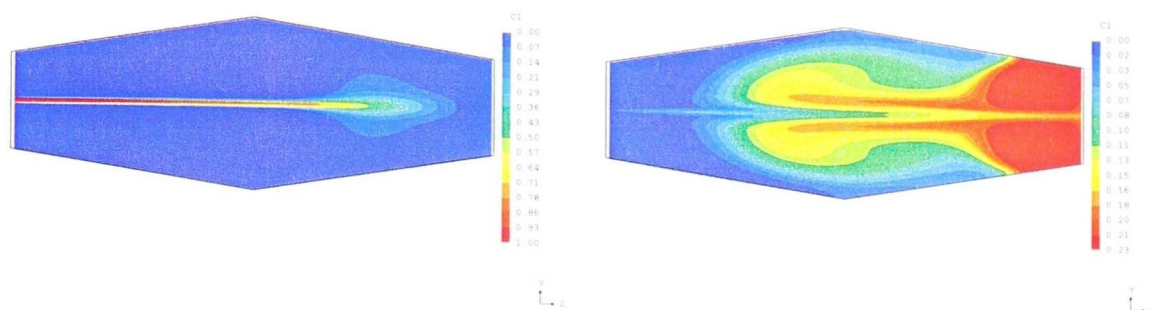
In order to investigate the geometry effects further the spacer length was reduced to 6 cm and the same range of jet inlet velocities were analysed.

Initially the straight jet with an inlet velocity of 10 m/s was modelled, Figure (6.4.4a). The jet had entered the spacer and was confined to a very narrow profile, with a very wide head. This appearance was created as a result of a very rapid diffusion. It was also observed from the above figure that the jet of drug reached the mouth piece very quickly.

At 0.4 seconds the maximum drug concentration was 23% and occupied a region on either side of the centre line around the mouth piece. The trailing part of the jet had then reached the mouth piece as shown in Figure (6.4.4b). This had created two separate recirculation regions.

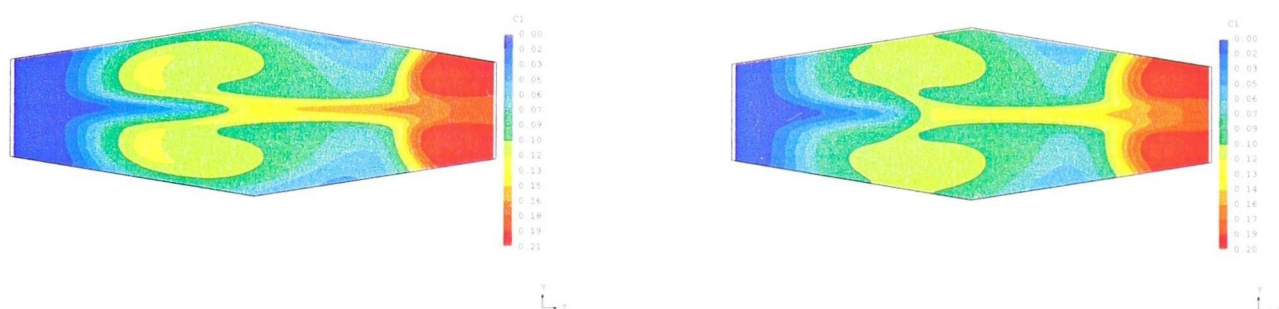
At time step 0.75 the highest concentration level had reduced to 21% shown in Figure (6.4.4c). At this time step there were two separate regions where the drug was seen to be mixing quite vigorously.

At the final time step, the two regions containing the drugs of varying concentration, appeared to have a more uniform concentration. The surprising feature of this case was the volume of spacer which had remained empty of any drug as shown in Figure (6.4.4d). It was also observed that the concentration level had followed the usual trend and had reduced by 1% for the final time step.



(a) Concentration Distribution Straight  
Jet Velocity 10m/s Time Step 0.05 Sec.

(b) Concentration Distribution Straight  
Jet Velocity 10m/s Time Step 0.4 Sec.



(c) Concentration Distribution Straight  
Jet Velocity 10m/s Time Step 0.75 Sec.

(d) Concentration Distribution Straight Jet Ve-  
locity 10m/s Time Step 1.0 Sec.

Figure 6.4.4: Inlet Velocities 10m/s Spacer Length 6cm

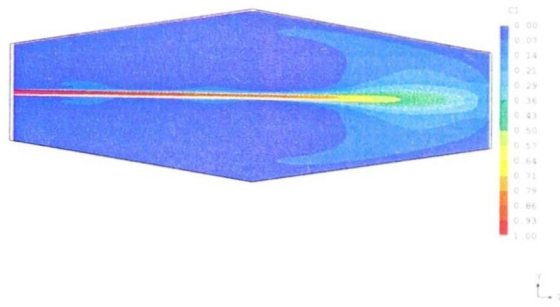
The next case studied was the that of the 30 m/s jet inlet velocity. It was observed from Figure (6.4.5a) that the jet of drug had entered the spacer and after reaching the mouth piece, it had begun recirculating backwards towards the middle of the spacer. The main body of the jet was shown at this time step to have a very narrow profile up to the head of the jet.

At 0.4 seconds the maximum drug concentration was shown in Figure (6.4.4c) to have accumulated near the mouth piece, having a maximum concentration of 33%.

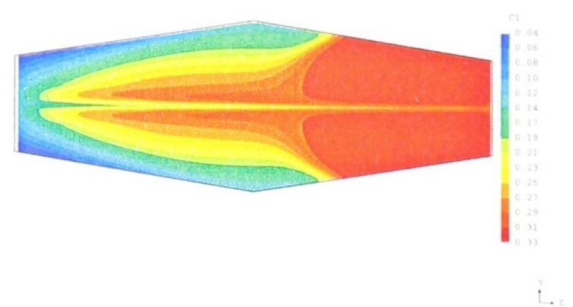
This was by far the highest value achieved.

At 0.75 seconds two separate regions containing varying drug concentrations were formed. The region at the inlet had the lowest drug concentration and the region at the mouth piece had been occupied by the drug containing the highest concentration level as shown in Figure (6.4.4c).

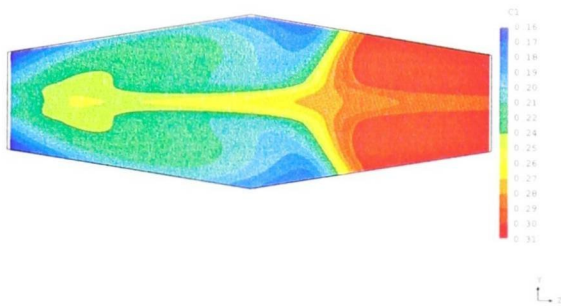
At time step 1.0 second there were not any changes in the drug concentration levels, as shown in Figure (6.4.5d). This particular analysis had proved varying the parameters, such as geometry and inlet velocity would have a profound effect on the drug concentration levels and regions where the highest concentrations were accumulated.



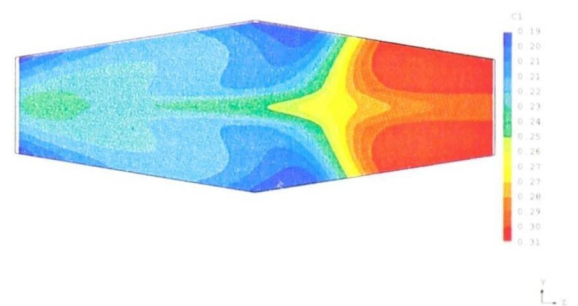
(a) Concentration Distribution Straight  
Jet Velocity 30m/s Time Step 0.05 Sec.



(b) Concentration Distribution Straight  
Jet Velocity 30m/s Time Step 0.4 Sec.



(c) Concentration Distribution Straight  
Jet Velocity 30m/s Time Step 0.75 Sec.



(d) Concentration Distribution Straight Jet Ve-  
locity 30m/s Time Step 1.0 Sec.

Figure 6.4.5: Inlet Velocities 30m/s Spacer Length 6cm

The final case studied was that of the jet inlet velocity of 40 m/s. This case was the final analysis for the current spacer model and would prove if the parametric studies have optimised the performance of the current spacer design.

At 0.05 seconds the drug was injected into the spacer. It was shown in Figure (6.4.6a) that the jet of drug had reached the mouth piece of the spacer, while the highest drug concentration was still at the inlet of the spacer.

At 0.4 second the values shown in Figure (6.4.6b) had revealed a disappointing picture. The highest concentration level recorded was only about 9.5%. Furthermore the high concentration region was situated away from the mouth piece, this in itself was a situation which needs to be avoided.

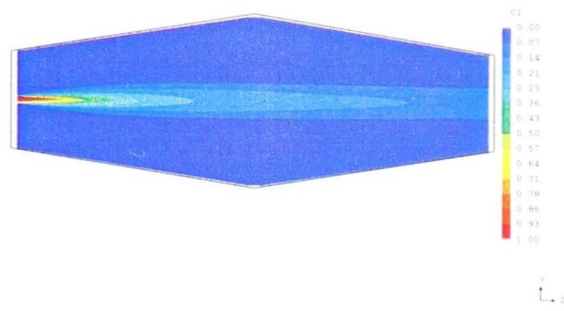
At time step 0.75 the highest drug concentration had reduced to 8.7%. It was clear from Figure (6.4.6c) that, the region with the highest drug concentration had moved to the front of the spacer, just near the mouth piece.

At time step 1.0 seconds there was a slight reduction in the drug concentration levels, as shown in Figure (6.4.6d), but otherwise no other significant changes were observed.

### §6.4.3 Summary of The Modified Volumatic<sup>TM</sup> Designs

In this section a summary of the findings for the two modified models of the spacers (i.e. the 12 cm and 6 cm) has been presented in Figures (6.4.6a-f). Initially the results are shown for time step 0.4 second, as at this time step the maximum drug concentration was present. It can be seen from Figure (6.4.6a), that the maximum drug concentration at time step 0.4 seconds for the 12 cm length spacer was 23%. It can be seen from the same time step when the spacer length was reduced, the maximum drug concentration level was 9.5% as shown in Figure (6.4.6b). It is clear from the current analysis the spacer which was 12 cm long in length was the more efficient device.

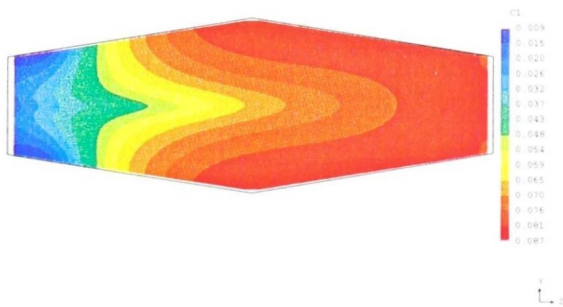
The next set of results shown in Figures (6.4.6c) indicated that at 30 m/s the more efficient design was that of the 6 cm long spacer delivering a maximum of 33% of the drug, where as for a similar inlet velocity, the 12 cm spacer model had only delivered 20% of the drug to the mouth piece as shown in Figure (6.4.6d).



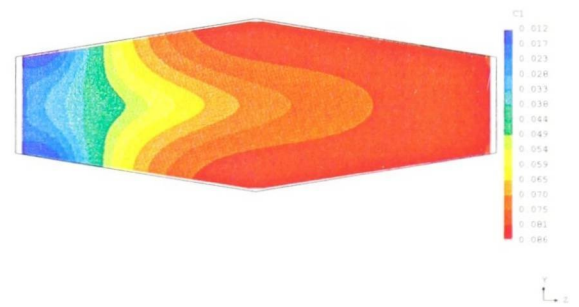
(a) Concentration Distribution Straight Jet Velocity 40m/s Time Step 0.05 Sec.



(b) Concentration Distribution Straight Jet Velocity 40m/s Time Step 0.4 Sec.



(c) Concentration Distribution Straight Jet Velocity 40m/s Time Step 0.75 Sec.

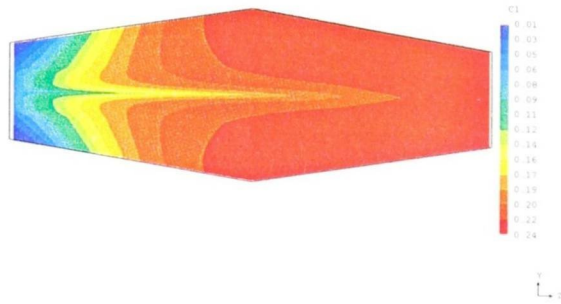


(d) Concentration Distribution Straight Jet Velocity 40m/s Time Step 1.0 Sec.

Figure 6.4.6: Inlet Velocities 40m/s Spacer Length 6cm

Finally the results for the 10 m/s inlet velocity were analysed. In the first instance the 6 cm spacer was studied. It has been shown that for this inlet velocity the spacer had delivered drug concentration of 23% to the mouth piece. For the similar set up the 12 cm spacer had managed to deliver only 13.8% of the drug, as shown in Figures(6.4.6e-f).

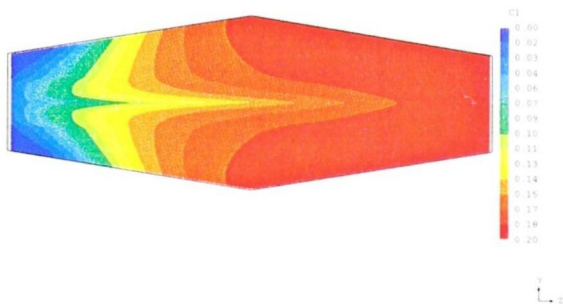
## 6.4. Geometry Effects



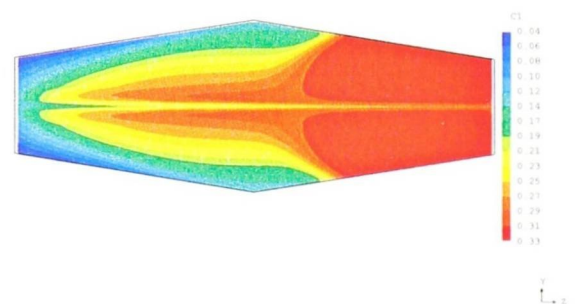
(a) Concentration Distribution Straight Jet Velocity 40m/s Length 12cm Time Step 0.4 Sec.



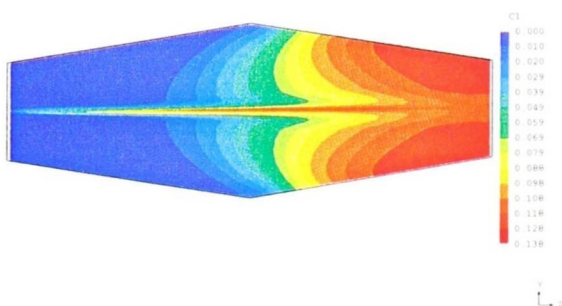
(b) Concentration Distribution Straight Jet Velocity 40m/s Length 6cm Time Step 0.4 Sec.



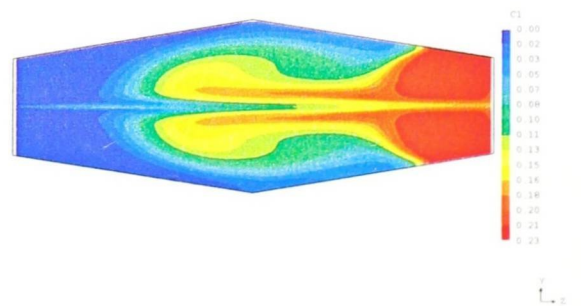
(c) Concentration Distribution Straight Jet Velocity 30m/s Length 12cm Time Step 0.4 Sec.



(d) Concentration Distribution Straight Jet Velocity 30m/s Length 6cm Time Step 0.4 Sec.



(e) Concentration Distribution Straight Jet Velocity 10m/s Length 12cm Time Step 0.4 Sec.



(f) Concentration Distribution Straight Jet Velocity 10m/s Length 6cm Time Step 0.4 Sec.

Figure 6.4.7: Concentration Distribution For Different Spacer Lengths

It was important to establish what the final drug concentrations were at the 1.0 second time step for all the models studied. The results have been presented in Figures (6.4.7a-f).

The initial study shown in Figures (6.4.7a-b) has shown that for the jet inlet velocity of 40 m/s the 6 cm spacer has only managed to deliver 8.6% of the drug, where as for the same inlet condition the 12 cm spacer has managed to deliver 24% of the drug.

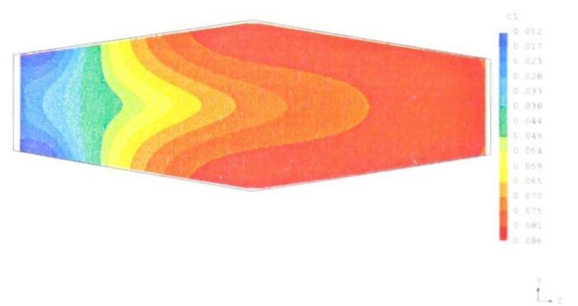
The next analysis was for the time step at 1.0 second, with the jet inlet velocity set at 30 m/s. The results are shown in Figures (6.4.7c-d). It is clear from the results that, the 6 cm spacer has delivered 31% of the drug at 1.0 second, where as for the same jet inlet velocity the 12 cm spacer can only deliver 19% of the drug to the mouth piece.

In the final analysis the flow patterns for the inlet velocity set at 10 m/s were compared. The results are shown in Figures (6.4.7e- f). It can be seen that the 12 cm spacer has delivered 12.5%. The similar jet inlet velocity has resulted in 23% of the drug being delivered for the 6 cm spacer.

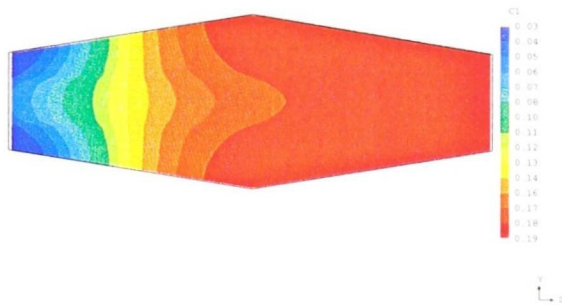
## 6.4. Geometry Effects



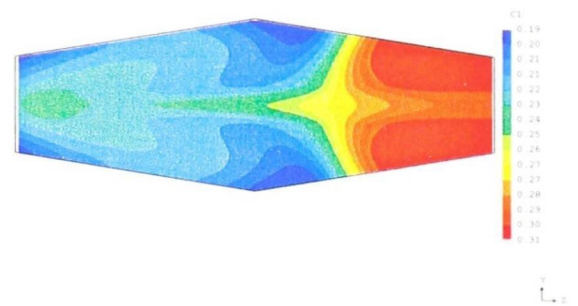
(a) Concentration Distribution Straight Jet Velocity 40m/s 12cm Length Time Step 1.0 Sec.



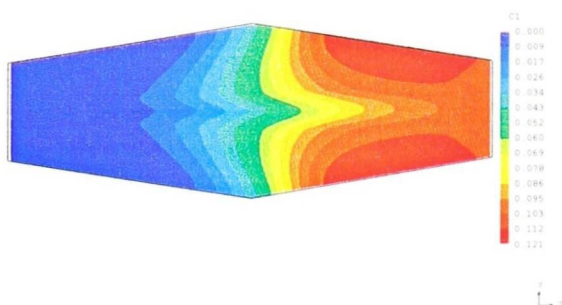
(b) Concentration Distribution Straight Jet Velocity 40m/s Length 6cm Time Step 1.0 Sec.



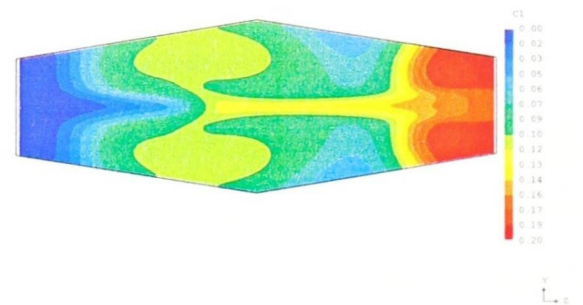
(c) Concentration Distribution Straight Jet Velocity 30m/s 12cm Length Time Step 1.0 Sec.



(d) Concentration Distribution Straight Jet Velocity 30m/s 6 cm Length Time Step 1.0 Sec.



(e) Concentration Distribution Straight Jet Velocity 10m/s 12cm Length Time Step 1.0 Sec.



(f) Concentration Distribution Straight Jet Velocity 10m/s 6cm Length Time Step 1.0 Sec.

Figure 6.4.8: Concentration Distribution For Different Spacer Lengths

## 6.5. The Straight Tube Design

---

At time step 1.0 second the maximum drug concentration level in all the test cases has reduced. The smallest reduction in drug concentration was observed in the 6 cm Volumatic<sup>TM</sup> spacer. This model carried 31% of the drug at the final time step.

### §6.4.4 Conclusions

The analysis carried out have shown that, for each geometrical change there is an optimum inlet velocity value for which the spacer can deliver the highest drug concentration. It was clear from the analysis, that the highest drug concentration was delivered, when the spacer length was 6 cm and the inlet velocity was 30 m/s. This study had shown the efficiency of the device was increased by a further 21% under these conditions.

It can also be concluded from the studies carried out that the inlet velocity of 40 m/s generally did not deliver the highest drug concentration for the standard spacer length, the 12cm long and the 6 cm long spacer.

The next step forward was to study different geometries and carry out a similar study for each geometry, until an acceptable level of drug delivery was achieved.

### §6.5 The Straight Tube Design

The lack of literature available on the design of the current spacer device, and the increase in use of tube like spacers or aero chambers, together with the confirmation from the previous section that there had to be an optimum geometry for the spacer device which has led to the following investigations.

The current tube design or aero chamber was investigated and after a series of analysis, it was concluded that the, device could be made more efficient by making some

## 6.5. The Straight Tube Design

minor adjustments. The other reason for choosing this device, was the tube like shape, which makes it easily portable. The dimensional measurements were made from a current aero chamber and a prototype was made.

The new Tube like spacer had a length of 10 cm and was made of Perspex material. The two holes were drilled one at the top and the other at the bottom of the spacer at a distance of 2 cm from the inlet. The holes drilled cause a change in pressure, this change in pressure keeps the jet narrow and directs it towards the mouth piece. A simple spring and weir arrangement ensured that the drug was injected straight into the spacer rather than hitting the lower wall at inlet. The comparison of the two spacers is shown in Figure(6.5.1).

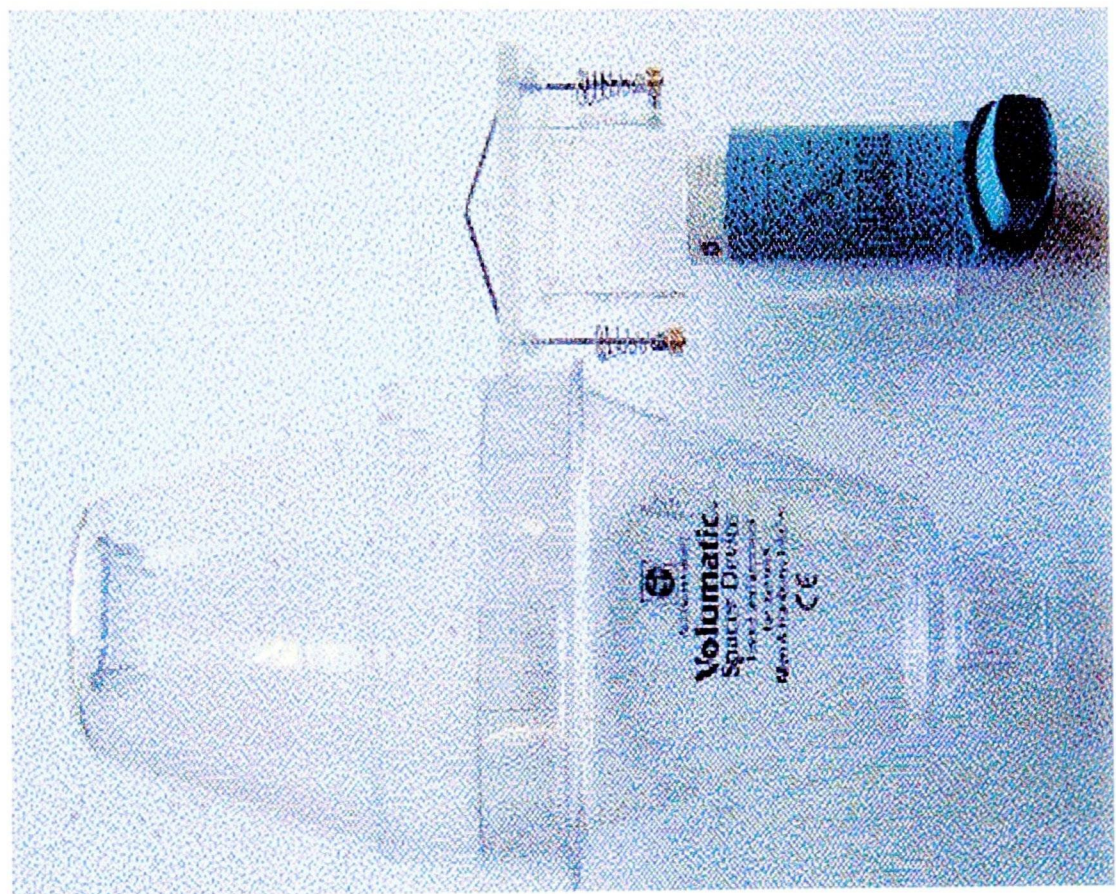


Figure 6.5.1: Comparison of the Two Spacers

At time step 0.05 seconds shown in Figure(6.5.2a) it was observed that the drug had been injected into the spacer. It was noticed at a glance that the flow pattern

## 6.5. The Straight Tube Design

---

was completely different from any of the previous studies. The two small holes on either side of the spacer caused a change in pressure as the drug was injected into the spacer. The change in pressure caused a recirculation region at the location of each hole. The jet of drug was then forced to the mouth piece end of the spacer, Figure (6.5.2a). The highest drug concentration is accumulated at the top and bottom corner of the spacer.

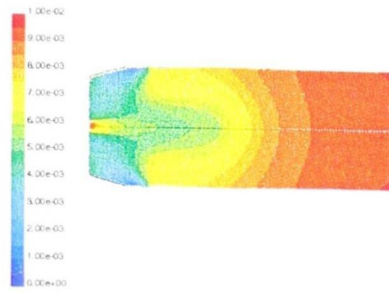
At the 0.4 second time step the detached jet had driven the drug forward within the spacer causing the highest drug concentration to remain at the mouth piece end of the spacer and fill that region completely, Figure (6.5.2b). The maximum drug concentration at this time step was 73%. This was by far the highest delivered drug concentration.

The next snap shot analysed was at 0.75 seconds. There was clear evidence of drug mixing as the region marked yellow in the spacer had reduced in volume and at the mouth piece end the region with the highest concentration level marked red had increased in volume. This region had a concentration of 71% as shown in Figure (6.5.2c).

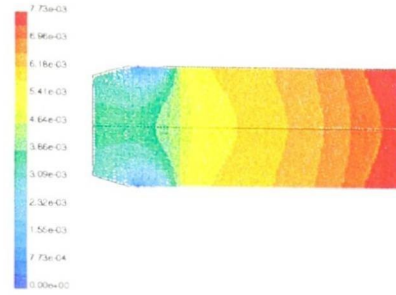
Finally at time step 1.0 second, shown in Figure (6.5.2d), that there had been no change in the level of drug concentration. This device had by far has out preformed any existing commercially available spacer in the market according to the available literature. In concluding this part of the study the advantages of the tube design over the current spacer design can be stated as follow:

- It has increased the efficiency from approximately 10% to 71%
- The new tube design is only about 10cm long compared to 24cm and is less bulky, so it can fit in a persons pocket as shown in Figure(6.5.1).
- The design is so simple, that the manufacturing costs would be reduced

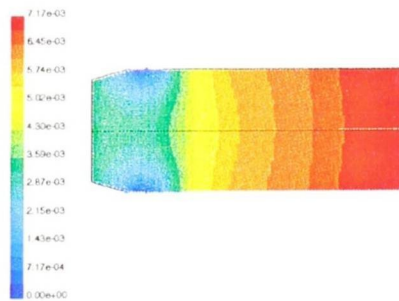
## 6.5. The Straight Tube Design



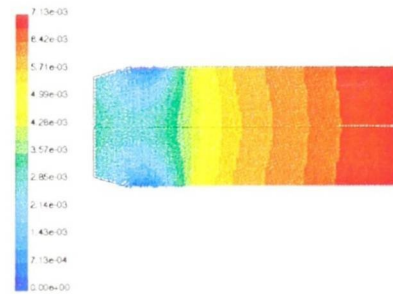
(a) Drug Distribution  
Straight Jet Velocity 40m/s  
Length 10cm, Aero Chamber  
Design Time Step 0.05  
Sec.



(b) Drug Distribution  
Straight Jet Velocity 40m/s  
Length 10cm Aero Chamber  
Design Time Step 0.4 Sec.



(c) Drug Distribution  
Straight Jet Velocity 40m/s  
Length 10cm Aero Chamber  
Time Step 0.75 Sec.



(d) Drug Distribution  
Straight Jet Velocity 40m/s  
Length 10cm Aero Chamber  
Time Step 1.0 Sec.

Figure 6.5.2: Drug Distribution For The New Aero Chamber Design

§6.5.1 Conclusions of the Parametric study

In conclusion to the parametric study it can be stated that the spacer efficiency in terms of drug delivery increases when the length of the spacer was reduced from 0.24m to 0.06m. This together with reduction of the inlet velocity from 40m/s to 30m/s had meant that the maximum drug concentration delivered had increased from 6.5% to 31%. This improvement was the maximum achievable for the current Volumatic<sup>TM</sup> design.

The best improvement was made when the design was changed to a straight tube (Aero Chamber) with two small holes opposite each other. The region containing the maximum drug concentration had a maximum value of 71%. The full set of results are tabulated in Table(6.6.1) and results are discussed in terms of percentage of the drug delivered.

Original Shape	Jet Type	Efficiency %	Velocity m/s
Length 0.24m	Straight	6.5	40
Length 0.24m	5 Deg. Cone Angle	9.4	40
Length 0.24m	30 Deg. Cone	7.7	40
Length 0.24m	19.5 Deg. Spray	9.3	40
Length 0.12m	Straight	12.1	10
Length 0.12m	Straight	19	30
Length 0.12m	Straight	23	40
Length 0.06m	Straight	20	10
Length 0.06m	Straight	30	30
Length 0.06m	Straight	9.5	40
Tube 0.10m	Straight	71	40

Table(6.6.1) Summary of Parametric Studies

### §6.6 Experimental Results

The experimental study has become a major component of any CFD analysis. In some cases the experimental results published in the literature are used to validate the CFD research. However in novel studies there is often little or no published experimental results for comparison or validation purposes.

The lack of experimental results in this novel research, meant that experiments and experimental equipment had to be designed or modified, in order to provide validation for the CFD results. For this reason the experimental validation was divided into two categories as follow:

- LDA measurements
- High speed photography

#### §6.6.1 Validation of CFD Results Against LDA

In the initial CFD study air was used to get a better understanding of the flow behaviour within the Volumatic<sup>TM</sup> spacer. The standard was to model the current commercially available device and provide useful information for industry. The CFD results were then compared to the LDA measurements taken along the centre line, using a commercially available pMDI. The results provided a good approximation of the jet inlet velocity. The LDA measurements also helped to test the capability of the measuring equipment and helped to eliminate any potential problems. The experimental study also increased the confidence in the modelling approach adopted for this study. The comparison of the LDA measurements against CFD results is shown in Figure(6.6.1) and it can be seen despite differences in the properties of drug and air the flow measurements display a similar trend and the values are closely

## 6.6. Experimental Results

matched.

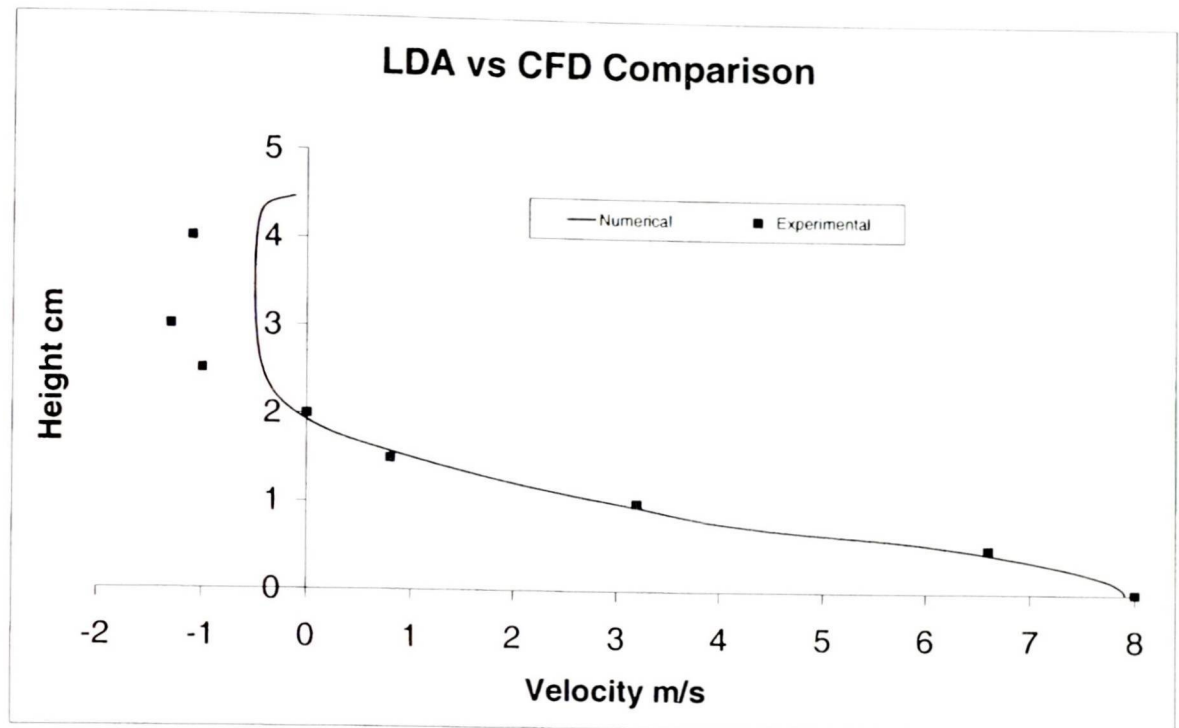


Figure 6.6.1: CFD Validation Against LDA Results At Distance 12cm from Inlet From Center Line In Positive Y Direction

The standard spacer which has a length of 24 cm was chosen for the validation study. The convention used for making the measurements is shown in Table(6.2).

Directory Listing	Y P(y value in mm)-positive to datum X(x value in mm) all positive from datum
File listing	X(x value in mm) app positive from Datum

Table(6.2) Notation Used in Measuring Data

Measurement attempts along the plane YP10 (10mm above the centre line in the positive Y direction) indicated that very few particles were present to be recorded

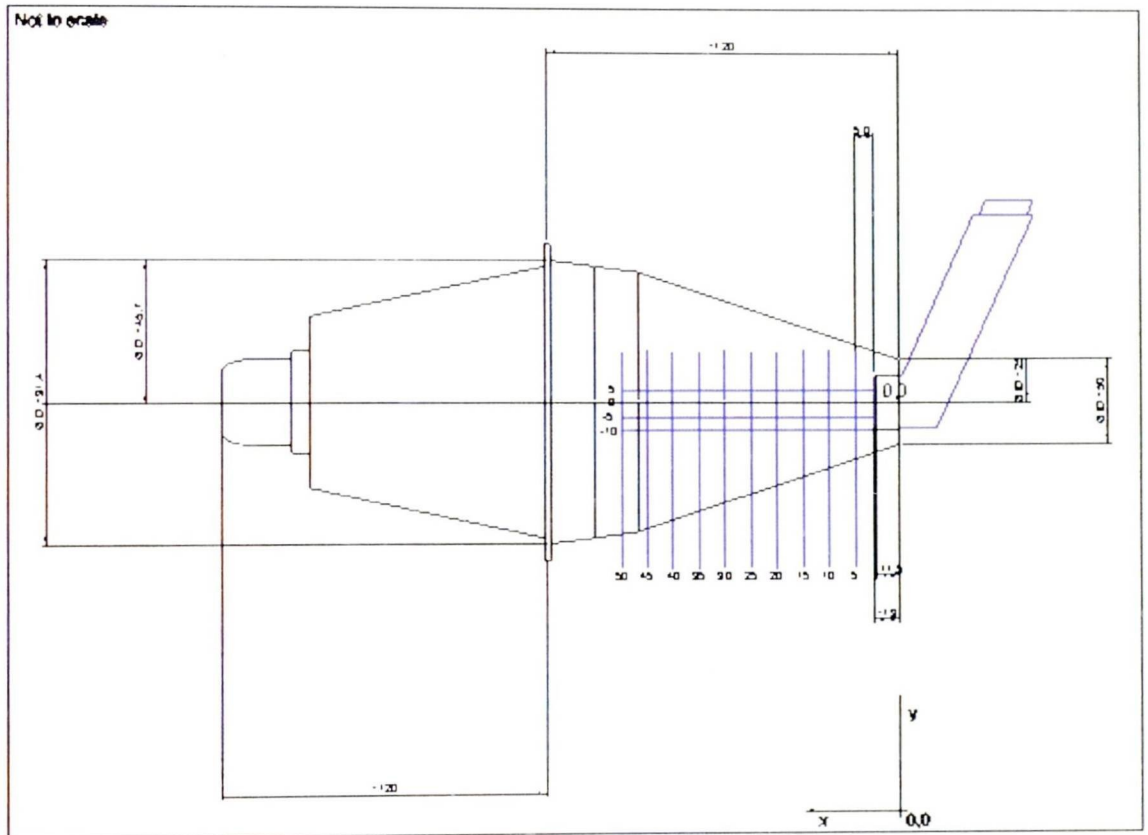


Figure 6.6.2: Measurement Grid Used In the Study

## 6.6. Experimental Results

---

as a useful set of velocity data without an excessive number of canisters. The sets of measurements for the positive YP5 plane also indicated a reduction in particle numbers and thus a very low data rate. For this plane, the number of validated Doppler events was limited to 5000 to ensure that the entire measurement grid could be completed. The repeatability of experiments performed at the same grid location was found to be generally within  $\pm 5\%$  for the average recorded velocities in the bulk flow regions during the injection event. All instantaneous velocity distributions were within 3 standard deviation of the mean value over the injection event. At each grid location, the mean velocity and turbulence intensity after 25,000 validated Doppler events was recorded. It should however be noted that these results are recorded as a means by which the experiment can be verified during its course and the values given are based upon injection and inter-injection measurements. The velocity distributions were skewed by returning particles deflected from the far, opposite wall and particles suspended between shots. These were indicated with regions of very high turbulence intensity. The standard spacer which had a length of 24 cm was chosen for the validation exercise. The locations are shown in Figure(6.6.2). The CFD verse LDA results for the three locations defined in Figure (6.6.2) have been plotted in Figures(6.6.3-6.6.6). A similar process was carried out, for the tube design but in this instance, due to lack of time and resources measurements were only taken at  $y=5$  (5mm above the centerline in positive Y direction) planes, the results are shown in Figure(6.6.7).

The CFD and experimental results shown in Figure(6.6.3) have been taken along the centreline at location  $Y=0$ . The results indicate the velocity value has reduced from 40 m/s to 20 m/s in only a distance of 5 mm from the nozzle. The velocity is then shown to decrease as the distance from the nozzle is increased. This has been mirrored by the CFD study and is the outcome expected. The velocity values estimated by CFD are slightly higher than those measure using LDA, this is was contributed to the fact that, in our CFD simulations the particles were free from any attachment to each other.

## 6.6. Experimental Results

---

The results presented in Figure (6.6.4) have measured at location YM10. This location is 10 mm below the centre line of the Volumatic<sup>TM</sup> spacer. It can be seen that the maximum velocity has occurred at a distance of 30 mm from the nozzle. The velocity value at this location was approximately 9 m/s. The reason for this phenomenon can be explained by the following suggestion: the particles are colliding with the side wall of the spacer and are carried along by the faster moving particles above them.

At the location YM5 shown in Figure (6.6.5), this is a distance of 5 mm below the centre line, the particle velocities have shown an increase from approximately 12 m/s to about 18 m/s. This fluctuation is noticed over a distance of 30 mm where the turbulence is quite strong as indicated by the contours plot earlier in the chapter. At the 40 mm mark the velocity value has decreased to approximately 10 m/s. This contributed to the decay of turbulence and the general propellant decay.

It can be seen from Figure (6.6.6) the velocity measurements recorded indicate a reverse flow region at a distance of 10 mm from the nozzle. The velocity has then shown to increase, up to the distance of 35 mm from the nozzle. The velocity magnitude recorded here are only about 1.4 m/s at the highest value. Once again the CFD and experimental studies show very close correlation.

Finally the Aero Chamber design was investigated, as shown in Figure (6.6.7). Due to the lack of time and drug only one location was chosen to take measurements from. At location Y=5, i.e just 5 mm below the centre line. It can be seen from the data plotted, that there is evidence of reverse flow up to about 7 mm from the nozzle. This was expected as the two holes drilled on either side of the chamber, were creating a change in pressure and two large recirculation regions. The comparison for between Figures (6.6.6) and Figure (6.6.7) indicate that in both models the measured velocities are of the same order.

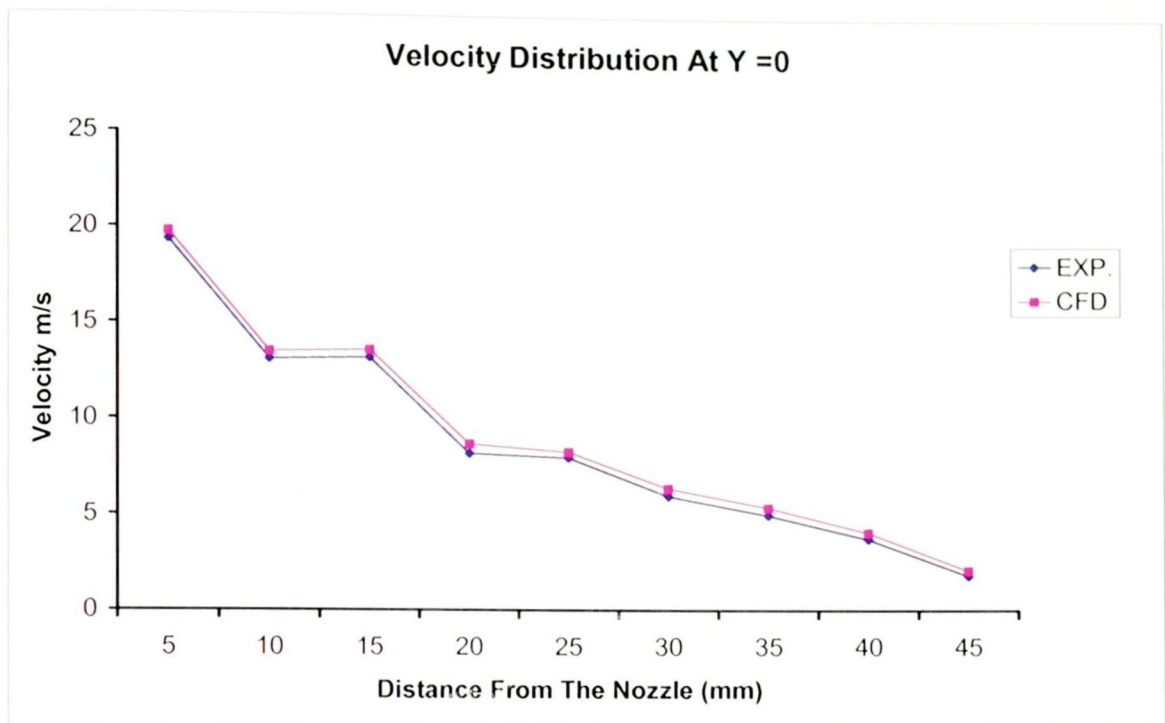


Figure 6.6.3: LDA VS CFD Measurements For The Volumatic<sup>TM</sup>

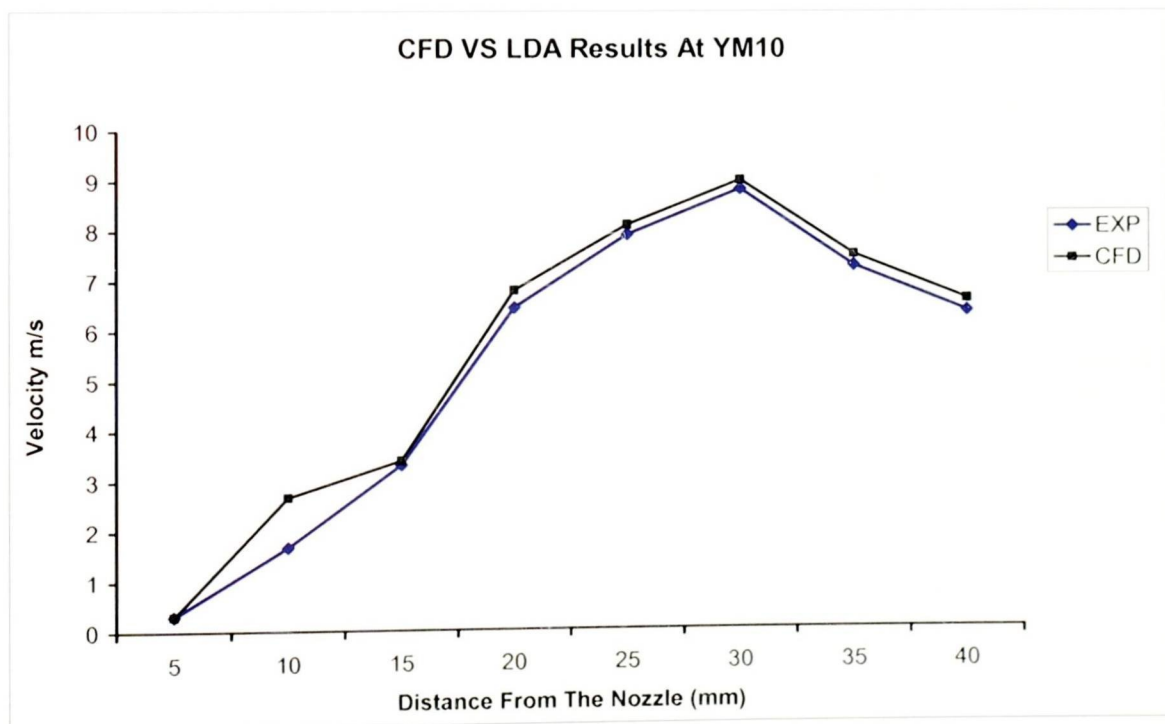


Figure 6.6.4: LDA VS CFD Measurements For The Volumatic<sup>TM</sup>

## 6.6. Experimental Results

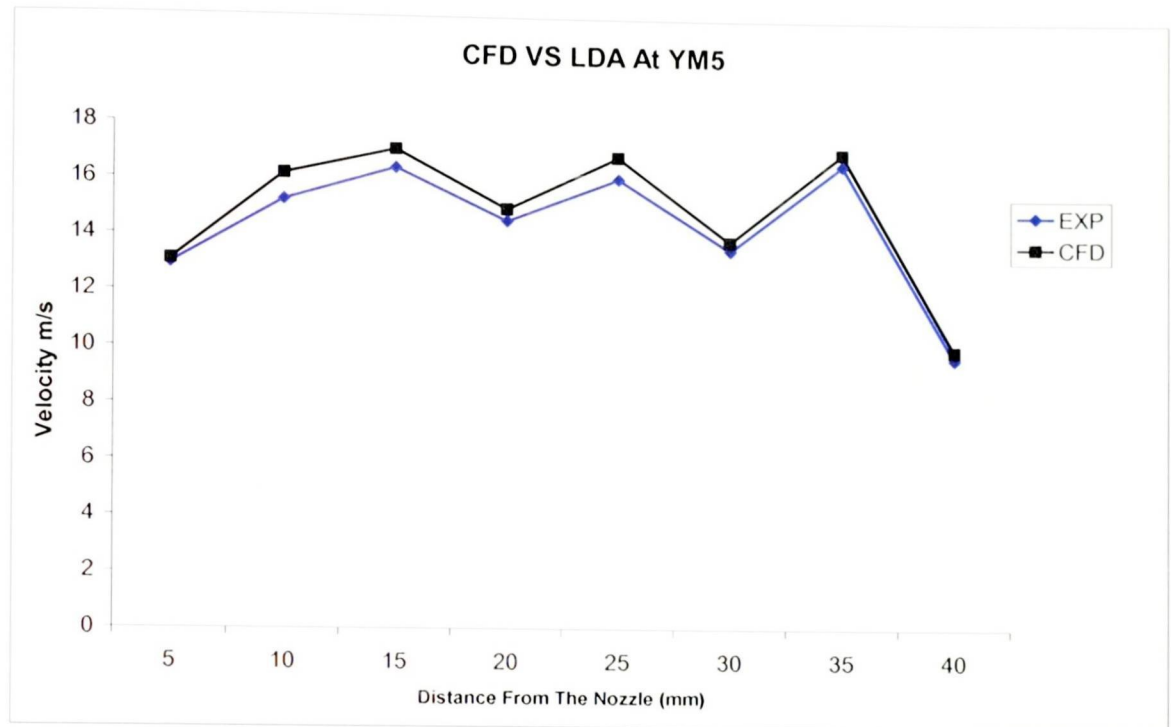


Figure 6.6.5: LDA VS CFD Measurements For The Volumatic<sup>TM</sup>

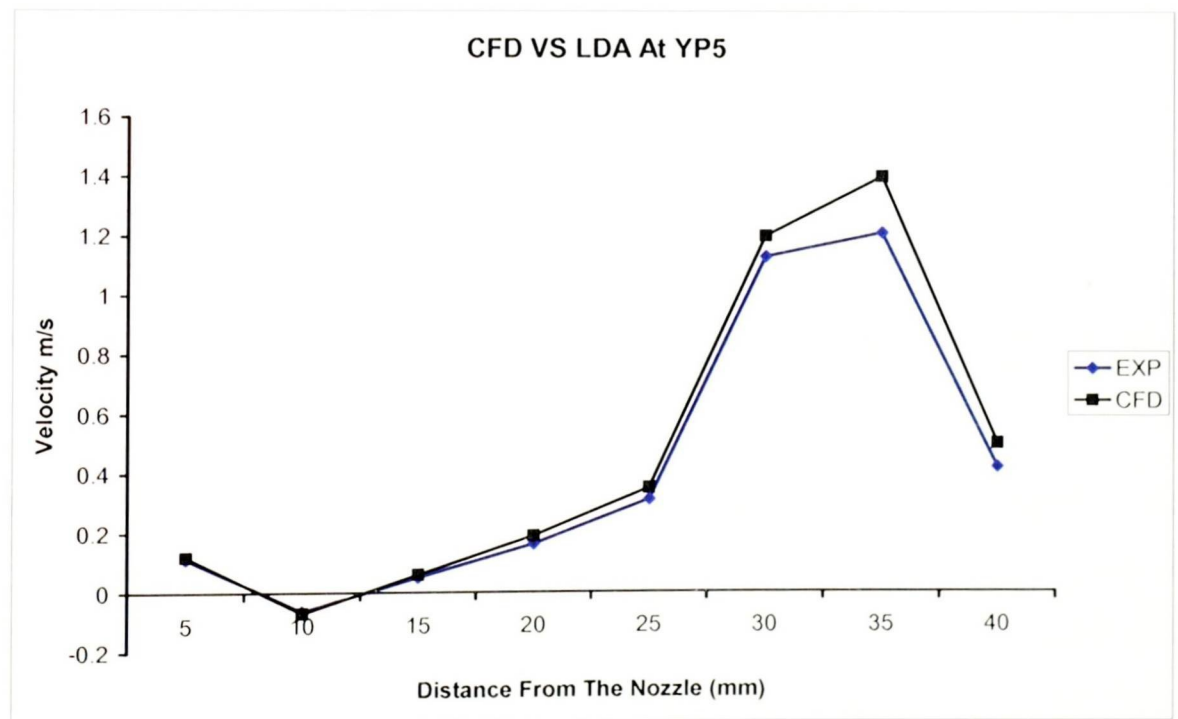


Figure 6.6.6: LDA VS CFD Measurements For The Volumatic<sup>TM</sup>

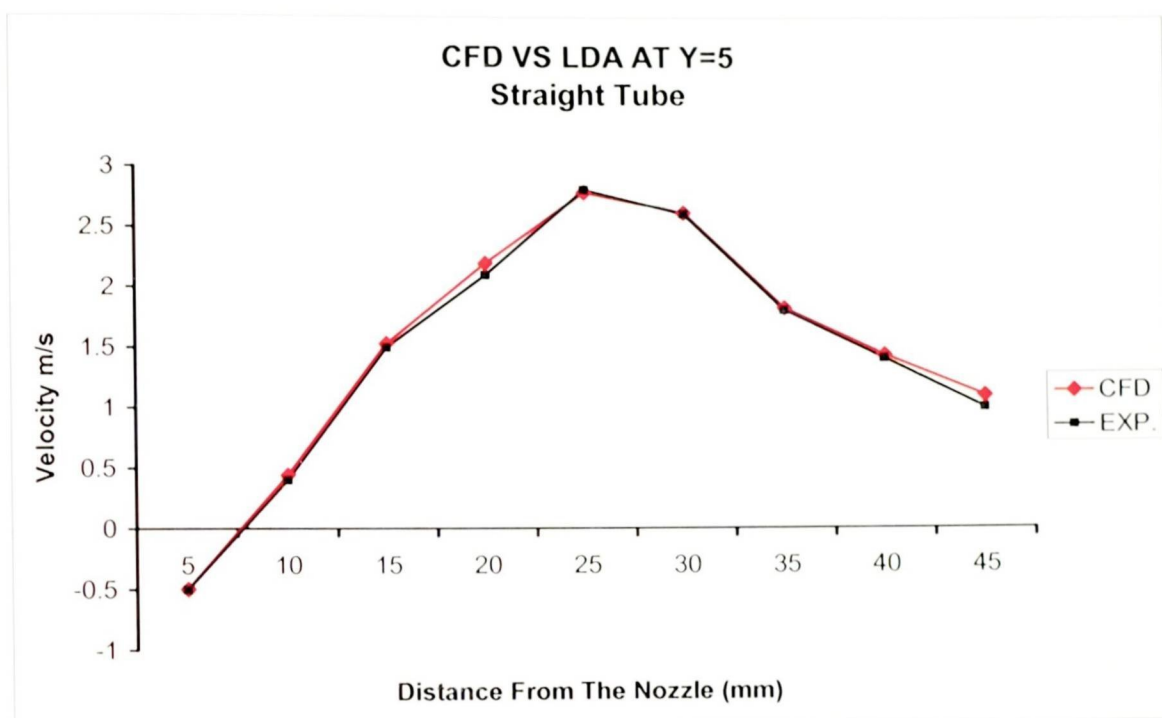


Figure 6.6.7: LDA VS CFD Measurements For The Aero Chamber Design

### §6.6.2 Conclusions

the conclusions reported in this section are only based upon the experimental observations.

- Time series data taken from the start of the injection was used to separate injection from inter-injection measurements.
- The lack of particles in the upper portion of the nozzle exit region suggested that the jet exited at a downwards angle. The main jet region was established through the  $y=0$  and  $y=-5$  planes. The plane  $y=-10$  exhibited a higher velocities than the  $y=+5$  plane. The downward motion of the jet created a re-circulatory pattern as the flow was deflected back from the lower, far corner, upwards and back towards the nozzle exit. The nozzle exit was horizontal and

parallel to the axis of the spacer device.

- The turbulence intensity values were reduced in the bulk flow regions. These were less influenced by the returning flow. The values were the lowest in the main jet region at  $y=-5$  mm.
- The majority of the data was cyclic, this meant the trigger input had functioned correctly. Inter-injection measurements have shown to significantly skew the velocity distributions towards a lower mean value.

### §6.7 Flow Visualization Studies

The method for this technique has been described in chapter 5. The high camera recorded 4500 frames per second, for this reason it will not be feasible to show all the frames in this thesis. It has been attempted to present the same time steps as the CFD study.

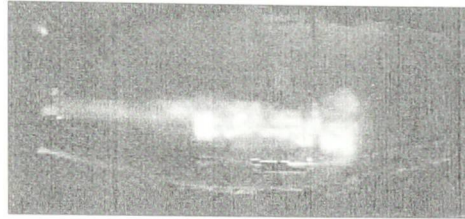
At 0.05 second, it can be seen from Figure (6.7.1a) that, the jet of drug has entered the spacer. The jet enters the device keeping a narrow profile, and then it has began to diffuse. This is exactly the flow pattern observed using CFD.

At time step 0.4 second, it can be seen from Figure (6.7.1.b), that the jet has detached completely and the drug has accumulated in the mouth piece half of the spacer. At this stage half the spacer was free of any drug. This was similar to the CFD findings.

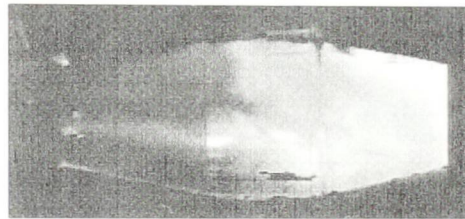
The next time step analysed was at 0.75 seconds. At this time step it is evident from Figure (6.7.1.c) that, there was a recirculation region near the mouth piece, which had caused the drug to extend back along the top wall towards the inlet. It is evident that there is also a small volume not containing any drug.

At 1.0 second, it is clear from Figure (6.7.1d), that, the majority of the spacer has

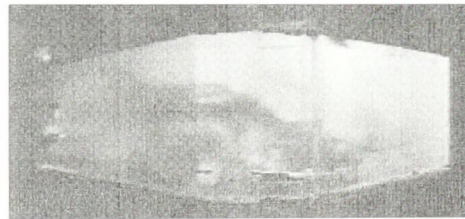
been filled with drug. However as reported from the CFD study, there is a small volume of the spacer not occupied with any drug.



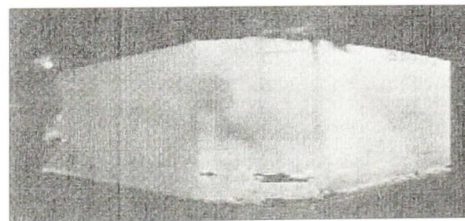
**Figure(6.7.1a) Time step 0.05 Sec.**



**Figure(6.7.1.b) Time Step 0.4 Sec.**



**Figure(6.7.1.c) Time Step 0.75 Sec.**



**Figure(6.7.1.d) Time Step 1.0 Sec.**

Figure 6.7.1: Flow Visualization High Speed Photos

## Discussions and Conclusions

*In this chapter the findings of experimental and CFD studies have been discussed. The objectives of this research set out in Chapter 1 have been addressed. Finally suggestions have been made with regards to progressing this research further.*

### §7.1 Introduction

The initial section of this chapter has provided answers to the questions raised in Chapter 1 of the thesis. In the remaining sections the CFD and experimental results have been discussed in detail.

### §7.2 Answers to the Questions Raised in Chapter 1

#### Question 1

**[Why do we need to study the flow behaviour within the Volumatic<sup>TM</sup>?]**

**Answer:** The reason for carrying out this research was to obtain a detailed flow study in the Volumatic<sup>TM</sup> spacer. This kind of research had never been initiated before and industry did possess any detailed study of this type. The findings from this research have highlighted the efficiency of the spacer and parameters controlling or contributing to the efficiency of the device. This is all novel research for industry.

---

### Question 2

**[What is the importance of this research?]**

**Answer:** The research was important because, it provided a detailed documented study of the current Volumatic<sup>TM</sup> spacer design and its modified versions. The study provided accurate efficiency values for each version, the CFD study was validated using LDA and High speed photography. The conclusion reached from this study was that, the current Volumatic<sup>TM</sup> spacer design could only be improved up to a certain limit. The limit was reached when all the parameters were optimised. The study has also shown the most efficient devices are in the form of Aero Chambers.

### Question 3

**[Is the research worthwhile?]**

**Answer:** The research has certainly been worthwhile, because, it has shown a new scientific approach for designing respiratory devices. Furthermore the research has justified its funding by providing a new spacer design which has an efficiency of 71% compared to the current 10%.

### Question 4

**[Would the current engineering tools such as Computational Fluid Dynamics (CFD) and experimental techniques such as Laser Doppler Anemometry (LDA) and high speed photography be adequate to carry out this research? ]**

**Answer:** The current engineering tools have been shown to be an essential part of this new approach to designing respiratory devices. It has to be pointed out that the, use of CFD simulations would remove the need for the manufacture of prototypes initially. Once the models are working in a satisfactory manner the prototype can then be built and LDA measurements taken. The use of LDA has provided a vast number of data samples, hence removing any ambiguity about the results. Finally the High speed photography has provided visual conformation with respect to our CFD study. It can therefore be concluded that the engineering tools and techniques were more than adequate in terms of providing relevant data in this study.

### §7.3 CFD Results

The initial part of this study was designed to use the CFD modelling approach to obtain an understanding of the flow pattern within the Volumatic<sup>TM</sup> Spacer. This work had never been carried out before, so the ability of the commercial CFD codes for modelling and design applications dealing with such complicated flow pattern as in the case of the Volumatic<sup>TM</sup> spacer was an unknown entity.

In any initial CFD study the most important starting point is to define a mesh fine enough to capture all the flow characteristics, without incurring any unnecessary computational time. For this study four different mesh configurations were used. The 200x100 mesh arrangement was the only configuration which captured the 40 m/s velocity at inlet, and the five re-circulation regions.

In the initial studies air was used to represent the drug, the 80x80 mesh was found to be adequate, as it captured the four re-circulation regions and the maximum velocity of 39.8 m/s at inlet. The next logical step in this research programme was to conduct a series of parametric studies. The initial study involved injecting air carrying a drug concentration into the spacer. The purpose of the concentration was to simulate the dispersion of the drug within the device, hence developing our understanding of the flow behaviour within the spacer. It was found that the maximum concentration near the mouth piece was only about 6.9%. This was of the same order as the figures reported in the literature. The obvious conclusion from this simulation indicated that, if the efficiency of the Volumatic<sup>TM</sup> was to be improved drastically a series of parametric studies needed to be carried out. The studies would cover a wide range of parameters such as:

- Geometry i.e. shape and length of the device
- Jet profile at inlet
- Jet Inclination angle
- Inlet velocity

The CFD model was validated experimentally using LDA data. Although air was used for the initial study, the LDA results showed a similar trend as those obtained by CFD. This was an encouraging sign and gave confidence to investigate further, other features. A series of studies were carried out concentrating on the effects, of jet configurations at inlet in terms of improving the efficiency of the spacer. The study took into consideration, three types of jet configurations at inlet, these were:

- Straight jet
- Cone jet
- Spray jet

The straight jet configuration is the current set up being used by industry in producing the MDI's.

The second case to consider was the cone jet configuration. The jet of drug and propellant leaves the nozzle in the shape of a cone, for which various cone angles were studied. The findings showed that, the jet with a cone angle of  $5^{\circ}$  delivered the highest concentration of 9.4% of the drug at the mouth piece. This was not a great improvement on the present system and certainly did not warrant the expense of manufacturing the pressurised canister and the exit nozzle to deliver the drug in this particular format. However as there was no data available in relation to the design of the Volumatic<sup>TM</sup> it was necessary to carry out this study, to obtain a better understanding of the flow field under different inlet conditions and gain confidence in the model in the model set up.

The next jet profile input was in the shape of a spray jet for which once again a range of angles were studied. It was predicted by the model that the jet with a spray angle of  $19.5^{\circ}$  would deliver 9.3% of the drug to the mouth piece, hence making it the most efficient spray type jet tested.

The conclusions from the jet profile studies indicated that although efficiency in terms

of drug delivery could be improved, by changing the jet profile, the improvements achieved were not sufficient to persuade the manufacturers to redesign the MDIs.

The length of the Volumatic<sup>TM</sup> spacer has for some time been a feature, which has influenced patients not to use the device. This made it an important feature to be studied in detail. In the initial part of the study the length of the Volumatic<sup>TM</sup> spacer was reduced from 0.24 m to 0.12 m. This simple geometrical change improved the drug delivery efficiency from 6.5% to 23%, three and half times more efficient over the original design. At this particular length a range of exit velocities were studied, and it was concluded that the exit velocity of 40 m/s gave the highest concentration of the drug at the mouth piece. The velocity range studied were 10, 30 and 40 m/s. The other outstanding feature of this design was that, it showed the whole of the device was occupied with the drug and an improved mixing process took place due to increased flow re-circulation within the spacer.

The length of the spacer was reduced further from 0.12 m to 0.06 m and once again the same range of inlet velocities were studied. It was concluded for this particular model that, if the inlet velocity into the spacer could be reduced to 30 m/s the maximum value of the drug delivered to the mouth piece would be 30%.

The studies carried out thus far, have indicated, that improving the efficiency of the Volumatic<sup>TM</sup> spacer was dependent mainly on the inlet velocity from the nozzle and the length and shape of the Volumatic<sup>TM</sup> spacer itself. This project was only concerned with the design study of the spacer, with a view to improve its delivery efficiency, furthermore there were other centres already involved with research around the PMDI and its nozzle.

The research having provided a valuable insight into the lack of efficiency of the spacer, effort was directed towards a standard cylindrical shape, that had come to light after companies had produced spacers in this format. It was once again found that there was no experimental data, or any documentation as to why there had been a shift in opinion towards the manufacture of cylindrical spacers. The company

concerned in the manufacture of the cylindrical spacer would not release any data regarding this device. The only step forward was to obtain one of the cylindrical spacer models through our sponsors (Astra Zeneca Pharmaceutical) and carry out a series of parametric studies and LDA experiments. The conclusions from the parametric studies showed that the cylindrical spacer design could also be improved. A revised model version was made by making some fundamental design changes in terms of diameter, length of the device and bleed holes. The CFD model of the device showed that it delivered approximately 71% of the drug to the mouth piece, making it the most efficient device reported in the literature to date. This novel work contributed to the paper <sup>(30)</sup>

### §7.4 Experimental Results

The Volumatic<sup>TM</sup> spacer has been extensively validated at four locations each extending 0.05 m into the spacer. The experimental results are very close to those obtained using CFD. This is particularly good, since the CFD simulations were carried out some six months prior to the LDA measurements. The Tube design spacer has also been validated, by measuring velocity values along the two locations out of the four which were used for the Volumatic<sup>TM</sup> spacer.

### §7.5 Flow Visualizations

The flow visualization studies were carried out using a Kodak camera, capable of capturing 4500 frames per second. The visualization results, have highlighted the CFD predictions that, in the original spacer, there was a volume of the device which did not contain any or very small quantity of the drug, hence serving no real purpose.

### §7.6 Conclusions

The findings from this research have revealed that the Volumatic<sup>TM</sup> spacer as it stands is not a very efficient device for delivering drugs to the patients suffering from asthma. The new Tube spacer design can increase the efficiency to 71% compared to the approximately 10% obtained with the Volumatic<sup>TM</sup> spacer. The size of the Tube design spacer would also make it more appealing to the patients. Thus a wider use is anticipated. The final remark regarding this type of research is that, in order to have meaningful results it is important to have a multi disciplinary set up so that benefits from LDA and High speed photography results can be fed back into the numerical studies.

### §7.7 Further Work

The work carried out thus far has comprised of a detailed parametric study carried out on the Volumatic<sup>TM</sup> spacer and has shown the deficiencies of the design. The work has also concluded that the cylindrical spacer design is more efficient, especially the modified version.

#### §7.7.1 Geometrical Studies

The research carried out has shown, how important the geometry of a device can be in terms of flow field. This factor alone had a considerable influence on the percentage of the drug delivered. It is important that the next step in continuing this research would consist of a detailed geometrical studies, where various geometries are chosen and a comprehensive set of parametric studies are carried out.

### §7.7.2 Full Flow Path

In order to complete the research in detail, studies need to be carried out, to model the breathing action of human. This would play a vital role in the way the drug is taken from the spacer and into the human airways. A shallow breath would only partially take empty the spacer, whereas a deep breath would take in the whole content of the spacer. It is also important for the patient to breath in at a certain time when there is a high concentration of the drug present. This time was found to be 0.4 seconds for the studies carried out during our research.

### §7.7.3 Different Drugs

There are a variety of different drugs available on the market, each drug having its own properties. It would be a useful study to model a different number of drugs and draw some kind of conclusion about the dispersion of the available drugs on the market.

### §7.7.4 Clinical Trials

It is important to test the final version of the device in a real situation. This would involve a major effort on the part of collaborating partners. The chosen design has to be manufactured and distributed to clinical trial centres. The patients have to be given the current spacer device and the new design. The patient needs to keep a log of the number of times he/she uses each device over a limited period. After this period the device is changed and the new device is used exactly the same number of times and over the same period. The clinicians need to collect all the data and analyse it statistically. an idea about the way they are dispersed within the spacer. is a possibility that different drugs would The addition of particle tracking to this model would high light the regions were the drug particles are likely to be deposited.

There are several features which can be looked at in more detail during the course of the next research. Initially it is important to find out if the tube design spacer is actually the optimum shape and design in every respect. The number of holes can be increased as they seem to have an effect on reducing the exit velocity of the fluid. It is also necessary to investigate other geometrical shapes. Finally it is important to study the spacer for a range of respiratory drugs, as characteristics of one drug may make it suitable for a particular shaped spacer.

---

# References

---

- [1] J. C Angus. Motion measurement by laser doppler techniques. *Ind. Eng. Chemistry*, 61:8-20, 1969.
- [2] P.R Appleton. A study of axisymmetric two phase flashing jets. SRD R303, UKAEA, 1984.
- [3] Bazhaikin A.N. Buzukov A.A. Timoshenko B.P. Bichenko E.I Rabinovich R.L. Baev, V.K. Experimental study of the development and structure of high velocity liquid jet in air. *Progress in Astronautics and aeronautics*, 105:104-112, 1986.
- [4] P. S. Bedi and M. T. Thew. A simplified optical arrangements for the laser doppler velocimeter. *J.Phys*, E 4:27-28, 1971.
- [5] R Brown and J.L York. Spray formed by flashing liquid jets. *A.I.Ch.E.J.*, 8(2):149-153, 1962.
- [6] P.G.J Burney. asthma mortality in england and wales evidence for a further increase. *Lancet*, 2:323-326, 1986.
- [7] M. Burr, B. Butland, S. King, and E. Vaughan-Williams. Changes in asthma prevalence; two surveys 15 years apart. *Arch. Dis. Childhood*, 64:1452-1456, 1989.
- [8] D Choudhury. Introduction to the renormalization group method and turbulence modeling. *Fluent Inc.*, pages 1-50, 1993.
- [9] A. Chuffart, F. H. Sennhauser, and J. H Wildhaber. Factors affecting the efficiency of aerosol therapy with pressurised metered-dose inhalers through plastic spacers. *Swiss Med. Weekly*, 131:14-18, 2001.
- [10] A.R Clark. Metered atomization for respiratory drug delivery. *PhD Thesis, Loughborough Univ. of Tech.*, 1991.
- [11] G. K Crompton. New inhaler devices. *Eur. Respir. J.*, 1:674-680, 1988.
- [12] W. Demuren, A.O.and Rodi. Calculation of turbulent-driven secondary motion in non-circular ducts. *J. Fluid Mech.*, 40:189-222, 1984.
- [13] R Dhand, s.k Malik, M Balakrishnan, and S.R Verma. High speed photographic analysis of aerosols produced by metered dose inhalers. *J. Pharm. Pharmacol.*, 40:429-430, 1988.

- [14] J.K Dokowicz. Quasi-steady droplet phase change in the presence of convection. *Los Alamos Report*, 1979.
- [15] J.K Dokowicz. A particle-fluid numerical model for liquid sprays. *Journal of Computational Physics*, 35:229–253, 1980.
- [16] M Dolovich, R Ruffin, D Corr, and M T Newhouse. optimal delivery of aerosols in the human respiratory tract. *chest*, 80(suppl):911–915, 1991.
- [17] Ranz W. E and Marshall W. R. Evaporation from drops part i. *Che. Eng. Prog.*, 48:141–146, 1952.
- [18] Ranz W. E and Marshall W. R. Evaporation from drops part ii. *Che. Eng. Prog.*, 48:173–180, 1952.
- [19] T. Ehtezazi, M. A Horsefield, P. W Barry, and C O’Callahan. Reconstruction of the upper airway during inhalation from drug delivery system using mri. *Proc. Drug Deliver to the Lungs*, pages 90–93, 2000.
- [20] G.M Faeth. Mixing, transport and combustion in sprays. *Prog. Energy Combust. Sci.*, 13:293–345, 1978.
- [21] G.M Faeth. Evaporation and combustion of sprays. *Prog. Energy Combust. Sci*, 9:1–76, 1983.
- [22] J.H. Ferziger and M Peric. Springer publishing company. *Comput. Methods Appl. Mech. Eng*, 64:20–35, 1999.
- [23] W. H Finlay and C. F Lange. Modelling the behaviour of inhaled pharmaceutical aerosols. *Proc. Drug Delivery to the Lungs*, pages 72–77, 2000.
- [24] G. E Fletcher. Factors affecting the atomization of saturated liquids. *PhD Thesies*, 1975.
- [25] W.G. Gorman and G.D. Hall. Inhalation aerosols. *In Swarbrick, J. (Ed.)*.
- [26] A.D Gosman and E Ioannides. Aspects of computer simulation of liquid-fueled combustor. *J. Energy*, 7:482–490, 1983.
- [27] C Hiller, M Mazumder, D Wilson, and R Bone. Aerodynamic size distribution of metered dose bronchodilator aerosols. *AM. Rev. Resp. Dis.*, 118:311–317, 1986.
- [28] S.T Holgate and J.P Finnetry. Recent advances in understanding the pathogenesis of asthma and its clinical implications. *Q. J. Med.*, 66:5–19, 1998.
- [29] S. Jain. Three-dimensional simulation of turbulent particle dispersion. *PhD Thesies, University of Utah*, 1995.
- [30] V. Jalili, M. K Patel, and C. Bailey. Numerical modelling of inhaler spacer: A novel study. *ASME FEDSM conference Sanfrancisco*, 1999.
- [31] V. Jalili, M. K Patel, and C. Bailey. Application of cfd in designing inhaler spacers. *ASME conference Orlando*, 2000.
- [32] V. Jalili, M. K Patel, and C. Bailey. Design analysis of volumatic spacer. *American Aerosol Association*, 2000.
- [33] V. Jalili, M. K Patel, and C. Bailey. Design analysis of volumatic spacer. *ASME*, 2002.

- [34] V. Jalili, M. K Patel, and C. Bailey. Would smaller devices be as efficient? *BMJ Submitted*, 2003.
- [35] Thiruvengadam A. Johnson, V.E. Rock tunnelling with high speed water utilizing cavitation damage. *ASME*.
- [36] S.-E. Kim, D. Choudhury, and Patel B. computations of complex turbulent flows using the commercial code fluent. *Proceedings of the ICASE/LaRC/AFOSR symposium on modeling complex turbulent Flows Hampton Virginia*, 1997.
- [37] K. K. Y Kuo. Principles of combustion. *John Wiley and Son*, 1986.
- [38] B.E. Launder and Spalding D.B. The numerical computations of turbulent flows. *Computer methods In applied mechanics and engineering*, 3:269–289, 1974.
- [39] B.E. Launder and D.B. Spalding. The numerical computation of turbulent flows. *Comput. Methods Appl. Mech. Eng.*, 3:269–289, 1974.
- [40] K.C Lee, K.O Suen, and M. Yianneskis. Characterisation of evaporating sprays from metered-dose inhalers by lda. *Proc. 4<sup>th</sup> Int.Conf.on Laser Anemometry*, 1991.
- [41] A. Leonard. A stable and accurate convection modelling procedure based on quadratic upstream interpolation. *Appl. Mech. Engrg*, 19:59–98, 1979.
- [42] A.B. Liu and Reitz R.D. Modelling the effects of drop drag and breakup on fuel sprays. *SAE 930072*, 1990.
- [43] R Melchor, Biddiscombe M.F, Mak V.H.F, Short M.D, and Spiro S.G. Lung deposition patterns of directly labelled salbutamol in normal subjects and in patients with reversible airflow obstruction. *Thorax*, 48:506–511, 1993.
- [44] D. Moren, F.and Hatheway. Characterisation of particle size from pressurised aerosol intended for oral inhalation. *ICLASS-85, London*, pages 11B.1–6, 1985.
- [45] F. Moren. Drug deposition of pressurized inhalation aerosols. *Int. J. Pharm.*, pages 205–212, 1978.
- [46] F. Moren. Studies on pressurised aerosols for oral inhalation. *PhD Thesis Uppsala University, Sweden*, 1980.
- [47] S. A Morsi and A. J Alexander. An investigation of particle trajectories in two-phase flow. *J. Fluid Mech.*, 55:193–208, 1972.
- [48] J.D. Naber and R.D Reitz. Modelling engine spray wall impingement. *SAE 880107*, 1998.
- [49] Cramer J.B. Nebeker, E.B. Visualisation of the central core of high speed water jets. *conference Rolla, Missouri*.
- [50] S.P Newman, F Moren, E. Troast, N. Talace, and S.W Clarke. *Int. J. Pharmaceut.*, 74:209–213, 1991.
- [51] S.P Newman, D. Pavia, and N. Garland. Effect of various inhalation modes on the deposition of pressurised aerosols. *Eur. J. Dis.*, 63 (Suppl.119):57–65 1982.

- [52] P.J O'Rourke. Modelling of drop interaction in thick sprays and comparisons with experiment. *I.MechE, Stratified charge automotive engines*, 1980.
- [53] G.P Polli, W.M Grim, F.A Bacher, and M.H Yunker. Influence of formulation on aerosol particle size. *J. Pharm. Sci.*, 58 part 4:484–486, 1969.
- [54] Montreal Protocol. Report of the technology and economic assessment panel including recommendations for essential use production/consumption exemptions for ozone depleting substances. 1984.
- [55] American Asthma Association Research. Devices and their application. *Arch. Dis. Childhood*, 64:1452–1456, 1989.
- [56] W. C. Reynolds. Fundamentals of turbulence for turbulence modelling and simulation. *Lecture notes for Von Karman Institute*, report number 755, 1987.
- [57] J. E. Rizzo. Velocity measuring interferometers. electro-optic system in flow measurements. *University of Southampton 25th-26 September*, 1972.
- [58] W. Rodi. Models and their applications in hydraulics a state of the art review. *Delft, The Netherlands.*, page all, 1980.
- [59] H. Rouse. cavitation in the mixing zone of a submerged jet. *La Houille Blanche*, pages 9–19, 1953.
- [60] M. J. Rudd. A new theoretical model for laser doppler meter. *J.Phys*, E 2:52–58, 1969.
- [61] E. Sher and C. Elata. Spray formation from pressure cans by flashing. *Ind. Eng. Chem., Process Des. Dev.*, 16(2):237–242, 1977.
- [62] Liou W.W Shabbir Shih, T.H and Zhu J. A new  $k-\epsilon$  eddy viscosity model for high reynolds number turbulent flows- model development and validation. *Computers Fluids*, 24.
- [63] I. Shrubbs. Influence of throat coating and flow rate on usp throat deposition. *Proc. Respiratory Drug Delivery*, pages 413–416, 1998.
- [64] Glaxo smith kline. Product literature. 1, 1989.
- [65] K. W. Stapleton, E. Guentsch, M. K Hoskinson, and W. H Finlay. On the stability of  $k-\epsilon$  turbulence modelling for aerosol deposition in the mouth and throat: a comparison with experiment. *J. Aerosol Sci.*, 31:739–749, 2000.
- [66] J. H. Toogood, J. Baskerville, B. Jennings, and S.A. Johanson. Factors affecting the efficiency of aerosol therapy with pressurised metered-dose inhaler through plastic spacers. *Journal of Respiratory Diseases*, 122:100–107, 1982.
- [67] Patankar S. V. *Numerical Heat Transfer and fluid flow*, volume 1. McGraw-Hill New York, 1980.
- [68] H. K Versteeg and W Malalasekera. *An introduction to computational fluid dynamics The finite volume method*, volume 1. Longman scientific Technical 1995.
- [69] Hargrave G Harrington L Shrubbs I Hodson D. Versteeg, H.K. The use of computational fluid dynamics (cfd) to predict

- pmdi air flows and aerosol plume formation. *Respiratory Drug Delivery*, pages 257–264, 2000.
- [70] Y Wan and N Peters. Numerical simulation of diesel spray. *Atom. Spray*, 9:111–132, 1999.
- [71] M.V Wiener. How to formulate aerosols to obtain the desired spray pattern. *J. Soc. Cos. Chem.*, pages 289–297, 1958.
- [72] Y. Yeh and H.Z Cummings. Localized fluid flow measurements with he-ne laser spectrometer. *Appl Phys.*, (lett.4):176–178, 1964.
- [73] J.L York. Thermodynamics of spray formation. *J.Soc. Cos. Chem.*, 7:204–214, 1957.
- [74] O. C. Zienkiewicz and R. L Taylor. *The Finite Element Method Solid and Fluid Mechanics*, volume 2. McGraw-Hill, New York, 1991.